



**HAL**  
open science

## Trace element composition and U-Pb ages of cassiterite from the Bolivian tin belt

Laura Gemmrich, Lisard Torr , Joan Carles Melgarejo, Oscar Laurent, Jean  
Vallance, Cyril Chelle-Michou, Thierry Sempere

► **To cite this version:**

Laura Gemmrich, Lisard Torr , Joan Carles Melgarejo, Oscar Laurent, Jean Vallance, et al.. Trace element composition and U-Pb ages of cassiterite from the Bolivian tin belt. *Mineralium Deposita*, 2021, 56 (8), pp.1491-1520. 10.1007/s00126-020-01030-3 . hal-03436560

**HAL Id: hal-03436560**

**<https://hal.science/hal-03436560>**

Submitted on 23 Nov 2021

**HAL** is a multi-disciplinary open access archive for the deposit and dissemination of scientific research documents, whether they are published or not. The documents may come from teaching and research institutions in France or abroad, or from public or private research centers.

L'archive ouverte pluridisciplinaire **HAL**, est destin e au d p t et   la diffusion de documents scientifiques de niveau recherche, publi s ou non,  manant des  tablissements d'enseignement et de recherche fran ais ou  trangers, des laboratoires publics ou priv s.

1 **Trace element composition and U-Pb ages of cassiterite from the Bolivian tin belt**

2 Laura Gemrrich<sup>a</sup>, Lisard Torró<sup>b,\*</sup>, Joan Carles Melgarejo<sup>a</sup>, Oscar Laurent<sup>c</sup>, Jean Vallance<sup>b</sup>, Cyril Chelle-Michou<sup>c</sup>,  
3 Thierry P.A. Sempere<sup>d</sup>

4 <sup>a</sup>*Departament de Mineralogia, Petrologia i Geologia Aplicada, Universitat de Barcelona (UB), C/Marti i*  
5 *Franquès s/n, 08028 Barcelona, Spain*

6 <sup>b</sup>*Geological Engineering Program, Faculty of Sciences and Engineering, Pontifical Catholic University of Peru*  
7 *(PUCP), Av. Universitaria 180, San Miguel, Lima 15088, Peru*

8 <sup>c</sup>*ETH Zürich, Department of Earth Sciences, Institute for Geochemistry and Petrology, 8092 Zürich, Switzerland*

9 <sup>d</sup>*Consultant and Exploration Manager at ANDES C&P, Lima, Peru*

10

11 To be submitted to *Mineralium Deposita*

12

13 \*Corresponding author: Dr. Lisard Torró

14 E-mail address: [lisardtorro@hotmail.com](mailto:lisardtorro@hotmail.com)

15 Phone: (+51) 6262000 Ext. 5060

16 **Abstract**

17 The Bolivian tin belt is a metallogenic province in the Eastern Cordillera of the Andes known for its Sn, W, Ag  
18 and base metal deposits. Cassiterite, which is a major constituent in many magmatic-hydrothermal ore deposits  
19 from the Bolivian tin belt, can incorporate dozens of elements within its crystal lattice, making it a useful  
20 geological tracer mineral, and also a potential host of critical elements. New U-Pb dating of cassiterite yields Late  
21 Triassic (Kellhuani deposit) and Late Oligocene to earliest Miocene (Viloco, Huanuni and Llallagua deposits)  
22 ages. These ages confirm that Sn mineralization in the Bolivian tin belt occurred at least in two separate events  
23 during two major magmatic episodes apparently triggered by mantle upwelling, decompression melting and basalt

24 production promoting high heat flow into the overlying crust. The composition of studied hydrothermal cassiterite  
25 yields some geochemical trends that are attributed to its distance to the causative intrusion and/or level of  
26 emplacement. For example, cassiterite is generally enriched in Nb and Ta and yields higher Ti/Zr and Ti/Sc ratios  
27 in samples from xenothermal ore deposits located adjacent to intrusive complexes relative to shallow xenothermal  
28 and epithermal ore deposits. Therefore, these geochemical trends in cassiterite are useful tracers pointing to  
29 magmatic-hydrothermal centers. REE distribution in cassiterite was likely influenced by boiling processes, which  
30 resulted in tetrad-type irregularities. Cassiterite from the Bolivian tin belt is unattractive as a source for Nb  
31 (interquartile range [IQR] 4.84-0.037 ppm), Ta (IQR 0.0924-0.0126 ppm) and Ge (IQR 3.92-0.776 ppm). Some  
32 deposits, however, contain cassiterite relatively enriched in In (IQR 96.9-9.78 ppm, up to 1414 ppm) and Ga (IQR  
33 92.1-3.03, up to 7437 ppm), that could constitute an attractive supplementary source for these elements in addition  
34 to sulfide minerals in the same deposits.

35 **Keywords:** Central Andes, geochemical composition, high-tech metals, critical elements, U-Pb geochronology

## 36 **Introduction**

37 Cassiterite, a tin oxide mineral ( $\text{SnO}_2$ ) of the rutile group and the primary Sn ore mineral, can incorporate a wealth  
38 of elements in minor and trace concentrations within its structure. Typical elements that are present in significant,  
39 although variable, amounts within its crystal lattice include Fe, Ti, Mn, Al, Nb, Ta and U, which substitute for Sn  
40 cations. Innovation in analytical chemistry (i.e., ICP-MS and micro-PIXE; e.g., [Plimer et al. 1991](#); [Serranti et al.](#)  
41 [2002](#)) further allows the determination of other elements found in trace amounts in cassiterite such as those of the  
42 rare earth elements (REE), Be and In amongst others. Some of these elements (e.g., Nb, Ta, W, REE, Be and In)  
43 are considered high-tech metals critical to the global economy ([Skirrow et al. 2013](#); [European Commission 2017](#);  
44 [Schulz et al. 2017](#)).

45 The broad range of P-T-X conditions in which cassiterite forms, its strong physical and chemical resistance and its  
46 plethora of chemical constituents including both compatible and incompatible elements makes this mineral useful  
47 as a petrogenetic indicator ([Murciego et al. 1977](#); [Plimer et al. 1991](#); [Serranti et al. 2002](#); [Jiang et al. 2004](#); [Chen et al.](#)  
48 [2019](#)). Furthermore, the moderate  $\text{U}^{4+}$  and low  $\text{Pb}^{2+}$  contents and high Pb isotope closure temperature (up to  
49  $860^\circ\text{C}$ ; [Zhang et al. 2011](#)) in cassiterite makes it suitable for U-Pb dating (e.g., [Zhang et al. 2017, 2019](#); [Guo et al.](#)  
50 [2018](#); [Neymark et al. 2018](#); [Chen et al. 2019](#); [Cheng et al. 2019](#); [Kendall-Langley et al. 2019](#); [Moscati and](#)  
51 [Neymark 2019](#); [Zhao et al. 2019](#); [Legros et al. 2020](#); [Lehmann et al. 2020](#); [Mao et al. 2020](#)).

52 The Bolivian tin belt, in the Central Andes, is one of the largest tin metallogenic belts worldwide and in 2019  
53 accounted for about 6% of the global tin production; in addition, it produced about 5% of silver and 1.5% of  
54 tungsten globally (U.S. Geological Survey 2020). Despite massive tin production since early 1900s, by when most  
55 Bolivian great tin deposits had been discovered, Bolivia is estimated to contain > 8% of the world's tin reserves  
56 (Arce-Burgoa and Goldfarb 2009; U.S. Geological Survey 2020). However, a detailed survey on the geochemical  
57 composition of cassiterite from this metalliferous belt has never been conducted. Furthermore, the age of the  
58 magmatism along the Bolivian tin belt is relatively well constrained through U-Pb zircon dating, but dispersion of  
59 K-Ar and Ar-Ar mica and feldspar dates reveals a complex thermal history (Ahfeld 1967; Clark and Farrar 1973;  
60 Evernden et al. 1977; Grant et al. 1979; McBride et al. 1983; Clark et al. 1990; Sugaki et al. 2003; Gillis et al.  
61 2006; Cordani et al. 2019). This is especially the case in the northern segment of the Bolivian tin belt, where  
62 plutons of Triassic age cluster. As previous geochronological studies on tin deposits were mainly based on K-Ar  
63 and Ar-Ar dating of hydrothermal mica, some questions remain in respect of their reliability. In this study we  
64 determine the geochemical composition and U-Pb dates of cassiterite grains from nine deposits/districts of the  
65 Bolivian tin belt with a threefold aim: i) to refine the geochronology of tin mineralization in this region, ii) to  
66 constrain the mechanisms that control minor and trace element concentrations in cassiterite crystallized at  
67 contrasting conditions within the xenothermal (i.e., polymetallic high-temperature [~300-500°C] vein-type  
68 deposits emplaced in the sub-epithermal environment; Buddington 1935, Imai et al. 1975, Heuschmidt et al. 2002)  
69 and epithermal environments, and iii) to assess their potential as source of high-tech byproducts.

## 70 **Geological setting**

### 71 **Geological setting of the Bolivian Andes**

72 The ore deposits dated in this paper are located in the northern and central segments of the Bolivian Eastern  
73 Cordillera. These segments are parts of the northwest limb of the Bolivian Orocline (Isacks 1988), and, more  
74 precisely, of its southernmost portion, i.e. close to the oroclinal “core hinge”. This broad region therefore shares  
75 many geological characteristics with adjacent Peru, and the descriptions and comments in this section are often  
76 envisioned from this point of view.

77 The Bolivian Andes present a marked morphotectonic partition that reflects differences in geological history,  
78 paleostructural domains and current crustal structure. These domains are, from west to east, the Western  
79 Cordillera, the Altiplano and the Eastern Cordillera. Furthermore, a deformed “Subandean Belt” serves as a

80 tectonic transition between the Eastern Cordillera and the nearly undeformed Amazonian Lowlands to the  
81 northeast and east.

82 The Western Cordillera corresponds to the present-day location of the main magmatic arc related to subduction  
83 processes. It is characterized by a ~100 km-wide belt of volcanoes sitting on a high-altitude surface, which reflects  
84 a considerable crustal thickness beneath (e.g., [James 1971a,b](#); [Isacks 1988](#); [Kono et al. 1989](#); [Lamb and Hoke](#)  
85 [1997](#)). At the latitudes of Bolivia, the Western Cordillera however extends also in adjacent Northern Chile. It is  
86 mostly composed of Late Miocene to recent intermediate to felsic igneous rocks that intruded in and extruded over  
87 Jurassic and Cretaceous sedimentary and volcanic rocks. The igneous rocks from the Western Cordillera belong to  
88 the magnetite series and record a high contribution of a mantle component ([Ishihara 1981](#); [Sugaki et al. 1988a](#)).

89 The upper crustal structure of the Altiplano varies significantly. It seems likely that its lower crust has been  
90 thickened through ductile flow from the overthickened crust along both the Western and Eastern cordilleras  
91 ([Husson and Sempere 2003](#)). Much of the current Altiplano surface is covered by recent sedimentary and volcanic  
92 deposits; it is strongly suspected that its eastern fringe corresponds to the buried western fringe of the Eastern  
93 Cordillera, and thus constitutes a transitional strip between the two domains. In particular, this transition is  
94 confirmed by the observation that many magmatic phenomena that affected the Altiplano also affected the crust of  
95 the western Eastern Cordillera, along which products of coeval and related magmatism are commonly observed  
96 (see below).

97 The scope of this paper is focused on the Eastern Cordillera since it hosts the Bolivian tin belt. The Eastern  
98 Cordillera was formed by inversion and substantial shortening of a Triassic rift system ([Sempere 2000](#); [Sempere et](#)  
99 [al. 2002](#)). This protracted compressional to transpressional deformation has developed since the Eocene and/or  
100 Oligocene in relation to the formation of the Bolivian Orocline (e.g., [Farrar et al. 1988](#); [Sempere et al. 1990](#);  
101 [Roperch et al. 2006](#)), and the ensuing erosion has resulted in the exposure of mainly Ordovician and Silurian  
102 strata, which as a whole may be over ~10 km thick.

103 The almost exclusively marine stratigraphic set formed by the Ordovician to Devonian strata is so thick that it  
104 raises the question of the geotectonic context in which this succession accumulated, and, indirectly, that of the  
105 time at which subduction was initiated at the latitude of Bolivia and Peru. Both present-day territories were part of  
106 supercontinents Rodinia and Pannotia; Laurentia separated from the latter at the latitudes of Peru and Bolivia  
107 through the opening of the Iapetus Ocean during the latest Neoproterozoic ([Scotese 2009](#)), which implies that what

108 was to become the Central Andean margin is very likely to have been passive at least in the earliest Paleozoic. A  
109 subduction-arc geochemical signature is however unambiguously noted in Carboniferous plutons of Peru  
110 (Mišković et al. 2009), which provides a minimum age for the onset of subduction at these latitudes.

111 The overall geological evolution of Bolivia has been summarized by Sempere (1995), who divided the  
112 stratigraphic record into a number of supersequences that reflect major changes in tectonic context. This  
113 preliminary understanding has been refined since that time, in particular thanks to new data from Bolivia and  
114 especially Peru. The Carboniferous arc orogeny that developed along at least the Eastern Cordillera of Peru was  
115 followed in the Permian by the extensional collapse of the resulting overthickened crust (Mišković et al. 2009).

116 Extensional conditions considerably increased in the Middle to Late Triassic, and resulted in the development of a  
117 major back-arc rift system (Sempere et al. 2002; Spikings et al. 2016). During the “Mitu time interval” (~240–220  
118 Ma), such an intense extension and associated mantle-derived mafic magmatism are likely to have generated an  
119 anomalously high heat flow. Late Triassic crustal anatexis is documented in several areas of contiguous E and SE  
120 Peru (see Kontak et al. 1990); in the NW-trending segment of the Eastern Cordillera of Bolivia, anatexis is  
121 recorded by the Zongo-Yani batholith (Fig. 1A), which consists of two-mica granite plutons that are commonly  
122 foliated; the peraluminous composition points to an anatectic origin, and the foliation indicates extensional  
123 shearing conditions during magma emplacement. In the Cuticucho-Samaini area, which is located ~25 km north of  
124 the Milluni Sn-Zn deposit (Fig. 1A), the Zongo-Yani batholith locally displays facies that range from pervasively  
125 foliated to weakly foliated, whereas its composition varies from monzogranite to syenogranite (Farrar et al. 1990).  
126 U-Pb zircon dating yielded dates of 222.2 –9.1/+7.7 and 225.1 –4.4/+4.1 Ma on the pervasively and weakly  
127 foliated facies, respectively (the weighted mean of these dates is 224.5 –4.0/+3.6 Ma). The U-Pb work confirmed  
128 that zircons from this pluton had been recycled by anatexis, and these dates are based on lower intercepts in the  
129 respective concordia diagrams (Farrar et al. 1990); all zircons that Gillis et al. (2006) attempted to date by the U-  
130 Pb method were also found to be discordant and gave  $^{206}\text{Pb}/^{238}\text{U}$  dates between 263 and 226 Ma for the Zongo  
131 pluton.

132 The Triassic rifting led to the subsequent accumulation of a stratigraphic succession that ranges well into the  
133 Jurassic (Sempere et al. 2002). After an apparently long sedimentation hiatus, deposition resumed at ~100 Ma; a  
134 significant increase in subsidence took place at ~90 Ma, reflecting the coeval growth of the main magmatic arc  
135 (Sempere 1994; Demouy et al. 2012). The latest Cretaceous to Eocene stratigraphic record mainly consists of red

136 beds forming a monotonous succession that may be several km thick (Sempere et al. 1997; Horton 2001),  
137 interpreted as a classical foreland basin (e.g., DeCelles and Horton 2003).

138 Arc migration is best recorded in southern Peru. Mamani et al. (2010) and Demouy et al. (2012) showed that in  
139 this large region the arc, from a position currently offshore, migrated northwards between ~130 and ~45 Ma to  
140 occupy a position that coincides with the Andahuaylas-Yauri batholith south of Cuzco; the arc has migrated  
141 “back” southwards since ~31–30 Ma (Mamani et al. 2010). Because the position of the arc is largely controlled by  
142 the dip angle of the subducted slab, the latter back-migration must have implied a widening of the asthenospheric  
143 wedge, which in turn involved mantle upwelling and thus decompression melting, and therefore the production of  
144 large amounts of basaltic magma (Mamani et al. 2010). This logical chain is confirmed by the widespread  
145 existence of basaltic magmatism of alkaline to shoshonitic composition centered over most of the Altiplano of  
146 southern Peru and Bolivia, between ~31 and ~22 Ma in southern Peru (Kontak et al. 1996; Sandeman et al. 1995),  
147 and between ~28 and ~21 Ma across the Bolivian Altiplano (Soler and Jiménez 1993); Fornari et al. (2002)  
148 detected a diachronic onset of mafic volcanism from ~29 Ma in the southern Peruvian Altiplano to ~21–20 Ma in  
149 the southernmost Bolivian Altiplano. The cumulated thickness of basaltic flows may locally be >2 km (Baldellón  
150 et al. 1994), which eloquently illustrates the magnitude of the related mantle upwelling and thus anomalous heat  
151 flow. The available dataset concerning this segment of the Bolivian Orocline suggests that mafic magmatism  
152 extended beneath the entire Altiplano of southern Peru and Bolivia as well as adjacent areas, and that it has  
153 continued through the Neogene and Quaternary, at least episodically at the surface.

154 In the Bolivian Altiplano, these mafic lavas occur as flows, sills, dikes and small intrusive stocks; thick and  
155 extended flow breccias are common and suggest that many volcanic centers were active at that time (Fornari et al.  
156 2002). Near the triple junction of Bolivia, Peru and Chile, the mafic Abaroa Formation yielded whole-rock  $^{40}\text{Ar}$ -  
157  $^{39}\text{Ar}$  dates comprised between  $28.0 \pm 0.1$  and  $27.3 \pm 0.1$  Ma (Fornari et al. 2002).

158 In the central Bolivian Altiplano, basaltic sills yielded whole-rock  $^{40}\text{Ar}$ - $^{39}\text{Ar}$  plateau dates of  $24.2 \pm 0.4$  and  $23.8 \pm$   
159  $0.1$  Ma; the latter date was obtained on a >100 m-thick mafic sill characterized by plagioclase phenocrysts up to 3  
160 cm in size (Fornari et al. 2002). About 75 km to the SSE, a ~1-km-thick section of red beds includes >15 basalt  
161 levels; lava flows near the base and top of the section yielded whole-rock  $^{40}\text{Ar}$ - $^{39}\text{Ar}$  dates of  $23.5 \pm 0.1$  and  $23.6 \pm$   
162  $0.1$  Ma, respectively, whereas a mafic dyke cutting several flows and sills yielded a plateau date of  $23.5 \pm 0.1$  Ma;  
163 these coinciding dates over a stratigraphic thickness of ~1 km indicate, again, that the corresponding mafic

164 magmatism was extremely productive at that time (~23.5 Ma in this case), and thus involved considerable mantle  
165 upwelling, resulting decompression melting and a very high heat flow into the overlying crust.

166 Crustal thickening in the NW-trending region of the Bolivian Orocline has developed since ~30 Ma (Picard et al.  
167 2008; Sempere et al. 2008 and references therein). The onset of crustal thickening thus coincided with the  
168 widespread development of mafic magmatism during the Late Oligocene and earliest Miocene.

169 Unlike igneous rocks from the Western Cordillera, silicic intrusive and volcanic rocks from the Eastern Cordillera  
170 of both Mesozoic (mostly ca. 225-200 Ma) and Tertiary (ca. 45-12.0 Ma) ages belong to the S-type, ilmenite series  
171 and resulted from sediment melting in a thickened continental crust with up to 30% of mantle component (Sugaki  
172 et al. 1981; Morgan et al. 1998; Lehmann et al. 2000; Mlynarczyk and Williams-Jones 2005; Maffione et al.  
173 2009).

174 The morphotectonic provinces are juxtaposed by a succession of parallel, north to south trending mineralized belts  
175 of Paleogene and Neogene ages. The Western Cordillera mostly comprises porphyry-type Cu-Mo-Au-Fe deposits,  
176 the Altiplano, polymetallic vein- and replacement-type Cu-Pb-Zn-Ag deposits and sedimentary Cu deposits, and  
177 the Eastern Cordillera, porphyry-type Sn-W-Ag deposits and associated polymetallic mineralization (Petersen  
178 1970; Sillitoe 1972, 1976; Clark et al. 1990; Mlynarczyk and Williams-Jones 2005; Fontboté 2018). The existence  
179 of metallogenic provinces (clusters of ore deposits with similar characteristics) in the Central Andes suggests  
180 control by regional or large scale geologic environments or processes, which in the region were governed by the  
181 quasi-continuous subduction along the western margin of the South American plate over the last ca. 300 My  
182 (Clark et al. 1976, 1990; Sillitoe 1976; Lehmann et al. 1990; Mlynarczyk and Williams-Jones 2005; Wörner et al.  
183 2018a,b; Fontboté 2018). In this convergent tectonic scenario, shortening, thickening and uplift favored the  
184 accumulation of magma in the upper crust, which was responsible for the magmatic-hydrothermal activity that  
185 formed the metalliferous deposits along metallogenic provinces (Fontboté 2018). This W to E zonation reflects the  
186 constraining character of the source regions and the decrease in the role of subduction-related processes evidenced  
187 by difference in granitoid type and series (Mlynarczyk and Williams-Jones 2005).

## 188 **Geological setting of the Bolivian Tin Belt**

189 The deposits selected for this study are distributed along the Bolivian segment of the Bolivian tin belt. The  
190 Bolivian tin belt is restricted to the Eastern Cordillera and stretches for about 900 km from ~150 km NNW of Lake  
191 Titicaca in Peru (e.g., the San Rafael world-class Sn deposit) through Bolivia to NW Argentina (e.g., the Piriquitas



192 Ag-Zn-Pb-Sn deposit; [Fig. 1A](#)). It has an arc shape with contrasting orientations in its northern half (running NW-  
193 SE) and southern half (running N-S), both segments connecting in the so-called “elbow of the Andes”, Bolivian  
194 orocline or Arica deflection ([Ahlfeld 1967](#); [Maffione et al. 2009](#)).

195 The Bolivian tin belt is genetically connected to two major periods of magmatism related to the Andean orogeny:  
196 the first is linked to intrusions of granitic plutons of Triassic to Jurassic ages and the second is related to plutonic,  
197 sub-volcanic and volcanic eruptive complexes of Oligocene to Miocene ages ([Turneaure 1971](#); [Sillitoe et al. 1975](#);  
198 [Evernden et al. 1977](#); [Lancelot et al. 1978](#); [Grant et al. 1979](#); [Clark et al., 1983, 1990, 2000](#); [McBride et al. 1983](#);  
199 [Kontak et al. 1987, 1990](#); [Mlynarczyk and Williams-Jones 2005](#); [Maffione et al. 2009](#); [Mišković et al. 2009](#);  
200 [Reitsma 2012](#); [Betkowski et al. 2017](#); [Cordani et al. 2019](#)). The Triassic granite intrusions were interpreted as  
201 typical of rift-related magmatism in a back-arc setting ([McBride et al. 1983](#); [Kontak et al. 1984, 1990](#); [Lehmann et  
202 al. 1990](#); [Miskovic et al. 2009](#); [Reitsma 2012](#)). The now-inverted rift system had an axis coinciding with the axis  
203 of the current Eastern Cordillera ([Sempere et al. 2002](#)). In the Cordillera Real, at the core of the Eastern Cordillera  
204 and the northern portion of the Bolivian tin belt, the oldest dated granitoids belong the Huato, Illampu, Yani,  
205 Huayna Potosí, Zongo and Taquesi plutons (ca. 280-200 Ma) and the youngest, to the Illimani, Quimsa Cruz and  
206 Santa Vera Cruz plutons (ca. 26-23 Ma; [Fig. 1A](#)). In the Peruvian segment of the Bolivian tin belt, known as the  
207 Cordillera de Carabaya, the oldest granitoids (San Gabán, Coasa, Limbani and Aricoma plutons; [Fig. 1A](#)) have a  
208 Triassic age (ca. 240-190 Ma). At the northern end of the Bolivian tin belt, the Nevado de Allincapac peralkaline  
209 volcano-plutonic complex comprises gabbros, diorites and nepheline syenites dated between 175 and 181 Ma  
210 ([Stewart et al. 1974](#); [Kontak et al. 1990](#)), and the youngest dated granitoids (San Rafael and Santo Domingo  
211 plutons) and their volcanoclastic equivalents of the Picotani Group ([Sandeman et al. 1997](#)) are of Late Oligocene  
212 age. South of the Cordillera Real, caldera complexes and huge volumes of Late Pliocene and Miocene (and up to  
213 recent) ignimbrite deposits of dacite and rhyolite composition formed as a result of changes in mantle melt  
214 productivity induced by the south-migrating subduction of the aseismic Juan Fernández Ridge and sporadic lower-  
215 crust and subcontinental lithospheric mantle delamination ([de Silva and Kay 2018](#) and references therein).

216 Compared to the Chilean and NW-Argentinian part of the Central Andes, rock suites in the Bolivian tin belt  
217 present higher abundance of Sn and sustained enrichment trends controlled by fractional crystallization ([Lehmann  
218 et al. 1990](#)). Despite being distinctly enriched in Sn, igneous rocks of Miocene porphyry systems in the Bolivian  
219 tin belt show concentrations of Ta, Zr and TiO<sub>2</sub> comparable to average upper crust and overall moderately  
220 fractionated rhyodacite and dacite bulk composition. In stark contrast, quartz-hosted melt inclusions in these rocks

221 yield highly fractionated rhyolitic compositions and enrichment in incompatible elements such as Ta, B, Cs, Li and  
222 Sn at concentrations comparable to those of tin granite systems worldwide ([Dietrich et al. 2000](#); [Lehmann et al.](#)  
223 [2000](#)). These authors propose that highly fractionated melts, chemically linked to the tin mineralization, mixed  
224 with primitive melts within magma chambers previous to shallow emplacement as sub-volcanic intrusions or  
225 volcanic eruption. Mio-Pliocene lithophile-rich obsidian glasses in felsic peraluminous tuffs in the Macusani area,  
226 in the Carabaya Cordillera in SE Peru, are representative of these highly evolved igneous rocks portions  
227 ([Pichavant et al. 1987, 1988a,b](#); [Cheilletz et al. 1990](#); [Poupeau et al. 1993](#); [Sandeman et al. 1997](#); [Nupen 2019](#)).  
228 Subsequent hydrothermal redistribution of Sn from igneous rocks magmatically enriched in this element led to  
229 enhancement of Sn concentrations. In this model, Sn inheritance from source and host rocks is discarded.  
230 Nevertheless, source sedimentary sequences played an important role in magma evolution by providing B and C<sub>org</sub>  
231 that depressed the solidus temperature of fractionating melts and induced a low oxidation state necessary for  
232 magmatic enrichment and hydrothermal redistribution of tin, respectively ([Lehmann et al. 1990, 2000](#); [Dietrich et](#)  
233 [al. 2000](#)). In addition, the high concentration of B and other volatile elements in melt inclusions in tin porphyries  
234 from the Bolivian tin belt led [Lehmann et al. \(2000\)](#) to conclude that the most likely crustal source was the Lower  
235 Paleozoic meta-sedimentary sequences.

236 Mineral deposits from the northern and southern halves of the Bolivian tin belt show contrasting ages and levels of  
237 emplacement ([Kelly and Turneure 1970](#); [Sillitoe et al. 1975](#); [Clark et al. 1976](#); [Lehmann et al. 1990](#); [Heuschmidt](#)  
238 [et al. 2002](#); [Kontak and Clark 2002](#); [Slater et al. 2020](#)). In the northernmost part, the ore deposits are mainly of Sn-  
239 W vein- and “manto”- (stratabound mineralization) type related to batholiths of Triassic and Oligocene age, whilst  
240 in the southernmost segment of the belt, mineralization is Miocene, usually shallower and appears as Sn, Sn-W  
241 and Sn-polymetallic veins formed in the epithermal and xenothermal environments ([Fig. 1](#)). The mineralized  
242 stocks and adjacent wall rocks usually present vertically and laterally zoned hydrothermal alteration, with  
243 abundant quartz - tourmaline - muscovite assemblages at high-temperature mineralization centers grading outward  
244 to phyllic, propylitic and, occasionally, silicified, advanced argillic lithocaps ([Sillitoe et al. 1975, 1998](#); [Harlaux et](#)  
245 [al. 2020](#); [Lehmann et al. 2000](#)). Lithocaps are only found in the southern part of the Bolivian tin belt, where  
246 volcanic domes genetically linked to the mineralization are only shallowly eroded ([Sillitoe et al. 1998](#)). Detailed  
247 descriptions of deposits from the Bolivian tin belt are given by [Ahlfeld and Schneider-Scherbina \(1964\)](#), [Kelly and](#)  
248 [Turneure \(1970\)](#), [Heuschmidt et al. \(2002\)](#) and [Arce-Burgoa \(2009\)](#).

## 249 **Methodology**

### 250 **Studied samples and their localities**

251 The studied cassiterite crystals belong to nine ore deposits/districts distributed along the Bolivian segment of the  
252 Bolivian tin belt (Fig. 1A-B).

#### 253 ***Milluni-Kellhuani district***

254 The Milluni-Kellhuani Zn-Cu-W-Bi district is located in the northernmost part of the La Paz department and sits at  
255 the northern part of the Cordillera Real, ~ 5 km south of the Triassic Huayna-Potosi granite (Gillis et al. 2006;  
256 Cordani et al. 2019). Vein and stratabound mineralization are hosted in Silurian quartzites of the Catavi Formation.  
257 Mineralization consists primarily of early quartz, tourmaline and cassiterite (Sn-W stage) and later sulfides such as  
258 chalcopyrite, sphalerite, pyrrhotite and pyrite (sulfide stage; Lehmann et al. 1985). Fluid inclusions in cassiterite  
259 from the Milluni mine yielded trapping temperatures of 410-500°C (corrected for depositional pressures of 0.5-1  
260 kbar) and salinities of 5-25 wt% NaCl equiv. (Kelly and Turneaure 1970).

261 In the central part of the district, the Chacaltaya granite porphyry stock, which shows extreme hydrothermal  
262 alteration (greisenization), intruded the Paleozoic metasedimentary rocks (Lehmann 1985). Mineralization in the  
263 greisen is mostly composed of cassiterite accompanied by fine- and medium-grained quartz, muscovite,  
264 tourmaline, fluorite and siderite. K-Ar dating of greisen muscovite yielded a date of  $210 \pm 6$  Ma (McBride et al.  
265 1983).

266 The analyzed cassiterite crystals belong to two samples of quartz-cassiterite veins from the Kellhuani deposit (Kell  
267 A and Kell B) about 3 km east of the granite porphyry. Crystals are dark red in color, euhedral and subhedral and  
268 have sizes typically larger than 500  $\mu\text{m}$  and exceptionally up to 5 mm across (Fig. 2A); some contain inclusions of  
269 pyrrhotite and are intergrown with quartz and tourmaline.

#### 270 ***Viloco – Rosario de Araca district***

271 The Viloco – Rosario de Araca district is located in the La Paz department, 70 km SE of La Paz, on the  
272 southwestern flank of the Quimsa Cruz Cordillera in the southern segment of the Cordillera Real. NE-trending  
273 peribatholithic veins are hosted by Ordovician quartzites of the Amutara Formation close to their contact with the  
274 Oligocene Quimsa Cruz granodiorite and porphyritic monzogranite batholith (Everden et al. 1977; Gillis et al.

275 2006; Artiaga et al. 2013). K-Ar dating of igneous biotite and muscovite from the Quimsa Cruz batholith yielded  
276 dates between 23 and 26 Ma (Ahlfeld and Branisa 1960; Cordani 1967 in Clark and Farrar 1973; Evernden et al.  
277 1977; McBride et al. 1983; Gillis et al. 2006). U-Pb zircon dates in the Quimsa Cruz batholith at Mina Argentina  
278 and Mina Viloco are  $25.65 \pm 0.41$  and  $26.02 \pm 0.41$  Ma, respectively (Gillis et al. 2006).

279 Vein mineralogy comprises early high-temperature cassiterite, wolframite, löllingite and pyrrhotite associated with  
280 quartz-tourmaline gangue and a second lower temperature sulfide stage with arsenopyrite, sphalerite, galena,  
281 chalcopyrite and stannite in association with sulfosalts and carbonate gangue minerals (Sugaki et al. 1985; Artiaga  
282 et al. 2013). Fluid inclusions in cassiterite crystals from the Araca deposit yielded salinities of 23-35 wt% NaCl  
283 equiv. and homogenization temperatures ( $T_h$ ) of 340-489°C (Kelly and Turneaure 1970). Cassiterite from this  
284 district is world renowned for its large, highly lustrous, black to caramel-color, twinned and euhedral crystals of  
285 gem quality.

286 Cassiterite crystals studied from this district belong to seven samples collected from the Viloco deposit (Vil 1-  
287 540d, Vil-2-sn-a, Vil2-453-2b, Vil2-453-2c, Vil4-453-2b, Vil41-xa and Vil5e). In the studied samples, cassiterite  
288 is the dominant phase and appears as dark euhedral and subhedral fractured crystals more than 500  $\mu\text{m}$  and up to 5  
289 cm across (Fig. 2B). Twinning is a common feature of most cassiterite grains. Crystals present sharp edges in  
290 contact with an assemblage of quartz and corroded pyrite-marcasite after pyrrhotite (Fig. 2C). Small sulfide  
291 veinlets, less than 200  $\mu\text{m}$  in width and containing chalcopyrite and arsenopyrite, cut cassiterite grains.

### 292 ***San José – Itos district (Oruro city)***

293 The San José and Itos mines are located on the western side of the city of Oruro, 200 km SE of La Paz, and sit  
294 close to the contact between the Altiplano and the Eastern Cordillera. Metallic mineralization is genetically  
295 associated to a Miocene dome and volcanic complex intruding into and extruding over Paleozoic shales and  
296 sandstones (Chace 1948a,b; Redwood and Macintyre 1989; Sugaki et al. 2003). K-Ar dating of biotite, sericite and  
297 K-feldspar in rhyodacite domes yielded dates between 15 and 19 Ma (McBride et al. 1983; Redwood and  
298 Macintyre 1989). Mineralization appears as Ag-Sn-rich veins and disseminations hosted by domes of 16.1 Ma  
299 (Redwood and Macintyre 1989) and hydrothermal breccias of the homonymous San José and Itos stocks (Sillitoe  
300 et al. 1975; Sugaki et al. 1990).

301 Mineralization occurred in three stages. The first stage is Sn-rich and composed of euhedral quartz, As-rich pyrite,  
302 cassiterite and arsenopyrite. The second stage is sulfosalt-rich and comprises franckeite and cylindrite coatings

303 over previous assemblages. The third stage is composed of sphalerite and stannite-group minerals partially  
304 replaced by franckeite and Ag-rich sulfosalts (stephanite, andorite), acanthite and galena as open-space infilling  
305 and associated to kaolinite, dickite and alunite (Sillitoe et al. 1975; Pastor et al. 2015). Bismuth-rich andorite and  
306 ramdohrite and Sb-rich bismuthinite are also found in the San José mine (Keutsch and De Brodtkorb 2008). Fluid  
307 inclusions in cassiterite from the Oruro district yielded  $T_h$  of 389-474°C and salinities of 8.9 to 26.3 wt% NaCl  
308 equiv. (Kelly and Turneure 1970).

309 Here studied cassiterite crystals are from six samples collected from the Itos (It-180b, It-250b and It-250d) and  
310 San José (1233, 1241 and 1433) mines. Cassiterite forms massive aggregates of crystals ranging in size from a few  
311 tens of microns up to 500  $\mu\text{m}$ . Most aggregates are highly corroded and show abundant porosity that draws  
312 secondary spongy textures (Fig. 2D). Cassiterite aggregates occur usually assembled with quartz, pyrite-marcasite,  
313 arsenopyrite and late sulfosalts such as jamesonite that replaced the previous sulfide assemblage. Locally, euhedral  
314 cassiterite crystals are intergrown with quartz (Fig. 2E).

### 315 *Poopó district*

316 The Poopó deposit is located 48 km S of Oruro and 240 km SE of La Paz, near the border between the Altiplano  
317 and the Eastern Cordillera delineated by the NNW–SSE striking Poopó regional fault. The Sn-Ag low-sulfidation  
318 epithermal mineralization consists of a vein system extending along the N-S striking Poopó-Uyuni fault system.  
319 Veins are hosted by Silurian black shales and sandstones of the Llallagua, Uncía and Belén Formations that were  
320 intruded by Miocene dacite porphyry stocks and covered by associated ignimbrite deposits (Heuschmidt et al.  
321 2002). Conspicuous cataclastic textures and occurrence of several stages of breccia cementation by hydrothermal  
322 minerals suggest that ore mineralization was coeval with the tectonic activity of the Poopó-Uyuni fault (Torres et  
323 al. 2019).

324 The mineralogy of the deposit consists primarily of quartz, sulfides (sphalerite, wurtzite, pyrite and marcasite),  
325 cassiterite, which locally amounts to about 10% of the vein assemblage, and a plethora of Ag-Pb-Cu sulfosalts  
326 (Torres et al. 2019). Cassiterite crystallized at two stages during the formation of the deposit: the first one, with  
327 quartz and sphalerite-pyrite (Zn-Sn stage) and the second one, along with tin sulfides and sulfosalts (Sn stage).

328 Analyzed cassiterite grains are from sample Poo-St-1c, which was collected from the Santo Toribio vein system,  
329 and belong to the first generation crystallized during the Zn-Sn stage. In the studied samples, cassiterite appears as  
330 small aggregates of crystals with sizes between a few tens of microns and 1 mm. Cassiterite is often intergrown

331 with pyrrhotite that has been pervasively replaced by an assemblage of pyrite and marcasite along with siderite  
332 (Fig. 2F).

### 333 ***Huanuni district***

334 The Huanuni Sn-W-Pb-Ag-Zn world-class district, located in the homonymous city in the Oruro department, 275  
335 km SE of La Paz, is the largest tin producer in Bolivia and in 2018 its production accounted for over half the total  
336 tin production of the country. This deposit is considered to be mesothermal or xenothermal (Cacho et al. 2019).  
337 Mineralization is mostly hosted by Silurian quartzites, shales and siltstones of the Llallagua, Uncía and Cancañiri  
338 Formations, which are discordantly overlain by pyroclastic series of the Miocene Morococala Formation (Koeppen  
339 et al. 1987). Paleozoic rocks were intruded by Miocene porphyric dikes peripheral to the mineralized area, which  
340 are thought to be genetically connected to the hydrothermal mineralization (Redwood 1993; Heuschmidt et al.  
341 2002; Cacho et al. 2019). Cassiterite-rich veins are restricted to the central area of the deposit, in the Pozokoni hill,  
342 and tin concentration decreases towards the periphery in the Zn-Pb-Ag La Suerte and Bonanza mines, which are  
343 rich in sphalerite, galena and sulfosalts.

344 Hypogene mineralization in the Pozokoni area comprises three stages. The first stage consists of quartz, base-  
345 metal sulfides and cassiterite. The second stage records abundant crystallization of schorl and, akin the first stage,  
346 is also rich in base-metal sulfides as well as Co-Ni minerals, late chamosite and siderite followed by native  
347 bismuth, wolframite and cassiterite. The third stage is characterized by stannite and sphalerite. There was, in  
348 addition, ample crystallization of supergene minerals dominated by phosphates, sulfates and carbonates rich in Fe,  
349 Cu and Pb (Cacho et al. 2019). Fluid inclusions in quartz from quartz-cassiterite veins yielded  $T_h$  up to 425°C and  
350 salinities up to 26 wt% NaCl equiv. (Sugaki et al. 1988b; Müller et al. 2001; Arce-Burgoa 2009).

351 Studied cassiterite grains belong to six samples collected from the Pozokoni hill mine area (Hua240, Hua240-1a,  
352 Hua240-1b, Hua240-3c, Hua-MU-7b and Hua-MU-8). Cassiterite is the most abundant phase in the studied  
353 samples and appears as large (>1 to 5 mm) subhedral and anhedral crystals often forming centimetric aggregates  
354 with abundant porosity (Fig. 2G). Twinning is a common feature of Huanuni cassiterite. The edges of the  
355 cassiterite crystals are usually sharp in contact with quartz and irregular in contact with marcasite-pyrite and  
356 pyrrhotite. In addition, cassiterite crystals are wrapped by stannite, which also lines fractures and voids within  
357 cassiterite.

358 ***Llallagua district***

359 The Llallagua district is located next to the homonymous city, 300 km SE of La Paz and 80 km SE of Oruro. It is  
360 one of the world's largest porphyry-tin deposits with a historical production exceeding 500,000 t of tin (Ahlfeld  
361 and Schneider-Scherbina 1964). The deposit lies in the hydrothermally altered La Salvadora stock, which is  
362 composed mostly of porphyry breccias. The stock is pervasively altered to tourmaline in the central areas and at  
363 depth grading upwards and outwards to intense sericitization and finally to chloritization and argillitization  
364 (Betkowski et al. 2017). The stock is cut by igneous and hydrothermal breccias. Tin mineralization appears  
365 disseminated and in quartz-cassiterite-sulfide veins restricted to early, high-temperature stages (Kelly and  
366 Turneure 1970). In veins, cassiterite is assembled with pyrrhotite and apatite (Turneure 1935; Gordon 1944;  
367 Kempe et al. 2008). Fluid inclusions in cassiterite and quartz yielded salinities up to 8.2 and 26 wt% NaCl equiv.,  
368 respectively, and  $T_h$  up to 593°C (Kelly and Turneure 1970).

369 Reported radiometric dates are 43.8 Ma (Sm-Nd fluorapatite age; Rakovan et al. 1997), 42.4 Ma (Pb-Pb zircon  
370 evaporation geochronology; Kempe et al. 2008), 23.4 and 19.0 Ma (U-Pb monazite; Kempe et al. 2008 - SHRIMP  
371 and Kohn and Vervoort 2008 - LA-ICP-MS, respectively). Recent U-Pb cassiterite dating by Neymark et al.  
372 (2018) yielded a date of  $20.0 \pm 2.5$  Ma.

373 Analyzed cassiterite grains are from sample LL-4, which was collected from the Siglo XX mine. In the studied  
374 sample, cassiterite occurs as anhedral, fractured and corroded relatively large crystals, with sizes in the range  
375 between 200 and 500  $\mu\text{m}$ , often showing simple twinning (Fig. 2H). Cassiterite grains are intergrown with quartz,  
376 tourmaline and small pyrite crystals with cores replaced by marcasite.

377 ***Colquechaca deposit***

378 The Ag-(Zn-Sn-Pb) Colquechaca deposit is located in the Hermoso hill in Colquechaca, northern Potosí  
379 department, 465 km SW of La Paz and 96 km N of Potosí. Mineralized veins are hosted by the Miocene  
380 Colquechaca volcanic complex in which a stratovolcano of andesitic to dacitic composition was intruded by a  
381 series of porphyritic rhyodacitic and quartz-latite domes. The volcanic complex is emplaced over metasedimentary  
382 Ordovician (Amutara Formation) and Silurian (Cancañiri and Uncía Formations) series and the discordantly  
383 overlying Jurassic (Ravelo Formation), Jurassic-Cretaceous (Kondo and Kosmina Formations) and Cretaceous  
384 (Tarapaya Formation) sedimentary series (Martínez and Vargas 1990; Claire et al. 1996; Díaz 1997; Heuschmidt

385 [et al. 2002](#)). K-Ar dating of igneous biotite, K-feldspar and plagioclase yielded dates in the range between 19.8  
386 and 22.6 Ma ([Ahlfeld and Schneider-Scherbina 1964](#); [Thormann 1966](#); [Evernden et al. 1977](#); [Grant et al. 1979](#)).

387 Xenothermal vein mineralization hosts a cassiterite- and stannite-rich zone along with tourmalinization in the  
388 innermost part of the deposit, which grades outwards to a sulfide- and Ag-sulfosalt-rich domain with phyllic  
389 alteration ([Grant et al. 1979](#); [Heuschmidt et al. 2002](#)).

390 Analyzed cassiterite grains are from two samples collected from the Hilarion vein in the Cerro Ánimas area  
391 (Colq6a and 1353). Cassiterite grains form mostly anhedral crystals of approximately 400  $\mu\text{m}$  across ([Fig. 2I](#)). The  
392 edges of these crystals are sharp in contact with quartz and tourmaline and more irregular in contact with sulfides  
393 (pyrite, sphalerite and galena). Local leather-shaped radial aggregates of cassiterite appear in contact with most  
394 massive, anhedral cassiterite crystals ([Fig. 2J](#)).

#### 395 ***Huari Huari district***

396 The Huari Huari xenothermal vein deposit is located 25 km NE of Potosí in the Potosí department, 400 km SW of  
397 La Paz. Vein and much restricted stratabound metallic mineralizations are hosted by slates and quartzites of the  
398 Ordovician San Benito and Silurian Cancañiri and Uncía Formations, which are unconformably overlain by  
399 Cretaceous sandstones of the La Puerta Formation. The sedimentary sequence was intruded by small dacite domes  
400 and stocks of alleged Miocene age ([Sugaki et al. 1983](#); [Torró et al. 2019a](#)).

401 Polymetallic veins are mostly of the fissure-filling type and NNE-oriented. Vein mineralogy consists primarily of  
402 an early assemblage of quartz, cassiterite and pyrrhotite followed by an assemblage dominated by base-metal  
403 sulfides (sphalerite, galena) and pyrite and a final stage dominated by Ag-Pb sulfosalts ([Torró et al. 2019a](#)).

404 Analyzed cassiterite grains belong to three samples collected from the Antón Bravo vein (2018hh15, 2018hh2b  
405 and 2018hh3a). In the studied samples, cassiterite is rare and mostly of the “*needle tin*” variety (i.e., small  
406 micrometric acicular crystals) forming radial aggregates up to 500  $\mu\text{m}$  in size. Nevertheless, in the deepest parts of  
407 the Antón Bravo vein, cassiterite appears as subhedral crystals in assemblage with quartz and a complex  
408 paragenesis of sulfides and sulfosalts ([Fig. 2K](#)).



409 *Ánimas – Chocaya – Siete Suyos district*

410 The Ánimas - Chocaya - Siete Suyos district is located about 150 km S of Potosí in the Potosí department, 520 km  
411 SW of La Paz. This district sits in the western flank of the Eastern Cordillera, close to the triple junction that is  
412 drawn by the Eastern Cordillera, the Western Cordillera and the Altiplano. Mineralization is genetically associated  
413 with the Miocene Chocaya volcanic caldera complex, which is 9 km in diameter and conformed of a pile of lava  
414 and pyroclastic deposits of dacitic composition intruded by a central dome of the same composition. The volcanic  
415 complex is hosted by Ordovician sandstones and slates unconformably overlain by Oligocene-Miocene sandstones  
416 and tuffs of the Quehua Formation (Ahlfeld and Schneider-Scherbina 1964; Grant et al. 1979; Arce-Burgoa 2009;  
417 Torró et al. 2019b). Reported K-Ar dates in the area are of  $13.8 \pm 0.2$  Ma (unweighted mean value) for biotite from  
418 unaltered volcanic rocks, and of  $12.5 \pm 0.2$  Ma for a sericitized sample (whole-rock age; Grant et al. 1979).

419 Mineralization in the district occurs as banded and massive oxide and sulfide ore vein infillings (Sugaki et al.  
420 1983). Torró et al. (2019b) determined a three-stage paragenetic sequence including an early low-sulfidation stage  
421 dominated by cassiterite, pyrrhotite, arsenopyrite and high-Fe sphalerite, a second intermediate-sulfidation stage  
422 dominated by pyrite, marcasite, sphalerite and stannite and a late intermediate-sulfidation stage dominated by  
423 galena and Ag-Pb-Sn sulfosalts. Cassiterite is much abundant in the Siete Suyos deposit and less common in the  
424 Ánimas deposit. In the Chocaya deposit, cassiterite is virtually absent (Torró et al. 2019b).

425 Analyzed cassiterite grains are from the 10 vein in the Siete Suyos mine (2018-7S2 and 1380) and from the  
426 Colorada vein in the Ánimas mine (2018-An12 and Ani5c). The studied grains are subhedral and anhedral and  
427 range in size from 100 to 600  $\mu\text{m}$ . Often, small crystals of cassiterite form aggregates up to 1 mm across. These  
428 aggregates are intergrown with quartz, sulfides and sulfosalts in hexagonal arrangements (Fig. 2L) after hexagonal  
429 pyrrhotite (see Torró et al. 2019b).

430 **Analytical methods**

431 A total of 32 thick sections belonging to nine deposits from the Bolivian tin belt were selected: two for Kellhuani,  
432 seven for Viloco, six for San José-Itos (Oruro), one for Poopó, six for Huanuni, one for Llallagua, two for  
433 Colquechaca, three for Huari Huari and five for Ánimas - Chocaya - Siete Suyos.

434 ***Petrography (optical microscope, SEM and SEM-CL)***

435 Mineralogy and textures in thick polished sections were studied by optical microscopy using reflected light in  
436 order to select the optimal cassiterite specimens for subsequent geochemical analysis. A selection of the polished  
437 sections was also examined with an environmental scanning electron microscope (SEM) Quanta 200 FEI, an XTE  
438 325/D8395 (Thermo Fisher Scientific, Waltham, MA, USA) equipped with an INCA Energy 250 EDS  
439 microanalysis system at the Centres Científics i Tecnològics of the University of Barcelona (CCiT-UB). Operating  
440 conditions were 20 keV accelerating voltage and 5 nA in backscattered electron (BSE) mode.

441 ***Electron probe microanalysis (EPMA)***

442 A total of 268 analyses of cassiterite (major and minor elements) were carried out using a five-channel JEOL JXA-  
443 8230 electron probe microanalyzer (EPMA; Jeol Ltd., Tokyo, Japan) at the CCiT-UB, operated at 20 kV  
444 acceleration voltage, 20 nA beam current, and with a beam diameter of 5  $\mu\text{m}$ . Analytical standards and lines used  
445 for analyses were:  $\text{ZrO}_2$  (Zr,  $L\alpha$ ),  $\text{Nb}_2\text{O}_5$  (Nb,  $L\alpha$ ),  $\text{SnO}_2$  (cassiterite,  $L\alpha$ ), FeO (Fe,  $K\alpha$ ),  $\text{Ta}_2\text{O}_5$  (Ta,  $L\alpha$ ), MnO  
446 (rhodonite,  $K\alpha$ ),  $\text{TiO}_2$  (rutile,  $K\alpha$ ). The EPMA data are reported in [Supplementary Table S1](#).

447 ***Laser ablation – inductively coupled plasma – sector field – mass spectrometry (LA-ICP-SF-MS)***

448 A total of 330 analyses of cassiterite trace element concentrations and U-Pb isotopic compositions were carried out  
449 at ETH Zürich, Switzerland, by laser ablation – inductively coupled plasma – sector field – mass spectrometry  
450 (LA-ICP-SF-MS) using a RESOLUTION S-155 (ASI/Applied Spectra) 193 nm ArF excimer laser system attached to  
451 an Element XR (Thermo) sector-field ICP-MS. We have used a laser repetition rate of 3 Hz, a spot diameter of 43  
452  $\mu\text{m}$  and a laser energy density on sample of about  $3.5 \text{ J}\cdot\text{cm}^{-2}$ . The sample surface was cleaned before each analysis  
453 by three pre-ablation pulses. Ablation was performed in a dual-volume, fast-washout S-155 ablation cell (Laurin  
454 Technic) fluxed with carrier gas consisting of about  $0.5 \text{ L}\cdot\text{min}^{-1}$  He and make-up gas consisting of about  $1 \text{ L}\cdot\text{min}^{-1}$   
455 Ar and  $2 \text{ mL}\cdot\text{min}^{-1}$   $\text{N}_2$ . The ablated aerosol was homogenized via flushing through a squid device before being  
456 introduced in the plasma.

457 The ICP-MS instrument is equipped with a high capacity ( $80 \text{ m}^3\cdot\text{h}^{-1}$ ) interface pump to achieve, in combination  
458 with jet sampler and normal H-skimmer cones, a detection efficiency (based on U in NIST SRM612 glass) in the  
459 range of 2% ([Guillong et al. 2020](#)). The instrument was optimized for maximum sensitivity on the entire mass  
460 range while keeping the production of oxides low ( $^{248}\text{ThO}^+ / ^{232}\text{Th}^+ \leq 0.15\%$ ) and the U/Th ratio at about 1 (on

461 NIST SRM612 glass). The list of analyzed isotopes and corresponding dwell times is provided in [Supplementary](#)  
462 [Table S2](#). A total of 40 mass scans (~1.04 s sweep time each) were acquired over 40 s measurement (20 s of  
463 background measurement followed by 20 s of sample ablation).

464 For trace element quantification, the resulting intensities were subsequently processed offline with the standalone  
465 version 1.3.2 of the SILLS program ([Guillong et al. 2008](#)). The USGS GSD-1G glass ([Guillong et al. 2005](#)) was  
466 used as the primary reference material for trace element quantification and instrumental drift correction using  
467 conventional standard-sample bracketing. The Fe concentrations obtained by electron microprobe were used as  
468 internal standards for relative sensitivity corrections. The analyzed In intensities on masses 113 and 115 were  
469 corrected for interferences by subtracting the contribution of  $^{113}\text{Cd}$  and  $^{115}\text{Sn}$ , respectively, based on the measured  
470  $^{111}\text{Cd}$  and  $^{118}\text{Sn}$  intensities and using natural isotope ratios for Cd and Sn recommended by IUPAC. Because of the  
471 very high  $^{118}\text{Sn}$  signal in cassiterite (>5,109 cps) and resulting elevated gas blanks on masses 115 and 118, the  
472 extent of the correction is much higher in the case of  $^{115}\text{In}$  than in the case of  $^{113}\text{In}$ , especially since the analyzed  
473 cassiterite crystals all show very low Cd concentrations (<1 ppm). Therefore, we only considered the  
474 concentrations based on the interference-corrected  $^{113}\text{In}$  intensities. The data are reported in [Supplementary Table](#)  
475 [S3](#). The analytical reproducibility and accuracy were checked by repeated measurements of the homogeneous  
476 NIST SRM610 glass ([Jochum et al. 2011](#)) reference material. Reproducibility ranges from 10 to 15% ( $2\sigma$ ) relative  
477 for most elements. The quoted uncertainties for each individual analysis correspond to the internal ( $2\sigma$ ) statistical  
478 error and analytical reproducibility propagated by quadratic addition. The results are accurate within these  
479 calculated uncertainties ([Supplementary Table S3](#)).

480 For U-Pb dating, the measured intensities were subsequently processed offline with the Igor Pro Iolite v2.5  
481 software ([Hellstrom et al. 2008](#)), using the VizualAge data reduction scheme ([Petrus and Kamber 2012](#)).  
482 Background-subtracted intensities were used to calculate isotope ratios, which were corrected for laser-induced  
483 Pb/U fractionation (after [Paton et al. 2010](#)), instrumental mass discrimination and drift by conventional standard-  
484 sample bracketing, against rutile reference material R10 (using isotope ratios from [Luvizotto et al. 2009](#)). No  
485 common Pb correction was carried out. U-Pb age calculations and data plotting were performed using the IsoplotR  
486 toolkit ([Vermeesch 2018](#)). The lack of matrix-matched primary reference material most certainly makes the  
487 obtained dates inaccurate. Nevertheless, in another session using exactly the same analytical parameters as here  
488 (including the use of R10 rutile as primary reference material), we have measured three cassiterite samples of  
489 known age from the San Rafael granite, Peru (ca. 24 Ma, samples and unpublished dates courtesy of K.

490 Kouzmanov, University of Geneva, 2020) and obtained a systematic offset of ca. 8% relative on lower intercept  
491 dates. This offset is in any case smaller than the relative uncertainty obtained on the cassiterite dates obtained here  
492 (13-53% relative), except for samples Kell-A and Kell-B (3-6% relative). For these two samples, a relative  
493 uncertainty of 8% was therefore propagated in the uncertainty of the dates by quadratic addition to account for the  
494 matrix effects. The data from unknowns and rutile reference material are provided in [Supplementary Table S4](#).

## 495 **Results**

### 496 **Major- and minor-element composition**

497 The EPMA data of cassiterite grains from the studied Bolivian deposits show a generally restricted range in  
498 composition, with  $\text{SnO}_2 > 97.7$  wt%. Of the other elements, only Fe yields concentrations that are generally above  
499 its lower limit of detection (L.O.D.) with maximum concentrations of 2.34 wt%. Iron is particularly high in  
500 cassiterite from the Colquechaca deposit, with concentrations systematically higher than 0.5 wt%. The rest of the  
501 elements yields values mostly below the respective L.O.D. with some anomalous values for  $\text{TiO}_2$  (up to 0.92 wt%  
502 in a sample from Kellhuani) and  $\text{Nb}_2\text{O}_5$  (up to 0.25 wt% in samples from Viloco and Huanuni).

### 503 **Trace-element composition**

504 Significant effort was made to report only the concentration of elements whose variations respond to solid  
505 solutions and not to mixed mineral analyses by analyzing mineral volumes free of obvious inclusions and by  
506 selecting only stable signal intervals in LA-ICP-MS spectra ([Supplementary Fig. S1](#)). A complete set of box plots  
507 showing the concentration of all elements analyzed by LA-ICP-MS is available in [Supplementary Figure S2](#), and a  
508 selection of them is shown in [Fig. 3](#). Concentration values will be hereinafter reported as the interquartile range  
509 (IQR) unless otherwise specified.

510 Cassiterite from the Bolivian tin belt shows a relatively wide trace element compositional spectrum, mainly  
511 subordinated to W (1987-53.7 ppm) and Ti (918-27.8 ppm) contents. The concentration of high-field-strength  
512 elements (HFSE) is relatively low, including Zr (17.0-0.528 ppm), Hf (0.293-0.0455 ppm), Nb (4.84-0.037 ppm)  
513 and Ta (0.0924-0.0126 ppm). The highest concentrations of Nb and Ta are found in cassiterite samples from the  
514 Kellhuani (60.8-2.26 ppm Nb and 0.639-0.0403 ppm Ta), Llallagua (18.5-0.989 ppm Nb and 0.185-0.0143 ppm  
515 Ta) and Viloco (6.19-0.0515 ppm Nb and 0.135-0.0138 ppm Ta) deposits, and the lowest, in cassiterite samples  
516 from the Poopó (0.027-0.0126 ppm Nb and 0.0196-0.0133 ppm Ta) and Ánimas - Chocaya - Siete Suyos (0.059-

517 0.00971 ppm Nb and 0.0165-0.00873 ppm Ta) deposits. Manganese concentrations (9.36-1.61 ppm) are  
518 consistently lower than Fe concentrations. Maximum Mn concentrations are recorded in samples from the  
519 Colquechaca (40.4-3.28 ppm) and Poopó (17.5-8.38 ppm) deposits, and the lowest concentrations, in samples from  
520 the Llallagua deposit (<L.O.D.). Most analyzed cassiterite samples from the Bolivian tin belt yield  
521  $(\text{Fe}+\text{Mn})/(\text{Nb}+\text{Ta}) \gg 1$  at relatively constant Mn (and Fe+Mn) and variable Nb+Ta (Fig. 4A-B; see also  
522 [Supplementary Fig. S3](#)). In the Nb vs Ta plot (Fig. 4C), cassiterite samples from the Bolivian tin belt plot mostly  
523 around the Nb:Ta = 2:1 ratio line, Nb concentrations being by up to four orders of magnitude higher than Ta  
524 concentrations.

525 Concentrations of Zr and Hf are highest in samples from the Kellhuani (28.5-3.24 ppm Nb and 0.965-0.141 ppm  
526 Ta), Huanuni (17.5-1.89 ppm Nb and 0.432-0.0731 ppm Ta) and Llallagua (16.5-3.92 ppm Nb and 0.387-0.0955  
527 ppm Ta) deposits, and lowest in samples from the Ánimas - Chocaya - Siete Suyos (0.059-0.00971 ppm Nb and  
528 0.0165-0.00873 ppm Ta) and Poopó (0.027-0.0126 ppm Nb and 0.0196-0.0133 ppm Ta) deposits. The  
529 concentration of both elements yields a relatively good positive correlation mostly at  $\text{Zr}/\text{Hf} > 1$ , Zr concentrations  
530 being by up to one order of magnitude higher than Hf concentrations (Fig. 4D). Concentrations of Ti are highest in  
531 cassiterite samples from Kellhuani (3065-561 ppm), Huari Huari (1391-383 ppm) and Llallagua (1303-382 ppm)  
532 and lowest in samples from Ánimas - Chocaya - Siete Suyos (19.1-4.65 ppm) and Poopó (4.38-2.02 ppm). There is  
533 a fairly positive correlation between Ti and Zr at  $\text{Ti}/\text{Zr} > 1$ , similar to most cassiterite worldwide (Fig. 4E). In  
534 contrast, Ti does not show clear correlation with U, and Ti/U ratios are normally higher than 1, with a composition  
535 similar to global cassiterite in terms of both elements (Fig. 4F). Titanium shows fairly positive correlation with Sc  
536 for most samples plotting between the lines defined by Sc:Ti 1:1 and 1:2 ratios in Fig. 4G. Nevertheless, cassiterite  
537 compositions for some of the studied deposits align preferably along one or the other, with most samples from the  
538 Kellhuani and Viloco deposits lying along the Sc:Ti = 1:2 ratio line and most samples from the Ánimas - Chocaya  
539 - Siete Suyos and Poopó deposits lying around the 1:1 ratio line. Finally, there is a strong positive correlation  
540 between V and Sc (Fig. 4H).

541 As for the concentrations of critical metals others than the aforementioned ones ([European Commission 2017](#)), In  
542 (96.9-9.78 ppm), Ga (92.1-3.03 ppm) and Ge (3.92-0.776 ppm) vary by orders of magnitude in crystals from  
543 individual deposits/districts and from deposit to deposit. Gallium and In are distinctively concentrated in cassiterite  
544 from the Oruro (801-31.8 ppm In and 377-71 ppm Ga), Huari Huari (889-96.9 ppm In and 438-53.5 ppm Ga) and  
545 Ánimas - Chocaya - Siete Suyos (582-174 ppm In and 292-53.1 ppm Ga) deposits. Gallium is also relatively high

546 in the Colquechaca deposit (438-53.5 ppm). The concentrations of In and Ga are consistently very low in the  
547 Viloco (63.4-10.0 ppm In and 5.43-1.59 ppm Ga), Kellhuani (30.9-2.15 ppm In and 3.11-0.932 ppm Ga),  
548 Llallagua (25-6.5 ppm In and 53.1-23.0 ppm Ga) and Poopó (4.7-3 ppm In and 43.3-27.3 ppm Ga; [Fig. 3](#))  
549 deposits.

550 REE values show a relative wide dispersion in grains analyzed within individual deposits/districts ([Figs. 3 and 5](#),  
551 [Table 1](#)). Cassiterite samples from Kellhuani (IQR[ $\Sigma$ REE] = 6.18-2.19 ppm) yield the highest REE  
552 concentrations, and samples from the Ánimas - Chocaya - Siete Suyos district (IQR[ $\Sigma$ REE] = 2.12-1.44 ppm), the  
553 lowest REE concentrations. In chondrite-normalized (CN) spider plots ([Fig. 5](#)), studied cassiterite grains show  
554 rather parallel patterns with irregular tetrad distribution, general negative Ce and positive Gd and Tb anomalies  
555 and enrichment in MREE relative to LREE and HREE ( $[\Sigma\text{LREE}/\Sigma\text{MREE}]_{\text{CN}}$  between 0.4 and 0.3,  
556  $[\Sigma\text{LREE}/\Sigma\text{HREE}]_{\text{CN}}$  between 1.6 and 0.6, and  $[\Sigma\text{MREE}/\Sigma\text{HREE}]_{\text{CN}}$  between 4.5 and 1.7).

#### 557 **U-Pb cassiterite geochronology**

558 U-Pb isotopic analyses of cassiterite grains from the Kellhuani, Viloco, Huanuni and Llallagua deposits are  
559 presented in [Supplementary Table S4](#) and illustrated in [Fig. 6](#). Spot analyses from the four deposits form Tera-  
560 Wasserburg (T-W) isochrons defining lower-intercept dates of  $218.3 \pm 5.5$  Ma (Kellhuani),  $24.4 \pm 0.4$  Ma  
561 (Viloco),  $24.0 \pm 2.4$  Ma (Huanuni) and  $24.0 \pm 5.1$  Ma (Llallagua); concordant data is absent. U-Pb isotopic  
562 analyses on cassiterite grains from the other studied Bolivian deposits were inconclusive due to too low U contents  
563 and/or too high initial Pb.

## 564 **Discussion**

### 565 **Timing of Sn mineralization in the Bolivian tin belt**

566 Punctuated magmatism and petrogenetically related hydrothermal tin mineralization in the Bolivian tin belt  
567 occurred in the Late Triassic, Late Oligocene and Miocene ([Ahfeld 1967](#); [Turneure 1971](#); [Clark and Farrar 1973](#);  
568 [Evernden et al. 1977](#); [Grant et al. 1979](#); [McBride et al. 1983](#); [Clark et al. 1990](#); [Lehmann et al. 1990](#); [Sugaki et al.](#)  
569 [2003](#); [Gillis et al. 2006](#); [Neymark et al. 2018](#)). Accordingly, the metallogeny of the Bolivian tin belt results from  
570 multiple, discrete events that lead to similar anomalous Sn enrichment in a series of mineral deposits of different  
571 affiliation within the magmatic-hydrothermal family.

572 To contextualize our U-Pb cassiterite ages in the framework of the magmatic and metallogenic evolution of the  
573 Bolivian tin belt, a geochronologic chart with all available radiometric dates (excluding dates related to  
574 exhumation - thermochronology oriented studies, e.g., (U-Th-Sm)/He, fission track) has been produced (Fig. 7).  
575 For some of the studied deposits (Kellhuani, Viloco and Huanuni), our U-Pb cassiterite dates are the first  
576 geochronologic data based on ore minerals rather than hydrothermal and/or magmatic mineral phases. This  
577 observation is particularly important in the case of the Milluni – Kellhuani district and other tin deposits in  
578 neighboring areas of the Cordillera Real (Fig. 1A). In the Yani, Sorata, Zongo and Huayna Potosí plutons, there is  
579 a large dispersion of radiometric dates (mostly K/Ar and Ar/Ar silicate mineral dates; Fig. 7) from Late Triassic  
580 (i.e., the accepted age of host rock crystallization, constrained by U-Pb zircon dating) to dates as young as ca. 35  
581 Ma. This dispersion in radiometric dates probably represents protracted isotopic resetting during the complex  
582 thermal history undergone by these rocks (cf. Farrar et al. 1988; Kontak et al. 1990; Schildgen and Hoke 2018) but  
583 also opens the door to overprinting hydrothermal events connected to mineralization.

584 Our U-Pb cassiterite date for Kellhuani ( $218.3 \pm 5.5$  Ma) agrees, within the limits of the analytical error, with the  
585 K/Ar muscovite date at  $210 \pm 6$  Ma reported by McBride et al. (1983) for the greisen at the Chacaltaya porphyry  
586 stock, which is genetically connected to the mineralization in the Milluni-Kellhuani district (Lehmann 1985). In  
587 addition, this date agrees with the U-Pb zircon concordia dates of  $222.3 \pm 2.4$  and  $220.8 \pm 1.9$  Ma reported by  
588 Cordani et al. (2019) for two granite samples from the neighboring Huayna Potosí pluton.

589 In the Viloco deposit, our U-Pb cassiterite date ( $24.4 \pm 0.4$  Ma) agrees, within error, with felsic magmatism in the  
590 Tres Cruces batholith dated at ca. 22-26 Ma via K/Ar analysis of igneous biotite and muscovite (Ahlfeld and  
591 Branisa 1960; Cordani 1967 in Clark and Farrar 1973; Evernden et al. 1977; McBride et al. 1983; Gillis et al.  
592 2006). Gillis et al. (2006) performed U-Pb dating of zircons from the Quimsa Cruz batholith in the Argentina and  
593 Viloco mines and obtained dates of  $26.2 \pm 0.2$  and  $25.4 \pm 0.2$  Ma, respectively.

594 As far as we know, there are no geochronological studies in the Huanuni deposit area. The mineralization has been  
595 suggested to be of Late Oligocene - Early Miocene age by analogy with other neighboring mining districts (e.g.,  
596 San Pablo stock - Japo - Santa Fe, El Poder and Llallagua; Fig. 1A) for which igneous activity connected to tin  
597 mineralization has been dated in the range between ca. 25 and 20 Ma (K/Ar mineral and whole rock dates;  
598 Evernden et al. 1961; Grant et al. 1979; Sugaki et al. 2003). This age bracket encompasses our  $24.0 \pm 2.4$  Ma U-Pb  
599 cassiterite date in the Huanuni deposit. The nearby Mororocala ignimbrites (Fig. 1A), in contrast, are much  
600 younger according to Ar/Ar dates of ca. 8-6 Ma provided by Koeppen et al. (1987) (see also Morgan et al. 1998).

601 The age of the mineralization in the Llallagua deposit has long been a topic of discussion. Reported radiometric  
602 dating includes dates as disparate as  $43.8 \pm 4.7$  Ma (Sm/Nd early fluorapatite vein assemblages, [Rakovan et al.](#)  
603 [1997](#)),  $42.2 \pm 4$  Ma (Pb/Pb evaporation age in zircon; [Kempe et al. 2008](#)),  $23.4 \pm 2.2$  and  $19.0 \pm 1.6$  Ma (U-Pb  
604 monazite, [Kempe et al. 2008](#); [Kohn and Vervoort 2008](#)) and  $20.9 \pm 0.4$  Ma (K/Ar geochronology of the  
605 hydrothermally altered porphyry, [Grant et al. 1979](#)). U-Pb dating on cassiterite by [Neymark et al. \(2018\)](#) yielded a  
606 date of  $20.0 \pm 2.5$  Ma, which overlaps within error with our  $24.0 \pm 5.1$  Ma U/Pb cassiterite date thus constraining  
607 the tin mineralization event in this deposit to the Early Miocene.

608 The new geochronologic data presented here, hence, conform to the idea that tin mineralization events in the  
609 Bolivian tin belt occurred at least in two separate epochs during the Late Triassic (Norian; Milluni-Kellhuani  
610 district) and the Late Oligocene (Chattian) - Early Miocene (Aquitainian; Viloco, Huanuni and Llallagua deposits).  
611 Unpublished cassiterite U-Pb analyses in samples from the San Rafael deposit in Peru yield dates of ca. 24 Ma  
612 (pers. comm. M. Harlaux), similar to the Viloco, Huanuni and Llallagua deposits. These ages coincide with major  
613 episodes of mantle upwelling, decompression melting and basalt production, and related high heat flow into the  
614 overlying crust (see above). Unfortunately, U-Pb measurements of cassiterite grains from deposits located in the  
615 southernmost part of the Bolivian tin belt were inconclusive, although previous geochronological data would point  
616 to younger mineralization ages of ca. 15-13 Ma ([Fig. 7](#); see also [Slater et al. 2020](#) for a discussion on the age of the  
617 Pirquitas deposit in Argentina based on field relationships). Progressively younger tin-polymetallic mineralization  
618 towards the south of the Bolivian tin belt during the Pliocene and Miocene might be related to the southward  
619 passage of the subducting Juan Fernández aseismic ridge and associated migrating magmatic flare-up ([de Silva](#)  
620 [and Kay 2018](#)); the latter might however have resulted from the southward migration of the onset of Late  
621 Oligocene–earliest Miocene major mafic magmatism detected by [Fornari et al. \(2002\)](#), possibly as a consequence  
622 of the reconstructed migration of this ridge. Separate tectonic events leading to i) crustal melting of volatile-rich,  
623 carbonaceous sediments and ii) enhanced magmatic differentiation and sustained heat production enabled by long  
624 crustal residence of mantle-derived melts in a thickened crust converged to form one of the largest Sn  
625 accumulations on Earth ([Dietrich et al. 2000](#); [Lehmann et al. 2000](#)).

#### 626 **Controls on minor- and trace-element variations in cassiterite**

627 Due to the tetragonal structure of cassiterite and according to charge, radii and coordination of ions compared with  
628  $\text{Sn}^{4+}$  the following elements are considered to be compatible with cassiterite:  $\text{Al}^{3+}$ ,  $\text{Fe}^{3+}$ ,  $\text{Ga}^{3+}$ ,  $\text{V}^{3+}$ ,  $\text{Cr}^{3+}$ ,  $\text{Sc}^{3+}$ ,  $\text{Sb}^{3+}$ ,  
629  $\text{W}^{4+}$ ,  $\text{U}^{4+}$ ,  $\text{Zr}^{4+}$ ,  $\text{Hf}^{4+}$ ,  $\text{Ti}^{4+}$ ,  $\text{Nb}^{5+}$  and  $\text{Ta}^{5+}$  ([Cheng et al. 2019](#); [Mao et al. 2020](#)). Of these elements, the 4+ charged



630 cations (Zr, Hf, Ti, U and W) can directly substitute for  $\text{Sn}^{4+}$  (without readjustments of charge balance) while  
631 coupled substitution mechanisms are required for differently-charged cations (e.g., Fe, Mn, Nb, Ta and In; [Cheng  
632 et al. 2019](#)).

633 Zirconium and Hf have similar geochemical behavior, so they usually maintain a near chondritic Zr/Hf ratio of 35-  
634 40 ([Hoskin and Schaltegger 2003](#)). However, in hydrothermal environments and in highly differentiated igneous  
635 rocks, deviations from this ratio (i.e., element pair decoupling) can occur ([Bau 1996](#)). Processes such as  
636 metasomatism, crystal fractionation in the presence of zircon, hydrothermal alteration or preferential mobilization  
637 of Zr in B- and F-rich fluids have been proposed to cause fractionation of Zr over Hf ([Cheng et al. 2019](#)). The fact  
638 that the studied cassiterite samples yielded Zr/Hf up to 90 agrees with the high activity of B and F during the  
639 formation of the mineralization along the Bolivian tin belt, as seen in abundant tourmaline plus fluorite.

640 Even though Nb and Ta are considered to have similar geochemical behavior, large variations in their  
641 concentration and ratio occur in cassiterite. [Cheng et al. \(2019\)](#) attribute these variations to processes involving  
642 element fractionation during mineral growth due to fluid disequilibrium. However, variations in the concentration  
643 of Nb and Ta may also be related to the physical-chemical characteristics of the hydrothermal fluids ([Zhao et al.  
644 2019](#); [Lerouge et al. 2017](#)). [Zhang et al. \(2017\)](#) noted that cassiterite from high-temperature systems related to  
645 highly fractionated Li-F granites and pegmatites has high Nb, Ta and Zr contents (with low Zr/Hf ratios) but low  
646 Fe and Mn contents, contrary to cassiterite from low-temperature hydrothermal deposits. On the other hand,  
647 isomorphous replacement of  $\text{Sn}_3\text{O}_6$  by  $(\text{Fe},\text{Mn})(\text{Nb},\text{Ta})_2\text{O}_6$  is typical of cassiterite in hydrothermal cassiterite-  
648 quartz veins and greisen deposits (e.g., [Möller et al. 1988](#); [Murciego et al. 1997](#); [Abdalla et al. 2008](#)), whereas  
649 isomorphic replacement of  $3\text{Sn}^{4+}$  by  $2(\text{Nb},\text{Ta})^{5+} + (\text{Fe},\text{Mn})^{2+}$  is typical of magmatic cassiterite from rare-element  
650 granites and pegmatites (e.g., [Tindle and Breaks 1998](#)).

651 Cassiterite grains from the Bolivian tin belt are low in Nb+Ta relative to most cassiterite compiled from the  
652 literature, particularly to magmatic cassiterite ([Fig. 4A-C, Table 2](#)). Iron and Mn concentrations in cassiterite  
653 samples from the Bolivian tin belt fit the composition of most cassiterite described in the literature, with the  
654 exception of magmatic cassiterite and cassiterite in greisen mineralizations, which are significantly enriched in  
655 Mn. In terms of Fe+Mn and Nb+Ta, cassiterite from the Bolivian tin belt shows limited dispersion without any  
656 correlation between the concentrations of Fe+Mn and Nb+Ta ([Figs. 4A-B](#)); these observations suggest that neither  
657 of the aforementioned substitution mechanisms was significant in the composition of the studied grains. Regarding  
658 Nb and Ta systematics, the compositions of cassiterite samples from the Bolivian tin belt lie largely along the

659 Nb:Ta = 2:1 ratio line similar to most cassiterite in hydrothermal occurrences worldwide, whereas most magmatic  
660 cassiterite and cassiterite from greisen mineralizations lie rather along the 1:1 ratio line (Fig. 4C). Niobium and Ta  
661 are enriched in cassiterite grains from the sediment-hosted Kellhuani and Viloco xenothermal deposits, which  
662 formed adjacent to causative intrusive complexes, and the stock-hosted Llallagua xenothermal deposit (Fig. 1B)  
663 relative to epithermal and shallow xenothermal deposits formed at lower temperatures and depths (Figs. 1, 3).

664 A decrease in Ti and Ti/Zr in cassiterite grains has been linked to transition from proximal (higher temperature) to  
665 distal (lower temperature) locations in intrusion-centered hydrothermal systems (Taylor 1979; Cheng et al. 2019),  
666 which coincides with a higher solubility of Zr in hydrothermal fluids compared to Ti (see also Kessel et al. 2005).  
667 On the other hand, Sc is said to be transported as F complexes in post-magmatic fluids (Plimer et al. 1991). Our  
668 samples describe Ti/Zr variations by up to two orders of magnitude and systematically plot above the 1:1 ratio line  
669 in Fig. 4E similar to reference data for xenothermal and epithermal deposits. In general, cassiterite samples from  
670 the intrusion-proximal Kellhuani and Viloco deposits show higher Ti/Zr and Ti/Sc than samples from the  
671 intrusion-distal Ánimas - Chocaya - Siete Suyos and Poopó deposits (Figs. 1B, 4E,G). Accordingly, our dataset  
672 agrees with a progressive depletion of Ti relative to Zr and Sc in hydrothermal fluids as they evolved or migrated  
673 away from the causative intrusive bodies and hence the Ti/Zr and Ti/Sc ratios can be used as tracers to magmatic-  
674 hydrothermal centers.

675 Cassiterite samples from the Bolivian tin belt yield a fair positive correlation between V and Sc, which has been  
676 used to propose a  $\text{Sc}^{3+} + \text{V}^{5+} \Leftrightarrow 2\text{Sn}^{4+}$  coupled substitution in tin-granite-, greisen-, skarn- and vein-type ores by  
677 Cheng et al. (2019). The behavior in hydrothermal systems of elements such as V, In, Ge and Ga regarding  
678 cassiterite is poorly understood. Plimer et al. (1991) related the In composition of cassiterite directly to the  
679 concentration of this element in the hydrothermal ore-forming fluids. The highest average concentrations of In in  
680 cassiterite samples from the Bolivian tin belt are found indeed in Huari Huari and Ánimas - Chocaya - Siete Suyos  
681 districts, which are well known for their high concentrations of In (Schwarz-Schampera and Herzig 2002; Torró et  
682 al. 2019a,b; Pring et al. 2020; Tables 2 and 3) thus supporting this idea. Lerouge et al. (2019) found that sulfides  
683 (such as stannite and sphalerite) and rutile associated with In-poor cassiterite contain high amounts of In thus  
684 highlighting that In tends to preferentially partition in sulfides rather than cassiterite. This would be also the case  
685 in the deposits from the Bolivian tin belt (Jiménez-Franco et al. 2018; Cacho et al. 2019; Torres et al. 2019; Torró  
686 et al. 2019a,b).

687 The studied cassiterite samples from the Bolivian tin belt show average REE concentrations similar to those of  
688 reference data for cassiterite in granite, granite-cupola and greisen mineralizations (Table 1; Fig. 5). Similar to  
689 cassiterite from the Bolivian tin belt, cassiterite from granites and granite-cupolas also show positive anomalies in  
690 MREE in chondrite-normalized diagrams, particularly Tb (see Zoheir et al. 2019). It is noteworthy that, unlike  
691 cassiterite from the Bolivian tin belt, cassiterite compositions reported in the literature normally lack negative Ce  
692 anomalies. Broken, “unusual” REE patterns combining concave and convex tetrads are acknowledged in tin-  
693 bearing magmatic-hydrothermal systems probably connected to liquid-vapor REE fractionation (Monecke et al.  
694 2011). Following Monecke et al. (2011), the irregular REE tetrad partition in cassiterite samples from the Bolivian  
695 tin belt would reflect generalized fluid immiscibility during the early stages of evolution of the studied deposits  
696 concomitant with the crystallization of cassiterite. Kelly and Turneaure (1970) proposed that boiling of the early  
697 tin-bearing fluid was an important mechanism for the precipitation of early quartz and cassiterite in Llallagua, and  
698 may have played an important role in the location of high grade ore in some shallow deposits of central and  
699 southern Bolivia (as also suggested by Chace 1948a,b for the Oruro deposits). These authors suggest that the  
700 upward vertical zoning of high grade cassiterite to low grade sulfide-rich tin ore may mark levels of local boiling.  
701 Other plausible mechanisms that might have controlled REE fractionation during the crystallization of  
702 hydrothermal cassiterite in Bolivian deposits include i) mixing between magmatic and meteoric waters (as  
703 proposed for the San Rafael deposit; Kontak and Clark 2002, Harlaux et al. 2020) leading to destabilization of  
704 REE chloride and fluoride complexes, which are more stable with increasing atomic number (Migdisov et al.  
705 2016); and ii) partitioning of REE between co-crystallizing phases (e.g., monazite and tourmaline; Jolliff et al.  
706 1987; Harlaux et al. 2020; Sciuba et al. 2020). Nevertheless, these alternative or complimentary mechanisms  
707 leading to REE fractionation would not reproduce the broken, highly irregular chondrite-normalized REE patterns  
708 described here for cassiterite samples from the Bolivian tin belt and therefore we surmise that their impact, if any,  
709 was subordinate to that of fluid immiscibility.

#### 710 **Potential of cassiterite from the Bolivian tin belt as a source of critical elements as byproducts**

711 Previous studies on the concentration of high-tech metals in deposits from the Bolivian tin belt have focused  
712 mostly on the sulfide mineralization (Schwarz-Schampera and Herzig 2002; Ishihara et al. 2011; Artiaga et al.  
713 2013; Murakami and Ishihara 2013; Jiménez-Franco et al. 2018; Cacho et al. 2019; Torres et al. 2019; Torró et al.  
714 2019a,b; Pring et al. 2020; summary of reported maximum concentrations of In, Ge and Ga shown in Table 3). In

715 the following lines we assess the potential of cassiterite from the Bolivian tin belt as a source of high-tech, critical  
716 elements, chiefly Nb, Ta, In, Ge and Ga, by comparing our results with bibliographic values.

717 Cassiterite samples from the Bolivian tin belt yielded much lower Nb concentrations than cassiterite from granite-  
718 hosted, granite cupola, greisen and pegmatite mineralizations worldwide (Table 2). Cassiterite from xenothermal  
719 and epithermal mineralizations reported in the literature is also enriched in Nb relative to our values. Likewise,  
720 cassiterite from the Bolivian tin belt is strongly depleted in Ta relative to most cassiterite compositions reported in  
721 the literature (Table 2). According to our results, cassiterite from the Bolivian tin belt is not likely to make a good  
722 resource for these two metals.

723 Indium concentrations in cassiterite from the Bolivian tin belt are consistent with, and often higher than,  
724 previously reported concentrations worldwide. However, it is noteworthy that in most of the studied Bolivian  
725 deposits, sulfide minerals, namely sphalerite and stannite, are the main In hosts, often with concentrations at the  
726 wt% level (Table 3). On the other hand, there is a close correlation between In enrichment in cassiterite and sulfide  
727 minerals in deposits along the Bolivian tin belt (Table 3). Therefore, in some deposits, cassiterite might represent a  
728 potential, additional source of In. The metallurgical recovery of In from cassiterite is, as far as we know, poorly  
729 developed. Preconcentration of In in slag during the smelting process to obtain tin metal from cassiterite could be  
730 expected, just as for Nb and Ta (Gupta and Suri 1994), In being separated afterwards by a multistep operation  
731 involving sulfuric acid leach of ferrite slag (Tshijik Karumb 2016).

732 Gallium contents in cassiterite samples from the Bolivian tin belt are also consistent with and often higher than  
733 concentrations reported in the literature (Table 2). Germanium concentrations in the studied samples of cassiterite  
734 are systematically very low, particularly if compared to Ge concentrations reported for cassiterite from pegmatites.  
735 With data in hand, cassiterite from the Bolivian tin belt is probably unattractive as source of Ge.

## 736 **Conclusions**

737 Tin mineralization has been dated directly by U-Pb geochronology on cassiterite samples from the Kellhuani  
738 ( $218.3 \pm 5.5$  Ma), Viloco ( $24.4 \pm 0.4$  Ma), Huanuni ( $24.0 \pm 2.4$  Ma) and Llallagua ( $24.0 \pm 5.1$  Ma) deposits. The  
739 dates are in good agreement with published ages for igneous rocks within the respective districts and confirm that  
740 hydrothermal tin mineralization in the Bolivian tin belt occurred mostly in two periods: Late Triassic and Late  
741 Oligocene –Miocene.

742 Our new ages closely coincide with two major magmatic episodes that were apparently triggered by mantle  
743 upwelling, decompression melting and basalt production, and related high heat flow into the overlying crust. The  
744 age obtained for Kellhuani coincides with the culmination of the Mitu rifting episode (~240–220 Ma; [Spikings et](#)  
745 [al. 2016](#)). The dates obtained for Viloco, Huanuni and Llallagua have mean values at 24.0 Ma, which overlap with  
746 the timing of major and widespread basaltic magmatism in the central Altiplano and probably adjacent regions.

747 The convergence of highly evolved, peraluminous silicic melts derived in part from the melting of volatile-rich  
748 sedimentary series and a sustained heat and fluid contribution from primitive melts stored at intermediate and  
749 upper levels of a thickened continental crust enhanced the formation of large tin deposits along the Bolivian tin  
750 belt.

751 The composition of the studied cassiterite samples is relatively homogeneous at the metalliferous belt scale.  
752 Nevertheless, nuances in trace element contents in mineralizations emplaced at different levels within the  
753 xenothermal and epithermal environments allow for the identification of some compositional trends. Some  
754 deposits formed adjacent to causative intrusive complexes such as Kellhuani, Viloco and Llallagua are typically  
755 enriched in Nb and Ta relative to epithermal and shallow xenothermal deposits. In addition, Ti/Zr and Ti/Sc ratios  
756 decrease from intrusive-proximal to intrusive-distal locations and therefore can be used to vectorize toward  
757 magmatic-hydrothermal centers.

758 REE abundances are elevated in cassiterite from intrusive-proximal (e.g., Kellhuani, Llallagua) relative to  
759 intrusive-distal mineralizations. There is a general, pronounced enrichment in MREE relative to LREE and HREE  
760 in chondrite-normalized patterns. REE distribution patterns are likely influenced by boiling processes, which yield  
761 characteristic broken REE patterns combining concave and convex tetrads.

762 The hydrothermal cassiterite from the Bolivian tin belt has low Nb and Ta compared with magmatic cassiterite in  
763 rare-metal granites and pegmatites. The concentration of Ge is systematically very low in the studied cassiterite  
764 samples. However, some cassiterite samples have relatively high concentrations of In and Ga. Interestingly, the  
765 highest In concentrations in cassiterite from the Bolivian tin belt are found in samples from deposits with  
766 documented high concentration of this element in sulfide minerals, suggesting that the concentration of In in  
767 cassiterite is primarily controlled by its availability in the hydrothermal fluid. In these particular deposits,  
768 cassiterite could represent an additional economic source of In.

## 769 **Acknowledgments**

770 This study was economically supported by the Peruvian CONCYTEC-FONDECYT-World Bank project 107-  
771 2018-FONDECYT-BM-IADT-AV and the Catalan project 2017-SGR-00707. We gratefully acknowledge Pura  
772 Alfonso (Polytechnic University of Catalonia) for providing cassiterite samples from the Llallagua deposit. The  
773 Bolivian State Mining Company (Corporación Minera de Bolivia—COMIBOL) granted its permission to the  
774 authors to access the Huanuni mine and to perform the necessary sampling; J.C. Ayaviri, J. Araca, R. Condori, N.  
775 Guevara and all individuals at COMIBOL are cordially thanked for their kind and efficient help during field work.  
776 The help and hospitality extended by the miners from mining cooperatives during sampling and field work are  
777 most gratefully acknowledged. We appreciate the technical support by Xavier Llovet (CCiT-UB) during the  
778 acquisition of EPMA data, and by Peter Tollan (ETH) during the acquisition of LA-ICP-MS data. We are grateful  
779 to Daniel Kontak, Matthieu Harlaux, and Editor-in-Chief Bernd Lehmann for their constructive comments which  
780 significantly improved the manuscript.

## 781 **References**

- 782 Abdalla HM, Matsueda H, Obeid MA, Takahashi R (2008) Chemistry of cassiterite in rare metal granitoids and  
783 the associated rocks in the Eastern Desert, Egypt. *J Miner Petrol Sci* 103:318-326.  
784 <https://doi.org/10.2465/jmps.070528a>
- 785 Ahlfeld F (1967) Metallogenic epochs and provinces of Bolivia. *Miner Deposita* 2:291–311.  
786 <https://doi.org/10.1007/BF00207022>
- 787 Ahlfeld F, Branisa L (1960) *Geología de Bolivia*. Don Bosco, Texas
- 788 Ahlfeld F, Schneider-Scherbina A (1964) Los yacimientos minerales y de hidrocarburos de Bolivia. *Bolivia*  
789 *Departamento Nacional de Geología* 5:1–388
- 790 Arce-Burgoa O (2009) *Metalliferous Ore Deposits of Bolivia*. SPC Impresores: La Paz
- 791 Arce-Burgoa O, Goldfarb RJ (2009) Metallogeny of Bolivia. *SEG Newsletter* 79:1–15
- 792 Artiaga D, Torres B, Torró L, Tauler E, Melgarejo JC, Arce-Burgoa O (2013) The Viloco Sn-W-Mo-As deposits,  
793 Bolivia: geology and mineralogy. Conference: 12th SGA Biennial Meeting “Mineral deposit research for a  
794 high-tech world”, 3:1239–1242, Uppsala
- 795 Baldellón E, Fornari M, Espinoza F, Soler P (1994) Sucesión estructural de la zona Serranía de las Minas. XI  
796 *Congreso Geológico de Bolivia, Memorias*, pp. 238–247
- 797 Bau M (1996) Controls on the fractionation of isovalent trace elements in magmatic and aqueous systems:  
798 evidence from Y/Ho, Zr/Hf, and lanthanide tetrad effect. *Contrib Mineral Petrol* 123:323-333.  
799 <https://doi.org/10.1007/s004100050159>

800 Betkowski WB, Rakovan J, Harlov DE (2017) Geochemical and textural characterization of phosphate accessory  
801 phases in the vein assemblage and metasomatically altered Llallagua tin porphyry. *Miner Petrol* 111:547–  
802 568. <https://doi.org/10.1007/s00710-017-0510-6>

803 Briskey JA (2005) Indium in lead–zinc and other mineral deposits. Open File Rpt 2005-1209.  
804 <http://pubs.usgs.gov/of/2005/1209/2005-1209.pdf>. Accessed 10 June 2020

805 Buddington AF (1935) High-temperature mineral associations at shallow to moderate depths. *Econ Geol* 30:205–  
806 222. <https://doi.org/10.2113/gsecongeo.30.3.205>

807 Cacho A, Melgarejo JC, Camprubi A, Torró L, Castillo-Oliver M, Torres B, Artiaga D, Tauler E, Martínez Á,  
808 Campeny M, Alfonso P, Arce-Burgoa OR (2019) Mineralogy and distribution of critical elements in the  
809 Sn–W–Pb–Ag–Zn Huanuni deposit, Bolivia. *Minerals* 9:753. <https://doi.org/10.3390/min9120753>

810 Chace FM (1948a) Tin-silver veins of Oruro, Bolivia, Part I. *Econ Geol* 43:333–383.  
811 <https://doi.org/10.2113/gsecongeo.43.5.333>

812 Chace FM (1948b) Tin-silver veins of Oruro Bolivia; Part II. *Econ Geol* 43:435–470.  
813 <https://doi.org/10.2113/gsecongeo.43.6.435>

814 Cheilletz A, Clark AH, Farrar E, Arroyo Pauca G, MacArthur JD, Pichavant M (1990) Stratigraphy and  
815 geochronology of the Macusani ignimbrite field: chronometer of the Mio-Pliocene geodynamic evolution  
816 of the Andes of SE Peru. In: Symposium international "Géodynamique andine": résumés des  
817 communications. Paris: ORSTOM, 341–344

818 Chen LL, Ni P, Dai BZ, Li WS, Chi Z, Pan JY (2019) The genetic association between quartz vein- and greisen-  
819 type mineralization at the Maoping W–Sn deposit, Southern Jiangxi, China: Insights from zircon and  
820 cassiterite U–Pb Ages and cassiterite trace element composition. *Minerals* 9:411.  
821 <https://doi.org/10.3390/min9070411>

822 Cheng Y, Spandler C, Kemp A, Mao J, Rusk B, Hu Y, Blake K (2019) Controls on cassiterite (SnO<sub>2</sub>)  
823 crystallization: Evidence from cathodoluminescence, trace-element chemistry, and geochronology at the  
824 Gejiu Tin District. *Am Mineral* 104:118–129. <https://doi.org/10.2138/am-2019-6466>

825 Clark AH, Farrar E (1973) The Bolivian Tin Province; notes on the available geochronological data. *Econ Geol*  
826 68:102–106. <https://doi.org/10.2113/gsecongeo.68.1.102>

827 Clark AH, Farrar E, Caelles JC, Haynes SJ, Lortie RB, McBride SL, Quirt GS, Robertson RCR, Zentilli M (1976)  
828 Longitudinal variations in the metallogenetic evolution of the central Andes: A progress report. *Geol S Am*  
829 S 14:23–58

830 Clark AH, Palma VV, Archibald DA, Farrar E, Robertson RCR (1983) Occurrence and age of tin mineralization in  
831 the Cordillera Oriental, southern Peru. *Econ Geol* 78:514–520. <https://doi.org/10.2113/gsecongeo.78.3.514>

832 Clark AH, Farrar E, Kontak DJ, Langridge RJ, Arenas FMJ, France LJ, McBride SL, Woodman PL, Wasteneys  
833 HA, Sandeman HA, Archibald DA (1990) Geologic and geochronologic constraints on the metallogenic  
834 evolution of the Andes of southeastern Peru. *Econ Geol* 85:1520–1583.  
835 <https://doi.org/10.2113/gsecongeo.85.7.1520>



836 Clark AH, Chen Y, Grant JW, Kontak DJ, Wasteneys HA, Sandeman HA, Farrar E, Archibald DE (2000) Delayed  
837 inception of ore deposition in major lithophile-metal vein systems: The San Rafael tin and Pasto Bueno  
838 tungsten deposits, Peru. *Geol S Am S* 32, pp. 279

839 Claire H, Olivera L, Heuschmidt B, Arduz M, Troëng B, Ballón R (1996) Mapas temáticos de recursos minerales  
840 de Bolivia, Hoja Uncía: *Bol Ser Geol Bolivia* 7:184

841 Cordani UG, Iriarte AR, Sato K (2019) Geochronological systematics of the Huayna Potosí, Zongo and Taquesi  
842 plutons, Cordillera Real of Bolivia, by the K/Ar, Rb/Sr and U/Pb methods. *Braz J Geol* 49:1-22.  
843 <https://doi.org/10.1590/2317-4889201920190016>

844 Cunningham CG, Zartman RE, McKee EH, Rye RO, Naeser CW, Sanjinés V, Erickson GE, Tavera V (1996) The  
845 age and thermal history of Cerro Rico de Potosi, Bolivia. *Miner Deposita* 31:374-385.  
846 <https://doi.org/10.1007/BF00189185>

847 DeCelles PG, Horton BK (2003) Early to middle Tertiary foreland basin development and the history of Andean  
848 crustal shortening in Bolivia. *Geol Soc Am Bull* 115:58-77. [https://doi.org/10.1130/0016-  
849 7606\(2003\)115%3C0058:ETMTFB%3E2.0.CO;2](https://doi.org/10.1130/0016-7606(2003)115%3C0058:ETMTFB%3E2.0.CO;2)

850 Demouy S, Paquette J-L, Saint-Blanquat M de, Benoit M, Belousova EA, O'Reilly SY, García F, Tejada LC,  
851 Gallegos R, Sempere T (2012) Spatial and temporal evolution of Liassic to Paleocene arc activity in  
852 southern Peru unraveled by zircon U-Pb and Hf in-situ data on plutonic rocks. *Lithos* 155:183–200.  
853 <https://doi.org/10.1016/j.lithos.2012.09.001>

854 de Silva SL, Kay MS (2018) Turning up the heat: High-flux magmatism in the Central Andes. *Elements* 14:245–  
855 250. <https://doi.org/10.2138/gselements.14.4.245>

856 Díaz E (1997) Facies y ambientes sedimentarios de la Formación Cancañiri (Silúrico inferior) en La Cumbre de La  
857 Paz, norte de la Cordillera Oriental de Bolivia. *Geogaceta* 22:55-57

858 Dietrich A, Lehmann B, Wallianos A (2000) Bulk rock and melt inclusion geochemistry of Bolivian tin porphyry  
859 systems. *Econ Geol* 95:313-326. <https://doi.org/10.2113/gsecongeo.95.2.313>

860 European Commission (2017) Critical Raw Materials. [https://ec.europa.eu/growth/sectors/raw-materials/specific-  
861 interest/critical\\_en](https://ec.europa.eu/growth/sectors/raw-materials/specific-interest/critical_en). Accessed 14 April 2020

862 Everden JF (1961) Edades absolutas de algunas rocas ígneas en Bolivia por el método potasio-argón. *Soc Geol Bol*  
863 Not 2:3

864 Evernden JF, Kriz SJ, Cherroni CM (1977) Potassium-argon ages of some Bolivian rocks. *Econ Geol* 72:1042–  
865 1061. <https://doi.org/10.2113/gsecongeo.72.6.1042>

866 Farrar E, Clark AH, Kontak DJ, Archibald DA (1988) Zongo-San Gabán zone: Eocene foreland boundary of the  
867 Central Andean orogen, northwest Bolivia and southeast Peru. *Geology* 16:55–58.  
868 [https://doi.org/10.1130/0091-7613\(1988\)016%3C0055:ZSGNZE%3E2.3.CO;2](https://doi.org/10.1130/0091-7613(1988)016%3C0055:ZSGNZE%3E2.3.CO;2)

869 Farrar E, Clark AH, Heinrich SM (1990) The age of the Zongo pluton and the tectonothermal evolution of the  
870 Zongo-San Gabán Zone in the Cordillera Real, Bolivia. Extended abstracts, 1st International Symposium  
871 on Andean Geodynamics, Grenoble, pp. 171–174



- 872 Fontboté L (2018) Ore deposits of the Central Andes. *Elements* 14:257–261.  
873 <https://doi.org/10.2138/gselements.14.4.257>
- 874 Fornari M, Baldellón E, Espinoza F, Ibarra I, Jiménez N, Mamani M (2002) Ar-Ar dating of Late Oligocene-Early  
875 Miocene volcanism in the Altiplano. Extended abstracts, 4th International Symposium on Andean  
876 Geodynamics, Toulouse, pp. 223–226
- 877 Fuchsloch W, Nex P, Kinnaird J (2019) The geochemical evolution of Nb-Ta-Sn oxides from pegmatites of the  
878 Cape Cross–Uis pegmatite belt, Namibia. *Mineral Mag* 83:1–56. <https://doi.org/10.1180/mgm.2018.151>
- 879 Gillis RJ, Horton BK, Grove M (2006) Thermochronology, geochronology, and upper crustal structure of the  
880 Cordillera Real: implications for Cenozoic exhumation of the central Andean plateau. *Tectonics* 25:1–22.  
881 <https://doi.org/10.1029/2005TC001887>
- 882 Goldschmidt V (1913) *Atlas der Kristallformen*. Heidelberg
- 883 Gordon SG (1944) The mineralogy of the tin mines of Cerro de Llallagua, Bolivia. *Proc Acad Nat Sci Philadelphia*  
884 96:279–359
- 885 Gorelikova NV, Khanchuk AI, Bortnikov NS, Pawlowsky-Glahn V, Tolosana-Delgado R (2004) Classification of  
886 tin deposits using trace elements in cassiterites (Far East, Russia) In Proceedings of the Interim Iagod  
887 Conference Vladivostok, Russia. *Dal'nauka*, 590–593
- 888 Gorelikova NV, Tolosana-Delgado R, Pawlowsky-Glahn V, Khanchuk A, Gonevchuk V (2006) Discriminating  
889 geodynamical regimes of tin ore formation using trace element composition of cassiterite: The Sikhote'Alin  
890 case (Far Eastern Russia). *Geol Soc Lon Spec Publ* 264:43–57.  
891 <https://doi.org/10.1144/GSL.SP.2006.264.01.04>
- 892 Grant JN, Halls C, Salinas WA, Snelling NJ (1979) K-Ar ages of igneous rocks and mineralization in part of the  
893 Bolivian tin belt. *Econ Geol* 74:838–851. <https://doi.org/10.2113/gsecongeo.74.4.838>
- 894 Guillong M, Hametner K, Reusser E, Wilson SA, Günther D (2005) Preliminary characterisation of new glass  
895 reference materials (GSA- 1G, GSC- 1G, GSD- 1G and GSE- 1G) by Laser Ablation- Inductively  
896 Coupled Plasma- Mass Spectrometry using 193 nm, 213 nm and 266 nm wavelengths. *Geostand Geoanal*  
897 *Res* 29:315–331. <https://doi.org/10.1111/j.1751-908x.2005.tb00903.x>
- 898 Guillong M, Meier DL, Allan MM, Heinrich CA, Yardley BWD (2008) SILLS: A MATLAB-based program for  
899 the reduction of laser ablation ICP-MS data of homogeneous materials and inclusions. In: Sylvester P, (ed)  
900 Laser Ablation ICP-MS in the Earth Sciences: Current Practices and Outstanding Issues. *Miner Assoc Can.*  
901 Short Course 40
- 902 Guillong M, Wotzlaw JF, Looser N, Laurent O (2020) Evaluating the reliability of U–Pb laser ablation inductively  
903 coupled plasma mass spectrometry (LA-ICP-MS) carbonate geochronology: matrix issues and a potential  
904 calcite validation reference material. *Geochronology* 2:155–167. <https://doi.org/10.5194/gchron-2-155-2020>
- 905 Guo J, Zhang RQ, Sun WD, Ling MX, Hu YB, Wu K, Zhang LC (2018) Genesis of tin-dominant polymetallic  
906 deposits in the Dachang district, South China: insights from cassiterite U-Pb ages and trace element  
907 compositions. *Ore Geol Rev* 95:863–879. <https://doi.org/10.1016/j.oregeorev.2018.03.023>

908 Gupta CK, Suri AK (1994) Extractive metallurgy of niobium. CRC press inc., Florida

909 Harlaux M, Kouzmanov K, Gialli S, Laurent O, Rielli A, Dini A, Chauvet A, Menzies A, Kalinaj M, Fontboté L  
910 (2020) Tourmaline as a Tracer of Late-Magmatic to Hydrothermal Fluid Evolution: The World-Class San  
911 Rafael Tin (-Copper) Deposit, Peru. *Econ Geol*, in press. <https://doi.org/10.5382/econgeo.4762>

912 Hellstrom JC, Paton C, Woodhead JD, Hergt JM (2008) Iolite: Software for spatially resolved LA-(quad and MC)  
913 ICP-MS analysis. In: Sylvester P (ed) *Laser ablation ICP-MS in the Earth sciences: Current practices and*  
914 *outstanding issues*. *Miner Assoc Can* 40:343–348

915 Heuschmidt B, La Torre JB, Angels VM, Zapata MC (2002) Las áreas prospectivas de Bolivia para yacimientos  
916 metalíferos. *Boletín del Servicio Nacional de Geología y Minería*, 30, La Paz

917 Horton BK, Hampton BA, Waanders GL (2001) Paleogene synorogenic sedimentation in the Altiplano plateau and  
918 implications for initial mountain building in the central Andes. *Geol Soc Am Bull* 113:1387–1400.  
919 [https://doi.org/10.1130/0016-7606\(2001\)113%3C1387:PSSITA%3E2.0.CO;2](https://doi.org/10.1130/0016-7606(2001)113%3C1387:PSSITA%3E2.0.CO;2)

920 Hoskin PWO, Schaltegger U (2003) The composition of zircon and igneous and metamorphic petrogenesis. *Rev*  
921 *Mineral Geochem* 53: 27–62. <https://doi.org/10.2113/0530027>

922 Hulsbosch N, Muchez P (2019) Tracing fluid saturation during pegmatite differentiation by studying the fluid  
923 inclusion evolution and multiphase cassiterite mineralisation of the Gatumba pegmatite dyke system (NW  
924 Rwanda). *Lithos* 354-355, Article 105285. <https://doi.org/10.1016/j.lithos.2019.105285>

925 Husson L, Sempere T (2003) Thickening the Altiplano crust by gravity-driven crustal channel flow. *Geophys Res*  
926 *Lett* 30:1243-1246. <https://doi.org/10.1029/2002GL016877>

927 Imai H, Lee MS, Iida K, Fujiki Y, Takenouchi S (1975) Geologic structure and mineralization of xenothermal  
928 vein-type deposits in Japan. *Econ Geol* 70:647–676. <https://doi.org/10.2113/gsecongeo.70.4.647>

929 Isacks BL (1988) Uplift of the central Andean plateau and bending of the Bolivian orocline. *J Geophys Res*  
930 93:3211–3231. <https://doi.org/10.1029/JB093iB04p03211>

931 Ishihara S (1981) The granitoid series and mineralization. *Econ Geol Anniversary Vol* 75:458-484.  
932 <https://doi.org/10.5382/AV75.14>

933 Ishihara S, Murakami H, Márquez-Zavalía MF (2011) Inferred indium resources of the Bolivian tin-polymetallic  
934 deposits. *Resour Geol* 61:174-191. <https://doi.org/10.1111/j.1751-3928.2011.00157.x>

935 James DE (1971a) Andean crustal and upper mantle structure. *J Geophys Res* 76:3246–3271.  
936 <https://doi.org/10.1029/JB076i014p03246>

937 James DE (1971b) Plate tectonic model for the evolution of the Central Andes. *Geol Soc Am Bull* 82:3325–3346.  
938 [https://doi.org/10.1130/0016-7606\(1971\)82\[3325:PTMFTE\]2.0.CO;2](https://doi.org/10.1130/0016-7606(1971)82[3325:PTMFTE]2.0.CO;2)

939 Jiang SY, Yu JM, Lu JJ (2004) Trace and rare-earth element geochemistry in tourmaline and cassiterite from the  
940 Yunlong tin deposit, Yunnan, China: Implication for migmatitic-hydrothermal fluid evolution and ore  
941 genesis. *Chem Geol* 209:193–213. <https://doi.org/10.1016/j.chemgeo.2004.04.021>

942 Jiménez-Franco A, Alfonso P, Canet C, Trujillo JE (2018) Mineral chemistry of In-bearing minerals in the Santa  
943 Fe mining district, Bolivia. *Andean Geol* 45:410–432. <https://doi.org/10.5027/andgeoV45n3-3052>

944 Jochum KP, Wies U, Stoll B, Kuzmin D, Yang Q, Raczek I, Jacob DE, Stracke A, Birbaum K, Frick DA, Günter  
945 D, Enzweiler J (2011) Determination of reference values for NIST SRM 610-617 glasses following ISO  
946 guidelines. *Geostand Geoanal Res* 35:397–429. <https://doi.org/10.1111/j.1751-908X.2011.00120.x>

947 Jolliff BL, Papike JJ, Laul JC (1987) Mineral recorders of pegmatite internal evolution: REE contents of  
948 tourmaline from the Bob Ingersoll pegmatite, South Dakota. *Geochim Cosmochim Acta* 51:2225-2232.  
949 [https://doi.org/10.1016/0016-7037\(87\)90272-9](https://doi.org/10.1016/0016-7037(87)90272-9)

950 Kelly WC, Turneure FS (1970) Mineralogy, paragenesis and geothermometry of the tin and tungsten deposits of  
951 the Eastern Andes, Bolivia. *Econ Geol* 65:609–680. <https://doi.org/10.2113/gsecongeo.65.6.609>

952 Kendall-Langley L, Kemp A, Grigson J, Hammerli J (2019) U-Pb and reconnaissance Lu-Hf isotope analysis of  
953 cassiterite and columbite group minerals from Archean Li-Cs-Ta type pegmatites of Western Australia.  
954 *Lithos* 352-353. Article 105231. <https://doi.org/10.1016/j.lithos.2019.105231>

955 Kessel R, Ulmer P, Pettke T, Schmidt MW, Thompson AB (2005) The water-basalt system at 4 to 6 GPa: Phase  
956 relations and second critical endpoint in a K-free eclogite at 700 to 1400 °C. *Earth Planet Sci Lett* 237:873–  
957 892. <https://doi.org/10.1016/j.epsl.2005.06.018>

958 Keutsch F, De Brodtkorb MK (2008) Metalliferous paragenesis of the San José mine, Oruro, Bolivia. *J S Am*  
959 *Earth Sci* 25:485-491. <https://doi.org/10.1016/j.jsames.2007.12.003>

960 Koeppen RP, Smith RL, Kunk MJ, Flores AM, Luedke RG, Sutter JF (1987) The Morococala volcanics: Highly  
961 peraluminous rhyolite ash flow magmatism in the Cordillera Oriental, Bolivia. *Geol S Am S* 19:731

962 Kohn MJ, Vervoort JD (2008) U-Th-Pb dating of monazite by single collector ICP-MS: pitfalls and potential.  
963 *Geochem Geophys Geosyst* 9:1–16. <https://doi.org/10.1029/2007GC001899>

964 Kono M, Fukao Y, Yamamoto A (1989) Mountain building in the Central Andes. *J Geophys Res* 94:3891–3905.  
965 <https://doi.org/10.1029/JB094iB04p03891>

966 Kontak DJ, Clark AH (2002) Genesis of the giant, bonanza San Rafael lode tin deposit, Peru: Origin and  
967 significance of pervasive alteration. *Econ Geol* 97:1741–1777. <https://doi.org/10.2113/gsecongeo.97.8.1741>

968 Kontak DJ, Clark AH, Farrar E, Strong DF (1984) The rift-associated Permo-Triassic magmatism of the Eastern  
969 Cordillera: A precursor to the Andean orogeny. In Pitcher WS, Atherton MP, Cobbing EJ, Beckinsale RD  
970 (eds) *Magmatism at a plate edge: The Peruvian Andes*. Blackie, Glasgow-London

971 Kontak DJ, Clark AH, Pearce TH, Strong DF, Baadsgaard H (1986) Petrogenesis of a Neogene shoshonite suite,  
972 Cerro Moromoroni, Puno, southeastern Peru. *Can Mineral* 24:117-135

973 Kontak DJ, Clark AH, Farrar E, Archibald DA, Baadsgaard H (1987) Geochronological data for Tertiary granites  
974 of the southeast Peru segment of the central Andean tin belt. *Econ Geol* 82:1711-1618.  
975 <https://doi.org/10.2113/gsecongeo.82.6.1611>

- 976 Kontak DJ, Farrar E, Clark AH, Archibald DA (1990) Eocene tectono-thermal rejuvenation of an upper Paleozoic-  
977 lower Mesozoic terrane in the Cordillera de Carabaya, Puno, southeastern Peru, revealed by K-Ar and  
978 <sup>40</sup>Ar/<sup>39</sup>Ar dating. *J S Am Earth Sci* 3:231–246. [https://doi.org/10.1016/0895-9811\(90\)90005-L](https://doi.org/10.1016/0895-9811(90)90005-L)
- 979 Lamb S, Hoke L (1997) Origin of the high plateau in the Central Andes, Bolivia, South America. *Tectonics*  
980 16:623–649. <https://doi.org/10.1029/97TC00495>
- 981 Lancelot JR, Laubacher G, Marocco R, Renaud U (1978) U/Pb radiochronology of two granitic plutons from the  
982 Eastern Cordillera (Peru): Extent of Permian magmatic activity and consequence *Geol Rundsch* 67:286-  
983 248. <https://doi.org/10.1007/BF01803263>
- 984 Legros H, Harlaux M, Mercadier J, Romer RL, Poujol M, Camacho A, Marignac C, Cuney M, Wang RC, Charles  
985 N, Lespinasse MY (2020) The world-class Nanling metallogenic belt (Jiangxi, China): W and Sn  
986 deposition at 160 Ma followed by 30 m.y. of hydrothermal metal redistribution. *Ore Geol Rev* 117. Article  
987 103302. <https://doi.org/10.1016/j.oregeorev.2019.103302>
- 988 Lehmann B (1985) Formation of the strata-bound Kellhuani tin deposits, Bolivia. *Miner Deposita* 20:169–176.  
989 <https://doi.org/10.1007/BF00204561>
- 990 Lehmann B, Ishihara S, Michel H, Miller J, Rapela C, Sanchez A, Tistl M, Winkelmann L (1990) The Bolivian tin  
991 province and regional tin distribution in the Central Andes: A reassessment. *Econ Geol* 85:1044–1058.  
992 <https://doi.org/10.2113/gsecongeo.85.5.1044>
- 993 Lehmann B, Dietrich A, Heinhorst J, Métrich N, Mosbah M, Palacios C, Schneider HJ, Wallianos A, Webster J,  
994 Winkelmann L (2000) Boron in the Bolivian tin belt. *Miner Deposita* 35:223-232.  
995 <https://doi.org/10.1007/s001260050017>
- 996 Lehmann B, Zoheir B, Neymark L, Zeh A, Emam A, Radwan A, Zhang R, Moscati R (2020) Monazite and  
997 cassiterite U-Pb dating of the Abu Dabbab rare-metal granite, Egypt: Late Cryogenian metalliferous granite  
998 magmatism in the Arabian-Nubian Shield, *Gondwana Res* 84:71-80.  
999 <https://doi.org/10.1016/j.gr.2020.03.001>
- 1000 Lentz D, McAllister A (1990) The petrogenesis of tin- and sulfide-iodine mineralization at True Hill, southwestern  
1001 New Brunswick. *Atl Geol* 26:136-155. <https://doi.org/10.4138/1698>
- 1002 Lerouge C, Gloaguen E, Wille G, Bailly L (2017) Distribution of In and other rare metals in cassiterite and  
1003 associated minerals in Sn±W ore deposits of the western Variscan Belt. *Eur J Mineral* 29:739-753.  
1004 <https://doi.org/10.1127/ejm/2017/0029-2673>
- 1005 Maffione M, Speranza F, Faccenna C (2009) Bending and growth of the Central Andean plateau: Paleomagnetic  
1006 and structural constraints from the Eastern Cordillera (22–24°S, NW Argentina). *Tectonics* 28.  
1007 <https://doi.org/10.1029/2008TC002402>
- 1008 Mao W, Zhong H, Yang J, Tang Y, Liu L, Fu Y, Zhang X, Sein K, Soe MA, Li J, Zhang Le (2020) Combined  
1009 zircon, molybdenite, and cassiterite geochronology and cassiterite geochemistry of the Kuntabin tin-  
1010 tungsten deposit in Myanmar. *Econ Geol* 115:603–625. <https://doi.org/10.5382/econgeo.4713>

- 1011 Martinez C, Vargas E (1990) Sobre las deformaciones sinsedimentarias mesozoicas de la región de Macha-  
1012 Pocoata-Colquechaca (Norte de Potosí – Cordillera Oriental de Bolivia). YPFB 11:13-20
- 1013 McBride SL, Robertson RCR, Clark AH, Farrar E (1983) Magmatic and metallogenic episodes in the northern  
1014 tin belt, Cordillera Real, Bolivia. *Geol Rundsch* 72:685-71. <https://doi.org/10.1007/BF01822089>
- 1015 Migdisov A, Williams-Jones AE, Brugger J, Caporuscio FA (2016) Hydrothermal transport, deposition, and  
1016 fractionation of the REE: Experimental data and thermodynamic calculations. *Chem Geol* 439:13-42.  
1017 <https://doi.org/10.1016/j.chemgeo.2016.06.005>
- 1018 Mišković A, Spikings RA, Chew DM, Kosler J, Ulianov A, Schaltegger U (2009) Tectonomagmatic evolution of  
1019 Western Amazonia: Geochemical characterization and zircon U-Pb geochronologic constraints from the  
1020 Peruvian Eastern Cordilleran granitoids. *Geol Soc Am Bull* 121:1298–1324.  
1021 <https://doi.org/10.1130/B26488.1>
- 1022 Mlynarczyk MSJ, Williams-Jones AE (2005) The role of collisional tectonics in the metallogeny of the Central  
1023 Andean tin belt. *Earth Planet Sc Lett* 240:656- 667. <https://doi.org/10.1016/j.epsl.2005.09.047>
- 1024 Möller P, Dulski P, Szacki W, Malow G, Riedel E (1988) Substitution of tin in cassiterite by tantalum, niobium,  
1025 tungsten, iron and manganese. *Geochim Cosmochim Ac* 52:1497-1503. [https://doi.org/10.1016/0016-7037\(88\)90220-7](https://doi.org/10.1016/0016-7037(88)90220-7)
- 1026
- 1027 Monecke T, Kempe U, Trinkler M, Thomas R, Dulski P, Wagner T (2011) Unusual rare earth element  
1028 fractionation in a tin-bearing magmatic-hydrothermal system. *Geology* 39:295–298.  
1029 <https://doi.org/10.1130/G31659.1>
- 1030 Moore F, Howie RA (1979) Geochemistry of some Cornubian cassiterites. *Miner Deposita* 14:103-7.  
1031 <https://doi.org/10.1007/BF00201869>
- 1032 Morgan GB, London D, Luedke RG (1998) Petrochemistry of Late Miocene peraluminous silicic volcanic rocks  
1033 from the Morococala Field, Bolivia. *J Petrol* 39:601-632 <https://doi.org/10.1093/petroj/39.4.601>
- 1034 Moscati R, Neymark L (2019) U–Pb geochronology of tin deposits associated with the Cornubian Batholith of  
1035 southwest England: Direct dating of cassiterite by in situ LA-ICPMS. *Miner Deposita* 55:1-20.  
1036 <https://doi.org/10.1007/s00126-019-00870-y>
- 1037 Müller B, Frischknecht R, Seward T, Heinrich C, Camargo Gallegos W (2001) A fluid inclusion reconnaissance  
1038 study of the Huanuni tin deposit (Bolivia), using LA-ICP-MS micro-analysis. *Miner Deposita* 36:680–688.  
1039 <https://doi.org/10.1007/s001260100195>
- 1040 Murakami H, Ishihara S (2013) Trace elements of Indium-bearing sphalerite from tin- polymetallic deposits in  
1041 Bolivia, China and Japan: A femto-second LA-ICPMS study. *Ore Geol Rev* 53:223-243.  
1042 <https://doi.org/10.1016/j.oregeorev.2013.01.010>
- 1043 Murciego A, Sanchez AG, Dusausoy Y, Pozas JM, Ruck R (1997) Geochemistry and EPR of cassiterites from the  
1044 Iberian Hercynian Massif. *Mineral Mag* 61:357-365. <https://doi.org/10.1180/minmag.1997.061.406.03>

- 1045 Murray BP, Horton BK, Matos R, Heizler MT (2010) Oligocene-Miocene basin evolution in the northern  
1046 Altiplano, Bolivia: Implications for evolution of the central Andean backthrust belt and high plateau. *Geol*  
1047 *Soc Am Bull* 122:1443–1462. <https://doi.org/10.1130/B30129.1>
- 1048 Nascimento T, Souza V (2017) Mineralogy, stable isotopes ( $\delta^{18}\text{O}$  and  $\delta^{34}\text{S}$ ) and  $^{40}\text{Ar}$ - $^{39}\text{Ar}$  geochronology studies  
1049 on the hydrothermal carapace of the Igarapé Manteiga W-Sn deposit, Rondônia. *Braz J Geol* 47:591–613.  
1050 <https://doi.org/10.1590/2317-4889201720170068>
- 1051 Neiva A (2008) Geochemistry of cassiterite and wolframite from tin and tungsten quartz veins in Portugal. *Ore*  
1052 *Geol Rev* 33:221–238. <https://doi.org/10.1016/j.oregeorev.2006.05.013>
- 1053 Nespolo M, Souvignier B (2015) Structural rationale for the occurrence of the elbow twins in cassiterite and rutile.  
1054 *J Miner Petrol Sci* 110:157–165. <https://doi.org/10.2465/jmps.150123>
- 1055 Neymark L, Holm-Denoma C, Moscati R (2018) In situ LA-ICPMS U–Pb dating of cassiterite without a known-  
1056 age matrix-matched reference material: Examples from worldwide tin deposits spanning the Proterozoic to  
1057 the Tertiary. *Chem Geol* 483:410–425. <https://doi.org/10.1016/j.chemgeo.2018.03.008>
- 1058 Nupen S (2019) Mineral resource estimates for the Falchani lithium project in the Puno district of Peru. Prepared  
1059 for Plateau Energy Metals Inc. under the Guidelines of National Instrument 43-101 and accompanying  
1060 documents NI 43-101.F1 and NI 43-101.CP. Report No: C-MYI-EXP-1727-1134
- 1061 Pastor M, Pastor A, Torró L, Martínez A, Artiaga D, Torres B, Tauler E, Melgarejo JC, Paillo F, Arce-Burgoa OR,  
1062 Alfonso P (2015). The San José-Itos mines, Oruro, Bolivia: Structure and Ag-Sn mineralization. Abstracts,  
1063 13th SGA Biennial Meeting, Nancy, 1:327–330
- 1064 Paton C, Woodhead JD, Hellstrom JC, Hergt JM, Greig A, Maas R (2010) Improved laser ablation U-Pb zircon  
1065 geochronology through robust downhole fractionation correction. *Geochem Geophys Geosyst* 11:1–36.  
1066 <https://doi.org/10.1029/2009GC002618>
- 1067 Pavlova GG, Palessky SV, Borisenko AS, Vladimirov AG, Seifert T, Phan L (2015) Indium in cassiterite and ores  
1068 of tin deposits. *Ore Geol Rev* 66:99–113. <https://doi.org/10.1016/j.oregeorev.2014.10.009>
- 1069 Petersen U (1970) Metallogenic Provinces in South America. *Geol Rundsch* 59:834–897.  
1070 <https://doi.org/10.1007/bf02042275>
- 1071 Petrus JA, Kamber BS (2012) VizualAge: A novel approach to Laser Ablation ICP-MS U-Pb geochronology data  
1072 reduction. *Geostand Geoanal Res* 36:247–270. <https://doi.org/10.1111/j.1751-908X.2012.00158.x>
- 1073 Picard D, Sempere T, Plantard O (2008) Direction and timing of uplift propagation in the Peruvian Andes deduced  
1074 from molecular phylogenetics of highland biotaxa. *Earth Planet Sc Lett* 271:326–336.  
1075 <https://doi.org/10.1016/j.epsl.2008.04.024>
- 1076 Pichavant M, Herrera JV, Boulmier S, Briquieu L, Joron JL, Juteau M, Marin L, Michard A, Sheppard MFS, Treuil  
1077 M, Vernet M (1987) The Macusani glasses, SE Peru: evidence of chemical fractionation in peraluminous  
1078 magmas. In: Mysen BO (ed) *Magmatic Processes: Physicochemical Principles*. *Geo Soc S P* 1:359–374



1079 Pichavant M, Kontak DJ, Briquieu L, Herrera JV, Clark AH (1988a) The Miocene-Pliocene Macusani Volcanics,  
1080 SE Peru I. Mineralogy and magmatic evolution of a two-mica aluminosilicate-bearing ignimbrite suite.  
1081 Contrib Mineral Petr 100:300-324. <https://doi.org/10.1007/BF00379742>

1082 Pichavant M, Kontak DJ, Briquieu L, Herrera JV, Clark AH (1988b) The Miocene-Pliocene Macusani Volcanics,  
1083 SE Peru II. Geochemistry and origin of a felsic peraluminous magma. Contrib Mineral Petr 100:325-338.  
1084 <https://doi.org/10.1007/BF00379742>

1085 Plimer IR, Lu J, Kleeman JD (1991) Trace and rare earth elements in cassiterite - sources of components for the  
1086 tin deposits of the Mole Granite, Australia. Miner Deposita 26:267-274  
1087 <https://doi.org/10.1007/BF00191072>

1088 Pollard PJ, Pichavant M, Charoy B (1987) Contrasting evolution of fluorine- and boron-rich tin systems. Miner  
1089 Deposita 22:315-321. <https://doi.org/10.1007/BF00204525>

1090 Poupeau G, Labrin E, Sabil N, Bigazzi G, Arroyo G, Vatin-Pérignon N (1993) Fission-track dating of 15  
1091 macusanite glass pebbles from the Macusani volcanic field (SE Peru). Nucl Tracks Radiat Meas 21:499-  
1092 506. [https://doi.org/10.1016/1359-0189\(93\)90189-G](https://doi.org/10.1016/1359-0189(93)90189-G)

1093 Pring A, Wade B, McFadden A, Lenehan CE, Cook NJ (2020) Coupled substitutions of minor and trace elements  
1094 in co-existing sphalerite and wurtzite. Minerals 10:147. <https://doi.org/10.3390/min10020147>

1095 Rakovan J, McDaniel DK, Reeder RJ (1997) Use of surface-controlled REE sectoral zoning in apatite from  
1096 Llallagua, Bolivia, to determine a single-crystal SmNd age. Earth Planet Sci Lett 146:329-336.  
1097 [https://doi.org/10.1016/S0012-821X\(96\)00226-9](https://doi.org/10.1016/S0012-821X(96)00226-9)

1098 Redwood S (1993) The Metallogeny of the Bolivian Andes. Mineral Deposit Research Unit Short Course No. 15  
1099 University of British Columbia, Vancouver

1100 Redwood SD, MacIntyre RM (1989) K-Ar dating of Miocene magmatism and related epithermal mineralization of  
1101 the northeastern Altiplano of Bolivia. Econ Geol 84:618-630. <https://doi.org/10.2113/gsecongeo.84.3.618>

1102 Reitsma MJ (2012) Reconstructing the Late Paleozoic–Early Mesozoic Plutonic and Sedimentary Record of  
1103 South-East Peru: Orphaned Back-arcs Along the Western Margin of Gondwana. PhD thesis Terre &  
1104 Environment 111. University of Geneva, Switzerland

1105 Revollo R (1967) Geología de la Cordillera de Santa Vera Cruz: Tesis de Grado, Universidad Mayor San Andrés,  
1106 La Paz

1107 Rivas S, Carrasco R (1968) Geología y yacimientos minerales de la Region de Potosi. Bol Geol Bol 11

1108 Roperch P, Sempere T, Macedo O, Arriagada C, Fornari M, Tapia C, García M, Laj C (2006) Counterclockwise  
1109 rotation of late Eocene–Oligocene fore- arc deposits in southern Peru and its significance for oroclinal  
1110 bending in the central Andes. Tectonics 25:TC3010. <https://doi.org/10.1029/2005TC001882>

1111 Samson IM, Wood SA (2004) The rare earth elements: behaviour in hydrothermal fluids and concentration in  
1112 hydrothermal mineral deposits, exclusive of alkaline settings. In: Linnen RL, Samson IM (eds) Rare  
1113 element geochemistry and mineral deposits. Geological Association of Canada Short Course Notes. Geol  
1114 Assoc Can 17:269-298

- 1115 Sandeman HA, Clark AH, Farrar E (1995) An integrated tectono-magmatic model for the evolution of the  
 1116 southern Peruvian Andes (13°-20°S) since 55 Ma. *Int Geol Rev* 37:1039–1073.  
 1117 <https://doi.org/10.1080/00206819509465439>
- 1118 Sandeman HA, Clark AH, Farrar E, Arroyo G (1997) Lithostratigraphy, petrology and <sup>40</sup>Ar/<sup>39</sup>Ar geochronology of  
 1119 the Crucero Supergroup, Puno Department, SE Peru. *J S Am Earth Sci* 10:223–245.  
 1120 [https://doi.org/10.1016/S0895-9811\(97\)00023-0](https://doi.org/10.1016/S0895-9811(97)00023-0)
- 1121 Sciuba M, Beaudoin G, Makvandi S (2020) Chemical composition of tourmaline in orogenic gold deposits. *Miner*  
 1122 *Deposita*, In Press. <https://doi.org/10.1007/s00126-020-00981-x>
- 1123 Schildgen FT, Hoke DG (2018) The topographic evolution of the Central Andes. *Elements* 14:231–236.  
 1124 <https://doi.org/10.2138/gselements.14.4.231>
- 1125 Schulz KJ, DeYoung JH Jr, Seal RR II, Bradley DC (2017) Critical mineral resources of the United States—  
 1126 Economic and environmental geology and prospects for future supply. *Geol Surv Prof Pap* 1802:797.  
 1127 <https://doi.org/10.3133/pp1802>
- 1128 Schwarz-Schampera U, Herzig PM (2002) *Indium: Geology, Mineralogy and Economics*. Springer, Heidelberg
- 1129 Scotese CR (2009) Late Proterozoic plate tectonics and palaeogeography: A tale of two supercontinents, Rodinia  
 1130 and Pannotia. In: Craig J, Thurow J, Thusu B, Whitham A, Abutarruma Y (eds) *Global Neoproterozoic*  
 1131 *Petroleum Systems: The Emerging Potential in North Africa*. Geological Society, Special Publications,  
 1132 London, pp. 326: 67–83
- 1133 Sempere T (1994) Kimmeridgian? to Paleocene tectonic evolution of Bolivia. In Salfity JA (ed) *Cretaceous*  
 1134 *tectonics in the Andes*. Vieweg Publications, Earth Evolution Sciences Monograph Series, Wiesbaden, pp.  
 1135 168–212
- 1136 Sempere T (1995) Phanerozoic evolution of Bolivia and adjacent regions. In: Tankard AJ, Suárez R, Welsink HJ  
 1137 (eds) *Petroleum Basins of South America*. AAPG Memoir 62:207–230. <https://doi.org/10.1306/M62593C9>
- 1138 Sempere T (2000) Discussion of “Sediment accumulation on top of the Andean orogenic wedge: Oligocene to late  
 1139 Miocene basins of the eastern Cordillera, southern Bolivia” (Horton, 1998). *Geol Soc Am Bull* 112:1752-  
 1140 1755
- 1141 Sempere T, Hérail G, Oller, Bonhomme MG (1990) Late Oligocene- Early Miocene major tectonic crisis and  
 1142 related basins in Bolivia. *Geology* 18:946–949. [https://doi.org/10.1130/0091-  
 1143 7613\(1990\)018<0946:LOEMMT>2.3.CO;2](https://doi.org/10.1130/0091-7613(1990)018<0946:LOEMMT>2.3.CO;2)
- 1144 Sempere T, Butler RF, Richards DR, Marshall LG, Sharp W, Swisher III CC (1997) Stratigraphy and chronology  
 1145 of Late Cretaceous – Early Paleogene strata in Bolivia and northwest Argentina. *Geol Soc Am Bull*  
 1146 109:709-727. [https://doi.org/10.1130/0016-7606\(1997\)109%3C0709:SACOUC%3E2.3.CO;2](https://doi.org/10.1130/0016-7606(1997)109%3C0709:SACOUC%3E2.3.CO;2)
- 1147 Sempere T, Carlier G, Soler P, Fornari M, Carlotto V, Jacay J, Arispe O, Néraudeau D, Cárdenas J, Rosas S,  
 1148 Jiménez N (2002) Late Permian–Middle Jurassic lithospheric thinning in Peru and Bolivia, and its bearing  
 1149 on Andean-age tectonics. *Tectonophysics* 345:153-181. [https://doi.org/10.1016/S0040-1951\(01\)00211-6](https://doi.org/10.1016/S0040-1951(01)00211-6)



- 1150 Sempere T, Folguera A, Gerbault M (2008) New insights into the Andean evolution: An introduction to  
1151 contributions from the 6th ISAG symposium (Barcelona, 2005). *Tectonophysics* 459:1–13.  
1152 <http://dx.doi.org/10.1016/j.tecto.2008.03.011>
- 1153 Serranti S, Ferrini V, Umberto M, Cabri LJ (2002) Trace-element distribution in cassiterite and sulfides from  
1154 rubané and massive ores of the Corvo deposit, Portugal. *Can Mineral* 40:815-835.  
1155 <http://dx.doi.org/10.2113/gscanmin.40.3.815>
- 1156 Sillitoe RH (1972) Relation of metal provinces in western America to subduction of oceanic lithosphere. *Geol Soc*  
1157 *Am Bull* 83:813-818. <https://doi.org/10.1130/0016-7606>
- 1158 Sillitoe RH (1976) Andean mineralization: A model for the metallogeny of convergent plate margins: *Geol Assoc*  
1159 *Can Spec Pap* 14:59-100
- 1160 Sillitoe RH, Halls C, Grant JN (1975) Porphyry tin deposits in Bolivia. *Econ Geol* 70:913–927.  
1161 <https://doi.org/10.2113/gsecongeo.70.5.913>
- 1162 Sillitoe RH, Steele GB, Thompson JFH, Lang JR (1998) Advanced argillic lithocaps in the Bolivian tin-silver belt.  
1163 *Miner Deposita* 33:539–546. <https://doi.org/10.1007/s001260050170>
- 1164 Skirrow RG, Huston DL, Mernagh TP, Thorne JP, Dulfer H, Senior AB (2013) Critical commodities for a high-  
1165 tech world: Australia’s potential to supply global demand. *Geoscience Australia*, Canberra
- 1166 Slater ET, Kontak DJ, McDonald AM, Fayek M (2020) Origin of a multi-stage epithermal Ag-Zn-Pb-Sn deposit:  
1167 the Miocene Cortaderas breccia body, Pirquitas mine, NW Argentina. *Miner Deposita*, in press.  
1168 <https://doi.org/10.1007/s00126-020-00976-8>
- 1169 Soler P, Jiménez N (1993) Magmatic constraints upon the evolution of the Bolivian Andes since Late Oligocene  
1170 times. Extended abstracts, 2nd International Symposium on Andean Geodynamics, Oxford, pp. 447–451
- 1171 Spikings R, Reitsma MJ, Boekhout F, Mišković A, Ulianov A, Chiaradia M, Gerdes A, Schaltegger U (2016)  
1172 Characterisation of Triassic rifting in Peru and implications for the early disassembly of western Pangaea.  
1173 *Gondwana Res* 35:124–143. <https://doi.org/10.1016/j.gr.2016.02.008>
- 1174 Stewart JW, Evernden JF, Snelling NJ (1974) Age Determinations from Andean Peru: A Reconnaissance Survey.  
1175 *Geol Soc Am Bull* 85:1107-1116. [https://doi.org/10.1130/0016-7606\(1974\)85%3C1107:ADFAPA%3E2.0.CO;2](https://doi.org/10.1130/0016-7606(1974)85%3C1107:ADFAPA%3E2.0.CO;2)
- 1177 Suárez-Soruco R (2000) Compendio de Geología de Bolivia. Servicio Nacional de Geología y Minería, YPFB  
1178 18:39-76
- 1179 Sugaki A, Ueno H, Shimada N, Kitakaze A, Hayashi K, Shima H, Sanjines O, Saavedra M (1981) Geological  
1180 study on the polymetallic hydrothermal deposits in the Oruro district, Bolivia. *Sci Rep Tohoku University*,  
1181 Series III. 15:1–52
- 1182 Sugaki A, Ueno H, Shimada N, Kusachi I, Kitakaze A, Hayashi K, Kojima S, Sanjines VO (1983) Geological  
1183 study on the polymetallic ore deposits in the Potosi district, Bolivia. *Sci Rep Tohoku University*, Series III  
1184 15(3):409-460

- 1185 Sugaki A, Ueno H, Kitakaze A, Hayashi K, Shimada N, Kusachi I, Sanjunes VO (1985) Geological study on the  
1186 ore deposits in the La Paz district, Bolivia. *Sci Rep Tohoku University, Series III* 16(2):132-198
- 1187 Sugaki A, Kusachi I, Shimada N (1988a) Granite-series and -type of igneous rocks in the Bolivian Andes and their  
1188 genetic relation to tin-tungsten mineralization. *Min Geol* 38:121– 130.  
1189 <https://doi.org/10.11456/shigenchishitsu1951.38.121>
- 1190 Sugaki A, Kojima S, Shimada N (1988b) Fluid inclusion studies of the polymetallic hydrothermal ore deposits in  
1191 Bolivia. *Miner Deposita* 23:9–15. <https://doi.org/10.1007/BF00204221>
- 1192 Sugaki A, Ueno H, Hayashi K (1990) Sulfur isotope reconnaissance of Bolivian hydrothermal deposits. *Min Geol*  
1193 40:299–312. <https://doi.org/10.11456/shigenchishitsu1951.40.299>
- 1194 Sugaki A, Shimada N, Ueno H, Kano S (2003) K–Ar ages of tin-polymetallic mineralization in the Oruro mining  
1195 district, central Bolivian tin belt. *Resour Geol* 53:273–282. [https://doi.org/10.1111/j.1751-  
1196 3928.2003.tb00176.x](https://doi.org/10.1111/j.1751-3928.2003.tb00176.x)
- 1197 Sun SS, McDonough WF (1989) Chemical and isotopic systematics of oceanic basalts: implications for mantle  
1198 composition and processes. *Geol Soc Lond Spec Pub* 42:313-345.  
1199 <https://doi.org/10.1144/GSL.SP.1989.042.01.19>
- 1200 Taylor RG (1979) *Geology of Tin Deposits*. Elsevier, The Netherlands
- 1201 Thormann W (1966) Investigaciones preliminares sobre la geotectónica y metalogénesis de la zona Challapata-  
1202 Caxata. *Bol Serv Geol Bolivia* 7:118
- 1203 Tindle AG, Breaks FW (1998) Oxide minerals of the Separation Rapids rare-element granitic pegmatite group,  
1204 northwestern Ontario. *Can Mineral* 36:609–635
- 1205 Tshijik Karumb E (2016) The recovery of indium from mining wastes. PhD thesis, Colorado School of Mines
- 1206 Torres B, Melgarejo JC, Torró L, Camprubí A, Castillo-Oliver M, Artiaga D, Campeny M, Tauler E, Jiménez-  
1207 Franco A, Alfonso P, Arce-Burgoa OR (2019) The Poopó polymetallic epithermal deposit, Bolivia:  
1208 mineralogy, genetic constraints, and distribution of critical elements. *Minerals* 9:472.  
1209 <https://doi.org/10.3390/min9080472>
- 1210 Torró L, Melgarejo JC, Gemmrich L, Mollinedo D, Cazorla M, Martínez Á, Pujol-Solà N, Farré de Pablo J,  
1211 Camprubí A, Artiaga D, Torres B, Alfonso P, Arce-Burgoa OR (2019a) Spatial and temporal controls on  
1212 the distribution of indium in xenothermal vein deposits: The Huari Huari district, Potosí, Bolivia. *Minerals*  
1213 9:304. <https://doi.org/10.3390/min9050304>
- 1214 Torró L, Cazorla M, Melgarejo JC, Camprubí A, Tarrés M, Gemmrich L, Campeny M, Castillo-Oliver M, Artiaga  
1215 D, Torres B, Martínez A, Molliendo D, Alonso P, Arce-Burgoa OR (2019b) Indium mineralization in the  
1216 volcanic dome-hosted Ánimas–Chocaya–Siete Suyos polymetallic deposit, Potosí, Bolivia. *Minerals* 9:604.  
1217 <https://doi.org/10.3390/min9100604>
- 1218 Turneure FS (1935) The tin deposits of Llallagua, Bolivia. *Econ Geol* 30:14–60.  
1219 <https://doi.org/10.2113/gsecongeo.30.1.14>

- 1220 Turneure FS (1971) The Bolivian tin-silver province. *Econ Geol* 66:215–225.  
1221 <https://doi.org/10.2113/gsecongeo.66.2.215>
- 1222 U.S. Geological Survey (2020) Mineral commodity summaries 2020. U.S. Geological Survey.  
1223 <https://pubs.usgs.gov/periodicals/mcs2020/mcs2020.pdf>. Accessed 19 June 2020
- 1224 U.S Geological Survey and Servicio Geologico de Bolivia (1992) Geology and mineral resources of the Altiplano  
1225 and Cordillera Occidental, Bolivia. *Bull US Geol Surv* 8:1-365 <https://doi.org/10.3133/b1975>
- 1226 Vermeesch P (2018) IsoplotR: A free and open toolbox for geochronology. *Geosci Front* 9:1479–1493.  
1227 <https://doi.org/10.1016/j.gsf.2018.04.001>
- 1228 Wise M, Brown C (2011) Chemical composition of coexisting columbite-group minerals and cassiterite from the  
1229 Black Mountain pegmatite, Maine. *Eur J Mineral.* 23:817-828. <https://doi.org/10.1127/0935-1221/2011/0023-2102>
- 1231 Wörner G, Schildgen TF, Reich M (2018a) The Central Andes: Elements of an extreme land. *Elements* 14:225–  
1232 230. <https://doi.org/10.2138/gselements.14.4.225>
- 1233 Wörner G, Mamani M, Blum-Oeste M (2018b) Magmatism in the Central Andes. *Elements* 14:237–244.  
1234 <https://doi.org/10.2138/gselements.14.4.237>
- 1235 Zhang DL, Peng JT, Hu RZ, Yuan SD, Zheng DS (2011) The closure of U-Pb system in cassiterite and its  
1236 reliability for dating. *Dizhi Lunping <Geol Rev>* 57:549–554 (in Chinese with English abstract)
- 1237 Zhang R, Lu J, Lehmann B, Li C, Li G, Zhang L, Guo J, Sun W (2017) Combined zircon and cassiterite U–Pb  
1238 dating of the Piaotang granite-related tungsten–tin deposit, southern Jiangxi tungsten district, China. *Ore*  
1239 *Geol Rev* 82:268-284. <https://doi.org/10.1016/j.oregeorev.2016.10.039>
- 1240 Zhang S, Zhang R, Lu J, Ma D, Ding T, Gao S, Zhang Q (2019) Neoproterozoic tin mineralization in South China:  
1241 Geology and cassiterite U–Pb age of the Baotan tin deposit in northern Guangxi. *Miner Deposita* 54:1125-  
1242 1142. <https://doi.org/10.1007/s00126-019-00862-y>
- 1243 Zhao Y, Chen S, Huang Y, Zhao J, Tong Xiang, Chen X (2019) U-Pb Ages, O isotope compositions, Raman  
1244 spectrum, and geochemistry of cassiterites from the Xi’ao copper-tin polymetallic deposit in Gejiu District,  
1245 Yunnan Province. *Minerals* 9:212. <https://doi.org/10.3390/min9040212>
- 1246 Zoheir B, Lehmann B, Emam A, Radwan A, Zhang R, Bain WM, Steele-MacInnis M, Nolte N (2020) Extreme  
1247 fractionation and magmatic–hydrothermal transition in the formation of the Abu Dabbab rare-metal granite,  
1248 Eastern Desert, Egypt. *Lithos* 352–353. Article 105329. <https://doi.org/10.1016/j.lithos.2019.105329>

## 1249 **Figure captions**

- 1250 **Fig. 1.** (A) Location of the main ore deposits, plutons and volcanic deposits along the Bolivian Tin Belt. Modified  
1251 from [Mlynarczyk and Williams-Jones \(2005\)](#). (B) Schematic cross-section model of volcanic- and subvolcanic-  
1252 hosted epithermal and xenothermal deposits in the Bolivian Tin Belt (inspired in [Pollard et al. 1987](#) and [Heuschmidt](#)  
1253 [et al. 2002](#)) showing the postulated ideal location of the studied deposits.

1254 **Fig. 2.** Photomicrographs of representative cassiterite grains for each of the studied Bolivian deposits (reflected light,  
1255 PPL). (A) Subhedral cassiterite crystals in association with siderite, quartz and basal sections of tourmaline  
1256 [Kellhuani]. (B) Twinned and fractured euhedral cassiterite crystal in contact with quartz [Viloco]. (C) Fractured  
1257 subhedral cassiterite crystals with corroded outlines in contact with stannite, sphalerite and pyrrhotite [Viloco]. (D)  
1258 Massive cassiterite aggregates with abundant secondary porosity in an assemblage of quartz-marcasite [Oruro]. (E)  
1259 Breccia texture containing small subhedral and anhedral cassiterite grains and pyrite in a micrometric gangue matrix  
1260 [Oruro]. (F) Subhedral to anhedral cassiterite grains in contact with sphalerite and pyrite-marcasite after pyrrhotite  
1261 showing “bird’s eye” textures [Poopó]. (G) Massive euhedral to subhedral fractured cassiterite grains [Huanuni].  
1262 (H) Massive, twinned cassiterite crystals in an assemblage of quartz and tourmaline [Llallagua]. (I) Breccia-type  
1263 mineralization with subhedral cassiterite grains along with quartz, pyrite, galena, sphalerite and late siderite  
1264 [Colquechaca]. (J) Leather-shaped radial aggregates of cassiterite surrounded by massive sphalerite [Colquechaca].  
1265 (K) Complex sulfide and sulfosalt assemblage along with corroded and twinned cassiterite crystals [Huari Huari].  
1266 (L) Garland-like arrangement of cassiterite, sulfides and sulfosalts wrapping a euhedral hexagonal quartz crystal  
1267 [Ánimas - Chocaya - Siete Suyos]. Abbreviations: Ara = aramayoite; Cst = cassiterite; Cpy = chalcopyrite; Gn =  
1268 galena; Mcs = marcasite; Mia = miargyrite; Osc = oscarkeppffite; Pyr = pyrargyrite; Po = pyrrhotite; Py = pyrite;  
1269 Qz = quartz; Sid = siderite; Sl = sphalerite; Stn = stannite; Ttd = tetrahedrite-group; Turm = tourmaline.

1270 **Fig. 3.** Selected box plots showing element concentrations in cassiterite from the Bolivian Tin Belt (LA-ICP-SF-MS  
1271 data).

1272 **Fig. 4.** Correlation binary plots for cassiterite from the Bolivian tin belt. Bibliographic data is shown for comparison.  
1273 Granite-hosted and granite cupolas: Moore and Howie (1979), Lentz and McAllister (1990), Plimer et al. (1991),  
1274 Murciego et al. (1997), Gorelikova et al. (2004, 2006), Abdalla et al. (2008), Neiva (2008), Pavlova et al. (2015),  
1275 Lerouge et al. (2017), Nascimento and Souza (2017), Zhang et al. (2017), Chen et al. (2019), Cheng et al. (2019),  
1276 Fuchsloch et al. (2019), Zoheir et al. (2019), Mao et al. (2020). Greisen-type: Plimer et al. (1991), Pavlova et al.  
1277 (2015), Chen et al. (2019), Cheng et al. (2019), Fuchsloch et al. (2019), Hulsbosch and Muechez (2019). Migmatitic-  
1278 related: Murciego et al. (1997), Jiang et al. (2004). Pegmatite: Murciego et al. (1997), Plimer et al. (1991), Wise and  
1279 Brown. (2011), Hulsbosch and Muechez (2019), Kendall-Langley et al. (2019). Xenothermal and epithermal  
1280 environment: Murciego et al. (1997), Pavlova et al. (2015), Guo et al. (2018), Cheng et al. (2019), Zhao et al. (2019).  
1281 Skarn: Cheng et al. (2019). VMS: Serranti et al. (2002).

1282 **Fig. 5.** Chondrite-normalized REE spider diagrams for Bolivian Tin Belt cassiterite represented as individual  
1283 analyses (A) and as average values for each deposit/district (B). Bibliographic data are shown for comparison.  
1284 Granite-hosted and granite cupolas: [Plimer et al. \(1991\)](#), [Zoheir et al. \(2019\)](#). Greisen-type: [Plimer et al. \(1991\)](#).  
1285 Migmatitic-related: [Jiang et al. \(2004\)](#).

1286 **Fig. 6.** Tera-Wasserburg U-Pb concordia plots for cassiterite from the Kellhuani, Viloco, Huanuni and Llallagua  
1287 deposits.

1288 **Fig. 7.** Triassic to recent geochronologic chart of the Bolivian Tin Belt, including the new U-Pb cassiterite data  
1289 presented here. Data are ordered from north to south of the Bolivian Tin Belt. Circled numbers correspond to the  
1290 following references: 1) [Ahfeld and Brainsa \(1960\)](#); 2) [Ahfeld and Schneider-Scherbina \(1964\)](#); 3) [Clark and Farrar](#)  
1291 [\(1973\)](#); 4) [Clark et al. \(1983\)](#); 5) [Clark et al. \(2000\)](#); 6) [Cordani \(1967\)](#); 7) [Cordani et al. \(2019\)](#); 8) [Cunningham et](#)  
1292 [al. \(1996\)](#); 9) [Everden \(1961\)](#); 10) [Everden et al. \(1997\)](#); 11) [Gillis et al. \(2006\)](#); 12) [Grant et al. \(1979\)](#); 13) [Kempe](#)  
1293 [et al. \(2008\)](#); 14) [Kontak and Clark \(2002\)](#); 15) [Kontak et al. \(1987\)](#); 16) [McBride et al. \(1983\)](#); 17) [Redwood and](#)  
1294 [Macintyre \(1989\)](#); 18) [Revollo \(1967\)](#); 19) [Rivas and Carrasco \(1968\)](#); 20) [Thormann \(1966\)](#); 21) [Farrar et al. \(1990\)](#).

## 1295 **Table captions**

1296 **Table 1.** Average REE concentrations for Bolivian Tin Belt cassiterite and bibliographic data: Granite-hosted and  
1297 granite cupolas: [Plimer et al. \(1991\)](#), [Zoheir et al. \(2019\)](#). Greisen-type: [Plimer et al. \(1991\)](#). Migmatitic-related:  
1298 [Jiang et al. \(2004\)](#). REE division after [Samson and Wood \(2004\)](#); LREE: La-Sm; MREE: Eu-Dy; HREE: Ho-Lu.

1299 **Table 2.** Summary of the concentrations of Nb, Ta, In, Ge and Ga in cassiterite grains from the Bolivian tin belt.  
1300 Bibliographic data are shown for comparison (references as in [Fig. 4](#)).

1301 **Table 3.** Maximum reported concentrations of In, Ge, Ga, Nb and Ta in ore minerals and concentrates from deposits  
1302 in the Bolivian Tin Belt.

## 1303 **Supplementary material**

1304 **Supplementary Table S1.** EPMA data for spot analyses of cassiterite grains from the Bolivian Tin Belt.

1305 **Supplementary Table S2.** LA-ICP-MS combined trace element and U-Pb isotopic analyses on cassiterite - Metadata.

1306 [Supplementary Table S3](#). Trace-element LA-ICP-MS data for spot analyses of cassiterite grains from the Bolivian  
1307 Tin Belt.

1308 [Supplementary Table S4](#). U-Pb LA-ICP-MS data for spot analyses of cassiterite grains from the Bolivian Tin Belt.

1309 [Supplementary Figure S1](#). Representative downhole LA-ICP-MS spectra for elements at concentrations >L.O.D. in  
1310 studied cassiterite from the Bolivian tin belt.

1311 [Supplementary Figure S2](#). Box plots showing element concentrations in cassiterite from the Bolivian Tin Belt (LA-  
1312 ICP-SF-MS data).

1313 [Supplementary Figure S3](#). Ternary diagrams representing cassiterite analyses from Bolivian Tin Belt and  
1314 bibliographic data. The centered ternary plot (C) is used to accentuate compositional variation in unbalanced  
1315 compositional data by centering the data-set on its average and visualizing the transformed data with a standard  
1316 ternary balance scheme. References given in [Fig. 4](#) caption.

Table 1

	<i>ppm</i>	$\Sigma$ REE	$\Sigma$ LREE	$\Sigma$ MREE	$\Sigma$ HREE	$\Sigma$ LREE/MREE <sub>CN</sub>	$\Sigma$ LREE/HREE <sub>CN</sub>	$\Sigma$ MREE/HREE <sub>CN</sub>
<b>Kellhuani (n=30)</b>	<i>Max.</i>	38.3	13.2	21.3	3.79	0.4	1.6	4.5
	<i>Min.</i>	0.513	0.168	0.266	0.046	0.3	0.6	1.7
	<i>IQR</i>	6.18-2.19	2.28-0.766	3.32-1.14	0.706-0.216	0.4-0.3	1.4-1.0	4.1-2.7
<b>Viloco (n=81)</b>	<i>Max.</i>	35.5	13.5	19.6	2.71	0.4	1.9	5.0
	<i>Min.</i>	0.351	0.124	0.190	0.0367	0.3	0.3	0.8
	<i>IQR</i>	4.42-1.61	1.55-0.562	2.21-0.865	0.483-0.181	0.4-0.4	1.5-1.0	4.2-2.7
<b>San José - Itos (Oruro) (n=22)</b>	<i>Max.</i>	13.9	5.28	7.41	1.18	0.6	2.4	5.3
	<i>Min.</i>	0.498	0.182	0.218	0.0375	0.4	0.9	2.6
	<i>IQR</i>	3.58-1.55	1.30-0.621	1.96-0.825	0.315-0.137	0.4-0.4	1.7-1.5	4.5-4.0
<b>Poopó (n=9)</b>	<i>Max.</i>	5.50	2.00	3.04	0.467	0.4	1.7	4.7
	<i>Min.</i>	0.384	0.142	0.209	0.0326	0.3	1.4	4.1
	<i>IQR</i>	3.26-1.98	1.16-0.711	1.83-1.10	0.272-0.178	0.4-0.4	1.6-1.5	4.6-4.4
<b>Huanuni (n=59)</b>	<i>Max.</i>	14.6	5.30	8.12	1.21	0.4	1.9	5.1
	<i>Min.</i>	0.214	0.0791	0.117	0.0184	0.3	1.5	3.9
	<i>IQR</i>	2.58-1.90	0.977-0.698	1.41-1.04	0.216-0.153	0.4-0.4	1.7-1.6	4.7-4.4
<b>Llallagua (n=13)</b>	<i>Max.</i>	11.7	4.03	6.65	0.991	0.4	1.7	4.8
	<i>Min.</i>	0.452	0.164	0.251	0.0368	0.3	1.2	3.3
	<i>IQR</i>	3.99-2.30	1.41-0.832	2.21-1.24	0.373-0.198	0.4-0.3	1.6-1.5	4.4-4.2
<b>Colquechaca (n=5)</b>	<i>Max.</i>	2.57	0.984	1.36	0.253	0.4	1.8	4.5
	<i>Min.</i>	1.73	0.661	0.921	0.144	0.4	1.5	3.6
	<i>IQR</i>	2.47-2.12	0.907-0.784	1.33-1.14	0.203-0.197	0.4-0.4	1.7-1.5	4.5-3.9
<b>Huari Huari (n=9)</b>	<i>Max.</i>	21.3	8.01	11.5	1.73	0.4	1.9	5.0
	<i>Min.</i>	1.74	0.644	0.954	0.145	0.3	1.3	3.9
	<i>IQR</i>	3.76-1.99	1.38-0.715	2.06-1.10	0.317-0.186	0.4-0.4	1.6-1.5	4.6-4.0
<b>Ánimas - Chocaya - Siete Suyos (n=17)</b>	<i>Max.</i>	4.66	1.68	2.56	0.421	0.4	1.6	4.8
	<i>Min.</i>	0.0636	0.0234	0.0342	0.00590	0.3	1.5	4.1
	<i>IQR</i>	2.12-1.44	0.784-0.543	1.14-0.769	0.197-0.125	0.4-0.4	1.6-1.5	4.4-4.2
<b>Granite hosted and granite cupolas (n=28)</b>	<i>Max.</i>	447	356	48.0	42.8	7.9	80.9	10.5
	<i>Min.</i>	0.658	0.0930	0.0850	0.260	0.1	0.02	0.1
	<i>IQR</i>	164-1.37	144-0.187	11.2-0.132	5.27-0.817	3.9-0.3	3.0-0.05	0.8-0.1
<b>Greisen-type (n=2)</b>	<i>Max.</i>	12.8	10.2	1.10	1.54	4.4	1.7	0.4
	<i>Min.</i>	2.19	0.490	0.710	0.990	0.4	0.1	0.4
<b>Migmatitic-related (n=1)</b>		1.83	1.10	0.350	0.380	1.3	0.7	0.5

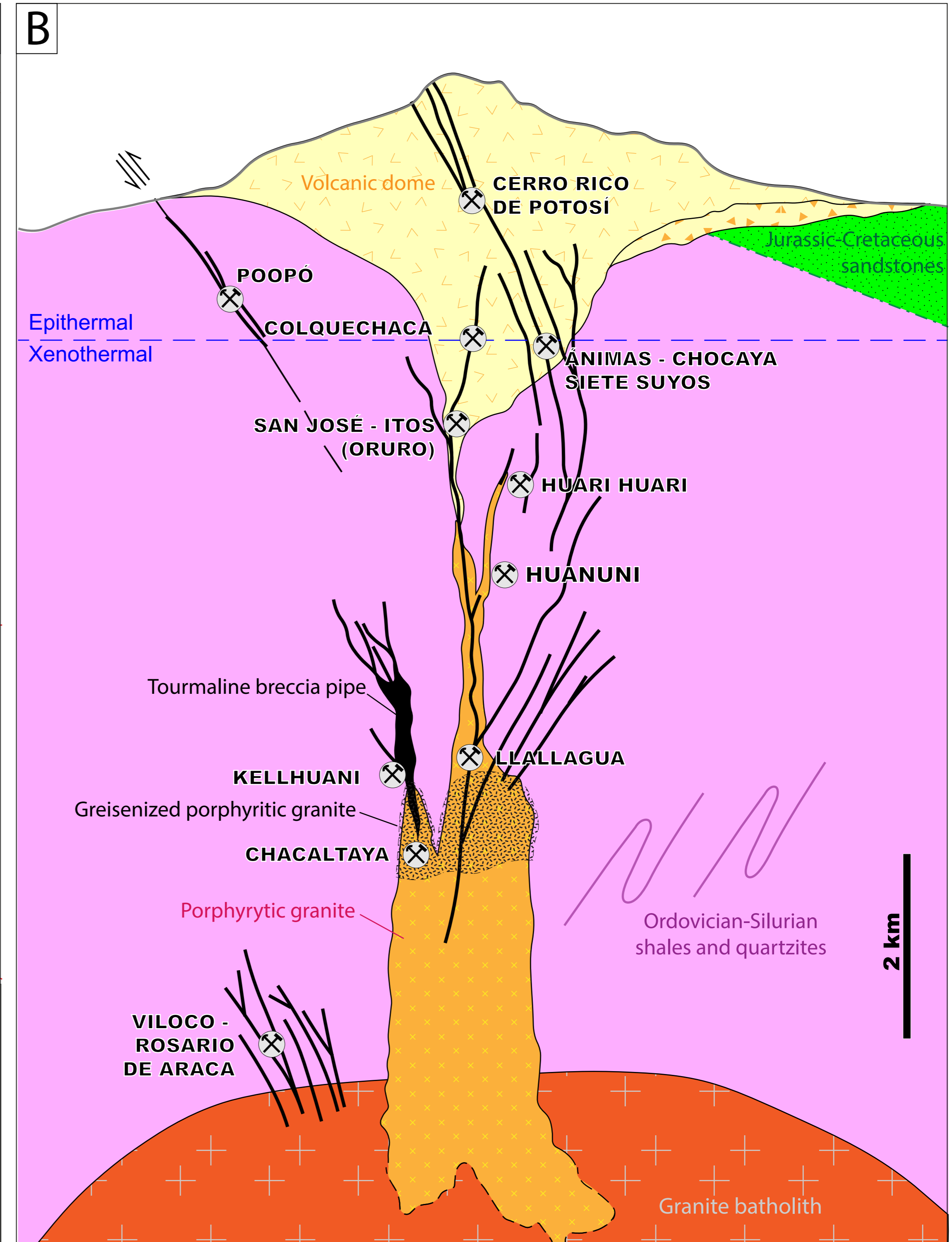
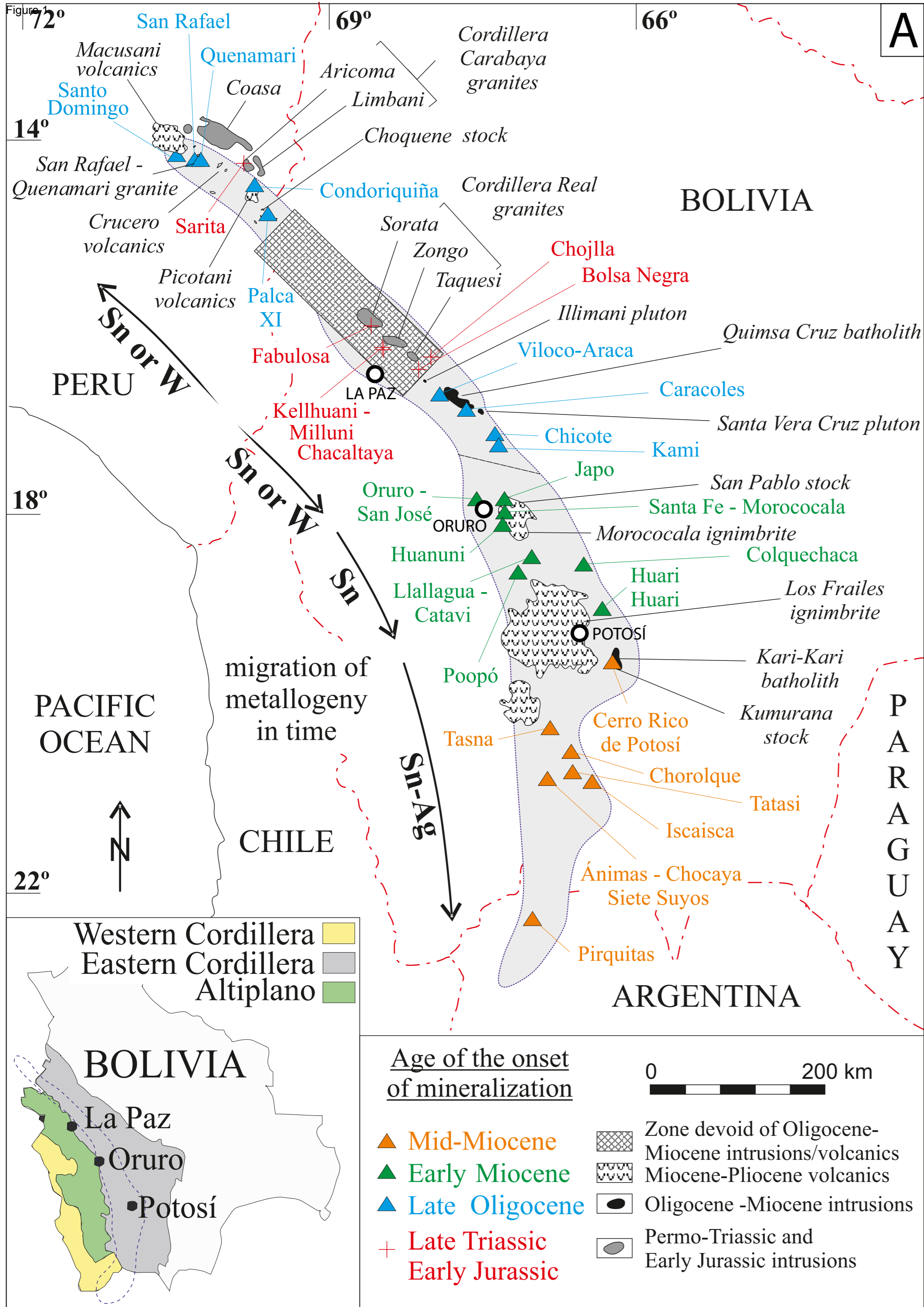
Table 2

		Nb (ppm)	Ta (ppm)	In (ppm)	Ge (ppm)	Ga (ppm)
<b>Kellhuani</b> (n=30)	<i>Max.</i>	2008	2.29	95.7	2.25	20.4
	<i>Min.</i>	0.0626	0.00324	0.700	B.D.L.	0.400
	<i>IQR</i>	60.8-2.26	0.639-0.0403	30.9-2.15	1.25-0.499	3.11-0.932
<b>Viloco</b> (n=81)	<i>Max.</i>	1011	114	268	13.5	42.5
	<i>Min.</i>	B.D.L.	0.00285	0.500	B.D.L.	0.422
	<i>IQR</i>	6.19-0.0515	0.135-0.0138	63.4-10.0	1.85-0.499	5.43-1.59
<b>San José - Itos (Oruro)</b> (n=22)	<i>Max.</i>	11.3	0.575	1414	21.9	1314
	<i>Min.</i>	0.0605	0.00806	7.70	0.573	13.2
	<i>IQR</i>	3.76-0.417	0.075-0.0259	801-31.8	10.1-1.58	377-71
<b>Poopó</b> (n=9)	<i>Max.</i>	0.0370	0.0411	8.30	10.6	49.7
	<i>Min.</i>	0.00649	0.00254	1.60	0.715	18.3
	<i>IQR</i>	0.027-0.0126	0.0196-0.0133	4.7-3	6.45-2.97	43.3-27.3
<b>Huanuni</b> (n=59)	<i>Max.</i>	43.0	0.929	260	6.36	396
	<i>Min.</i>	B.D.L.	0.00139	1.40	0.107	8.87
	<i>IQR</i>	0.488-0.0377	0.025-0.011	122-20.3	3.79-1.47	217-52.9
<b>Llallagua</b> (n=13)	<i>Max.</i>	63.8	1.06	44.2	3.93	78.6
	<i>Min.</i>	0.0167	0.0106	1.60	0.508	7.01
	<i>IQR</i>	18.5-0.989	0.185-0.0143	25-6.5	3.48-2.2	53.1-23.0
<b>Colquechaca</b> (n=5)	<i>Max.</i>	1.06	0.0294	104	7.34	503
	<i>Min.</i>	0.0194	0.0162	1.70	2.23	23.4
	<i>IQR</i>	0.611-0.022	0.0289-0.0226	95.2-1.7	6.37-2.78	438-53.5
<b>Huari Huari</b> (n=9)	<i>Max.</i>	6.05	0.253	1041	8.32	916
	<i>Min.</i>	0.00684	0.0113	11.3	0.913	105
	<i>IQR</i>	2.58-0.034	0.0872-0.0267	889-96.9	4.79-2.89	690-150
<b>Ánimas - Chocaya - Siete Suyos</b> (n=17)	<i>Max.</i>	0.689	0.0299	996	33.6	7437
	<i>Min.</i>	B.D.L.	0.000390	56.7	0.219	2.31
	<i>IQR</i>	0.059-0.00971	0.0165-0.00873	582-174	7.81-3.23	292-53.1
<b>Granite-hosted and granite cupolas (n=392)</b>	<i>Max.</i>	26800	306700	800	1.17	400
	<i>Min.</i>	B.D.L.	B.D.L.	B.D.L.	0.03	B.D.L.
	<i>IQR</i>	3389-100	5078-100	304-2.50	0.59-0.263	19.9-5.00
<b>Greisen-type</b> (n=103)	<i>Max.</i>	26800	103300	160	-	22.9
	<i>Min.</i>	0.07	B.D.L.	0.02	-	0.68
	<i>IQR</i>	2400-308	6311-170	2.30-0.195	-	9.00-2.74
<b>Migmatitic-related</b> (n=6)	<i>Max.</i>	6400	100	-	-	-
	<i>Min.</i>	0.17	0.07	-	-	-
	<i>IQR</i>	2225-150	100-25.1	-	-	-
<b>Pegmatite</b> (n=177)	<i>Max.</i>	28500	32000	0.02	24997	4580
	<i>Min.</i>	B.D.L.	B.D.L.	0.02	B.D.L.	B.D.L.
	<i>IQR</i>	2780-175	4088-0.55	-	361-13.0	593-115
<b>Skarn</b> (n=21)	<i>Max.</i>	626	248	-	-	27.5
	<i>Min.</i>	5.51	0.05	-	-	1
	<i>IQR</i>	146-25.4	12.9-1.42	-	-	8.74-1.78
<b>VMS</b> (n=2)	<i>Max.</i>	-	53	309	-	-
	<i>Min.</i>	-	45	284	-	-
	<i>IQR</i>	-	51.0-47.0	303-290	-	-
<b>Xenothermal and epithermal environment (n=48)</b>	<i>Max.</i>	13316	3760	1508	-	149
	<i>Min.</i>	B.D.L.	B.D.L.	3.88	-	0.22
	<i>IQR</i>	172-0.12	31.5-0.01	358-5.00	-	21.3-2.06



Table 3

Reference	Deposit	Method	Sample type	In (ppm)	Ge (ppm)	Ga (ppm)
Ishihara et al. (2011)	Cerro Rico de Potosí	ICP-MS	Sphalerite	5740		69
Ishihara et al. (2011)	Pailaviri	ICP-MS	Composite ore	43		28
Ishihara et al. (2011)	San Jacinto	ICP-MS	Composite ore	292		24
Ishihara et al. (2011)	Huari Huari	ICP-MS	Composite ores	3080		148
Ishihara et al. (2011)	Reserva	ICP-MS	Zn concentrate	553		14
Ishihara et al. (2011)	San Lorenzo	ICP-MS	Zn concentrate	1080		9
Ishihara et al. (2011)	Tuntoco	ICP-MS	Composite ore	100		125
Ishihara et al. (2011)	Porco	ICP-MS	Sphalerite	821		138
Ishihara et al. (2011)	Bolívar	ICP-MS	Breccia Ore	2730		284
Ishihara et al. (2011)	Colquiri	ICP-MS	Ore	393		88
Ishihara et al. (2011)	Siete Suyos - Ánimas	ICP-MS	Composite Ore	2240		312
Ishihara et al. (2011)	Ánimas	ICP-MS	Composite Ore	2510		210
Ishihara et al. (2011)	Chorolque	ICP-MS	Composite Ore	1		32
Ishihara et al. (2011)	Tatasi	ICP-MS	Composite Ore	630		24
Ishihara et al. (2011)	San Vicente	ICP-MS	Sphalerite ore	1290		133
Ishihara et al. (2011)	Pirquitas (Argentina)	ICP-MS	Composite ore	1160		567
Ishihara et al. (2011)	San Cristóbal	ICP-MS	Zn concentrate	11		17
Ishihara et al. (2011)	Cerro Rico de Potosí	EPMA	Sphalerite	12700		
Ishihara et al. (2011)	Cerro Rico de Potosí	EPMA	Petrukite	48600		
Ishihara et al. (2011)	Bolívar	ICP-MS	Zn concentrate	584		
Ishihara et al. (2011)	Colquiri	ICP-MS	Zn concentrate	213		
Ishihara et al. (2011)	Porco	ICP-MS	Zn concentrate	499		
Ishihara et al. (2011)	Huari Huari	ICP-MS	Zn concentrate	3080		
Ishihara et al. (2011)	Cerro Rico de Potosí	ICP-MS	Zn concentrate	1199		
Ishihara et al. (2011)	San Lorenzo	ICP-MS	Zn concentrate	1080		
Ishihara et al. (2011)	Bolívar	ICP-MS	Zn concentrate	584		
Ishihara et al. (2011)	Reserva	ICP-MS	Zn concentrate	553		
Ishihara et al. (2011)	Porco	ICP-MS	Zn concentrate	499		
Ishihara et al. (2011)	Colquiri	ICP-MS	Zn concentrate	213		
Ishihara et al. (2011b)	San Cristóbal	ICP-MS	Zn concentrate	10.7		
Artiaga et al. (2013)	Viloco	EPMA	Stannite	20400		
Artiaga et al. (2013)	Viloco	EPMA	Sphalerite	2000		
Murakami and Ishihara (2013)	Cerro Rico de Potosí	EPMA	Sphalerite	95900		
Murakami and Ishihara (2013)	Huari Huari	EPMA	Sphalerite	182200		
Murakami and Ishihara (2013)	Bolívar	EPMA	Sphalerite	6900		
Murakami and Ishihara (2013)	Porco	EPMA	Sphalerite	3900		
Murakami and Ishihara (2013)	Cerro Rico de Potosí	fsLA-ICPMS	Sphalerite	430		
Murakami and Ishihara (2013)	Huari Huari	fsLA-ICPMS	Sphalerite	3450		116
Murakami and Ishihara (2013)	Bolívar	fsLA-ICPMS	Sphalerite	2290		249
Murakami and Ishihara (2013)	Porco	fsLA-ICPMS	Sphalerite	20		35
Murakami and Ishihara (2013)	Cerro Rico de Potosí	fsLA-ICPMS	Miargyrite	4		not detected
Murakami and Ishihara (2013)	Huari Huari	fsLA-ICPMS	Jamesonite	624		not detected
Jiménez-Franco et al. (2018)	Santa Fe	ICP-MS	Porphyry stock	2.5		47
Jiménez-Franco et al. (2018)	Santa Fe	ICP-MS	Dome	1.6		5
Jiménez-Franco et al. (2018)	Santa Fe	ICP-MS	Dike	2.2		9
Jiménez-Franco et al. (2018)	Santa Fe	ICP-MS	Host rock	1		15
Jiménez-Franco et al. (2018)	Morococala (Santa Fe)	ICP-MS	Concentrate	200		35
Jiménez-Franco et al. (2018)	Japo (Santa Fe)	ICP-MS	Concentrate	200		21
Jiménez-Franco et al. (2018)	Santa Fe	EPMA	Sphalerite	300		
Jiménez-Franco et al. (2018)	Morococala (Santa Fe)	EPMA	Sphalerite	1700		
Jiménez-Franco et al. (2018)	Japo (Santa Fe)	EPMA	Stannite	2000		
Jiménez-Franco et al. (2018)	Morococala (Santa Fe)	EPMA	Stannite	4500		
Jiménez-Franco et al. (2018)	Japo (Santa Fe)	EPMA	Sakuraiite	1400		
Jiménez-Franco et al. (2018)	Morococala (Santa Fe)	EPMA	Sakuraiite	16800		
Jiménez-Franco et al. (2018)	Japo (Santa Fe)	EPMA	Kersterite	1400		
Cacho et al. (2019)	Huanuni	EPMA	Sphalerite	8800		
Cacho et al. (2019)	Huanuni	EPMA + LA-ICPMS	Stannite	3300	1300	123
Torres et al. (2019)	Poopó	EPMA + LA-ICPMS	Sphalerite	10500		1360
Torres et al. (2019)	Poopó	EPMA + LA-ICPMS	Stannite	11100		199
Torres et al. (2019)	Poopó	EPMA + LA-ICPMS	Rhodostannite	6070	2100	441
Torres et al. (2019)	Poopó	EPMA + LA-ICPMS	Teallite	10800		108
Torres et al. (2019)	Poopó	EPMA	Franckeite		1600	
Torró et al. (2019a)	Huari Huari	EPMA	Sphalerite	34900	800	6400
Torró et al. (2019a)	Huari Huari	EPMA	Stannite	26400	not detected	1400
Torró et al. (2019a)	Huari Huari	EPMA	Jamesonite	1400		100
Torró et al. (2019b)	Ánimas - Chocaya - Siete Suyos	EPMA	Sphalerite	96600	700	
Torró et al. (2019b)	Ánimas - Chocaya - Siete Suyos	EPMA	Stannite	41100	1400	
Pring et al. (2020)	Ánimas - Chocaya	LA-ICP-MS	Wurtzite	150		
Pring et al. (2020)	Ánimas - Chocaya	LA-ICP-MS	Sphalerite	600		





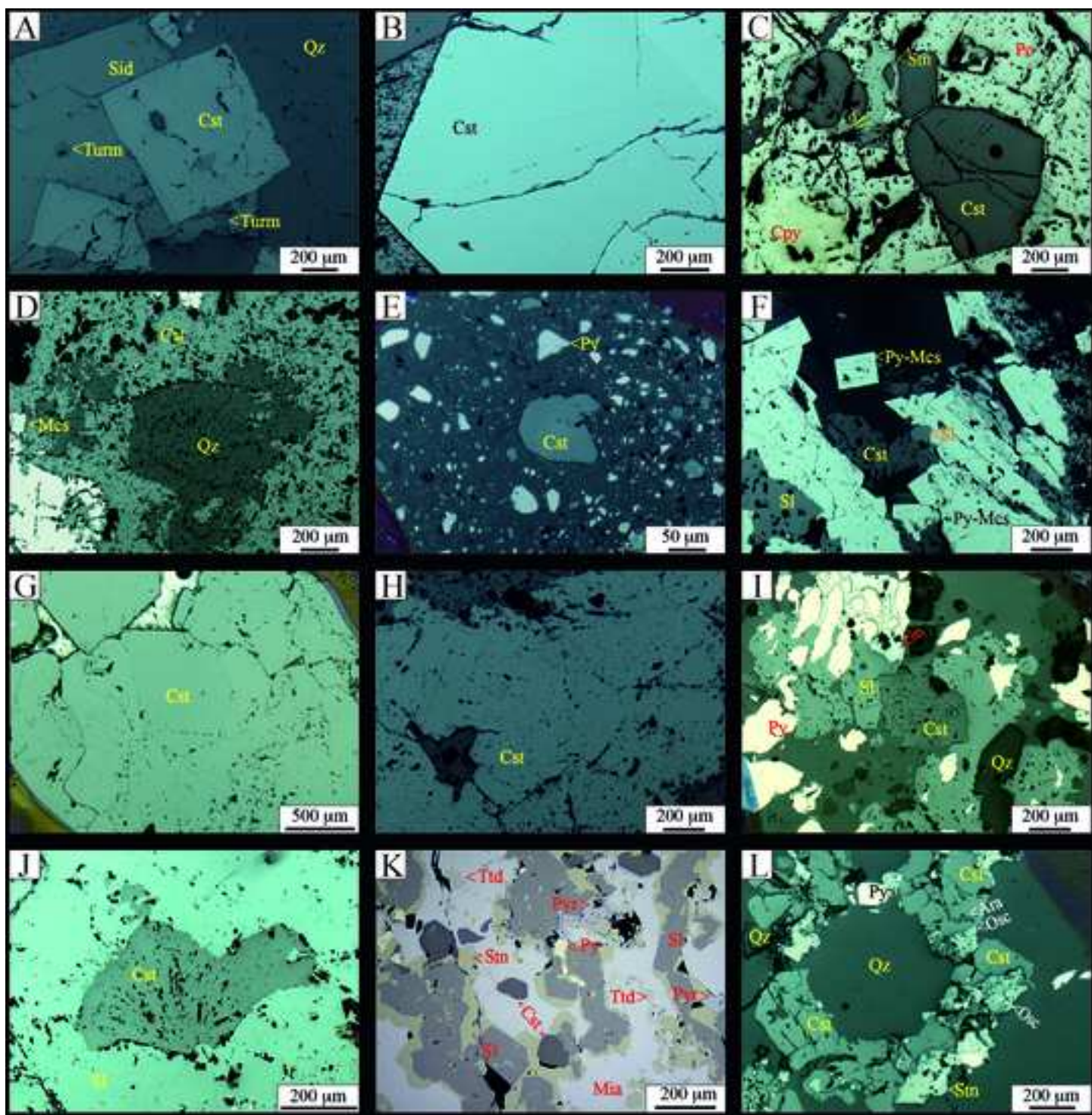
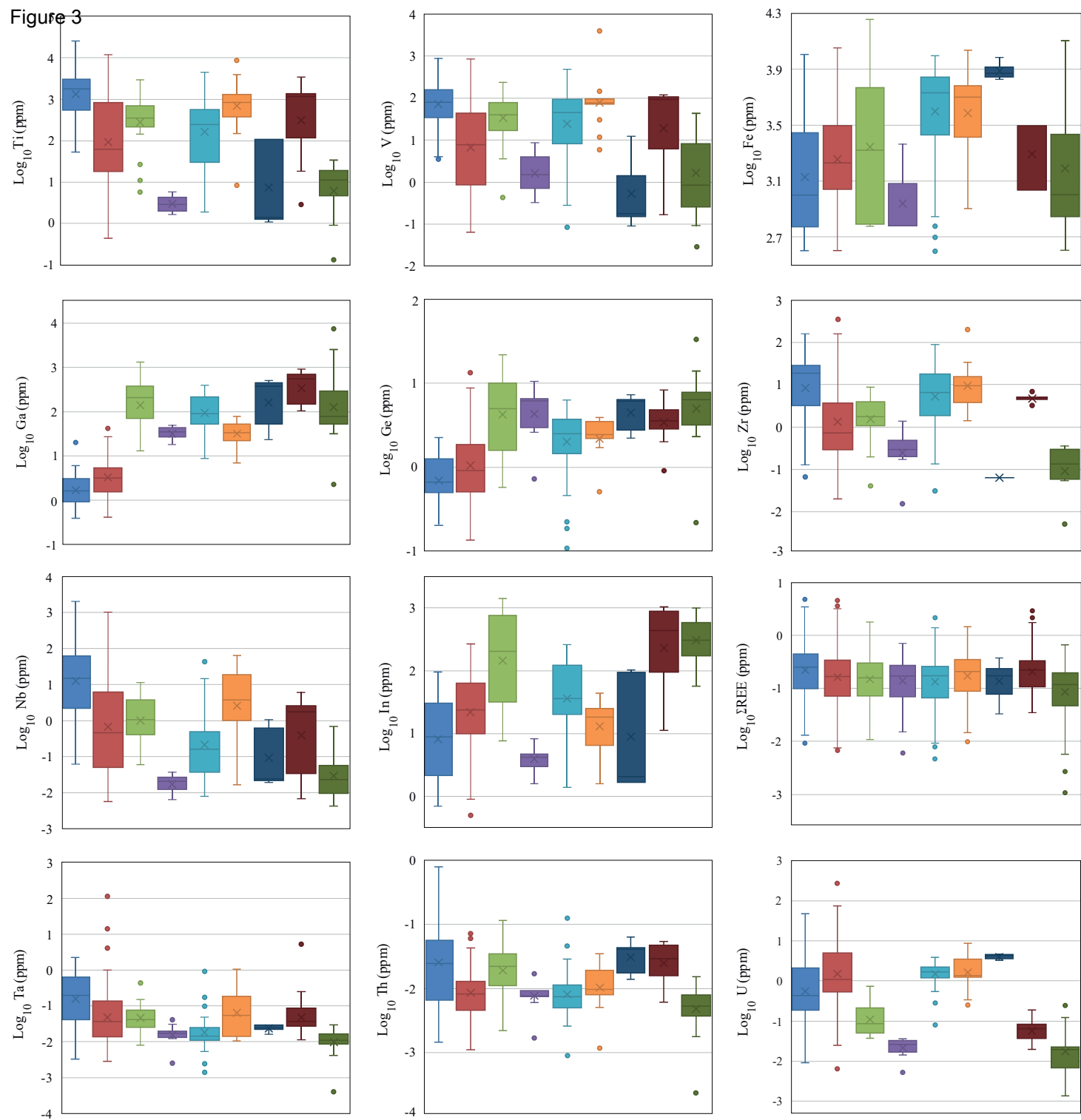


Figure 3

**Mine district**

Interquartile Range (IQR)



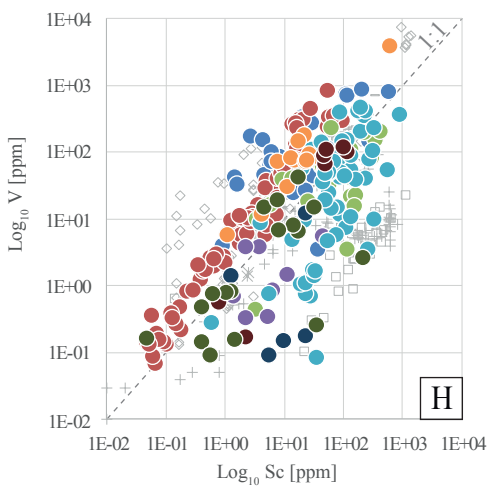
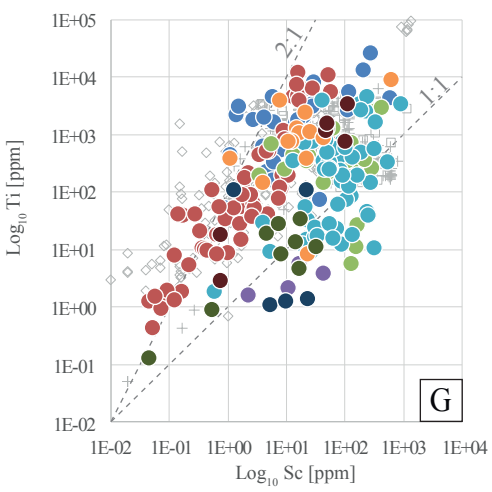
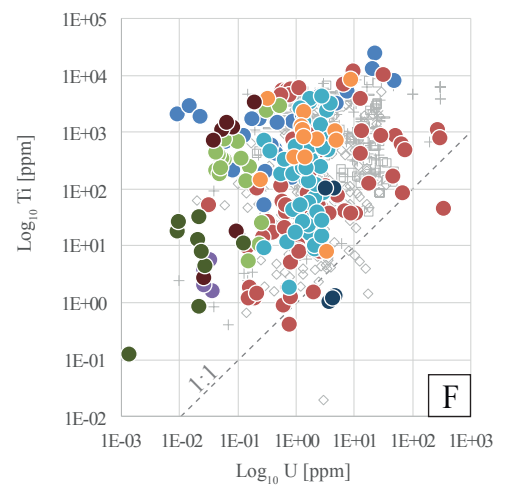
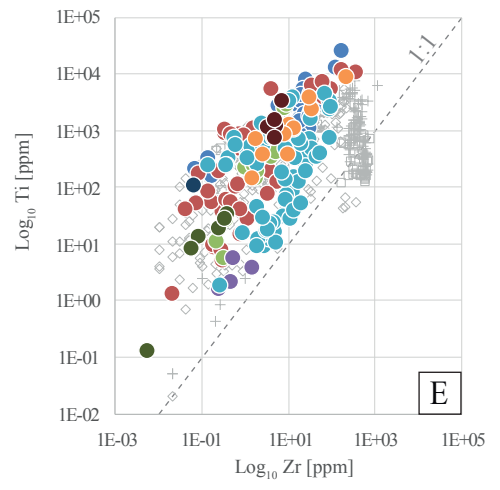
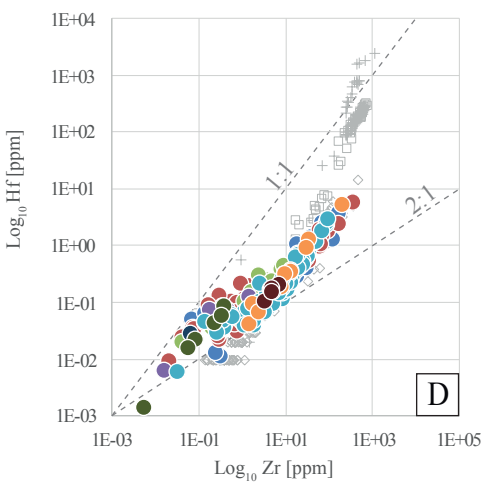
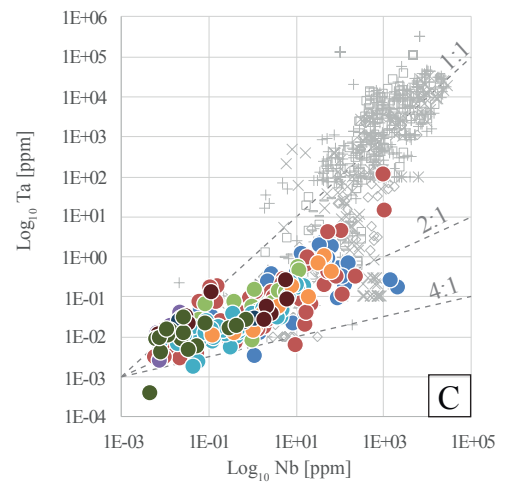
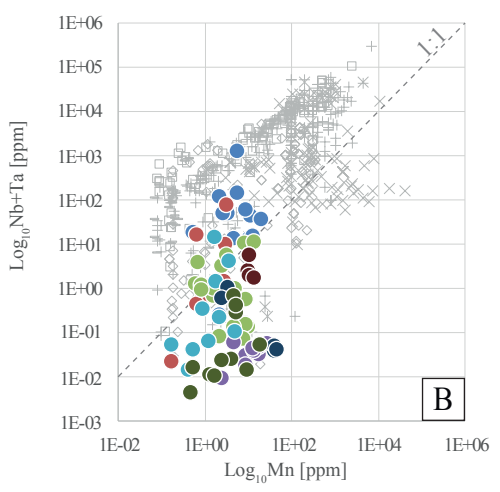
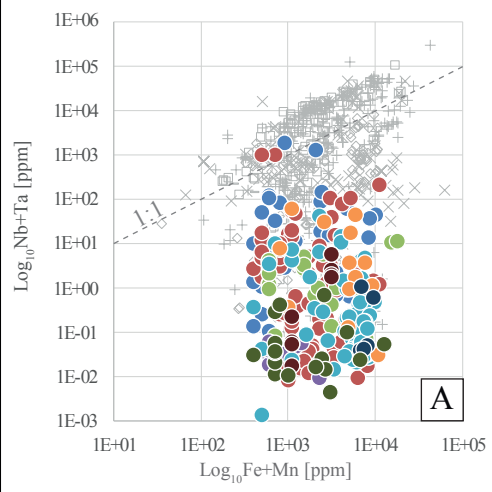
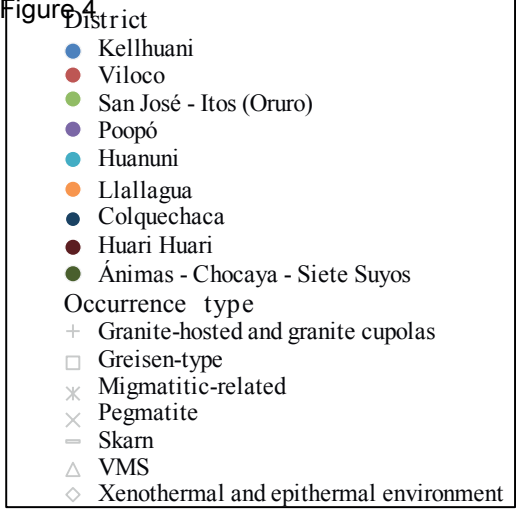
Range within 1.5 IQR

— Median line

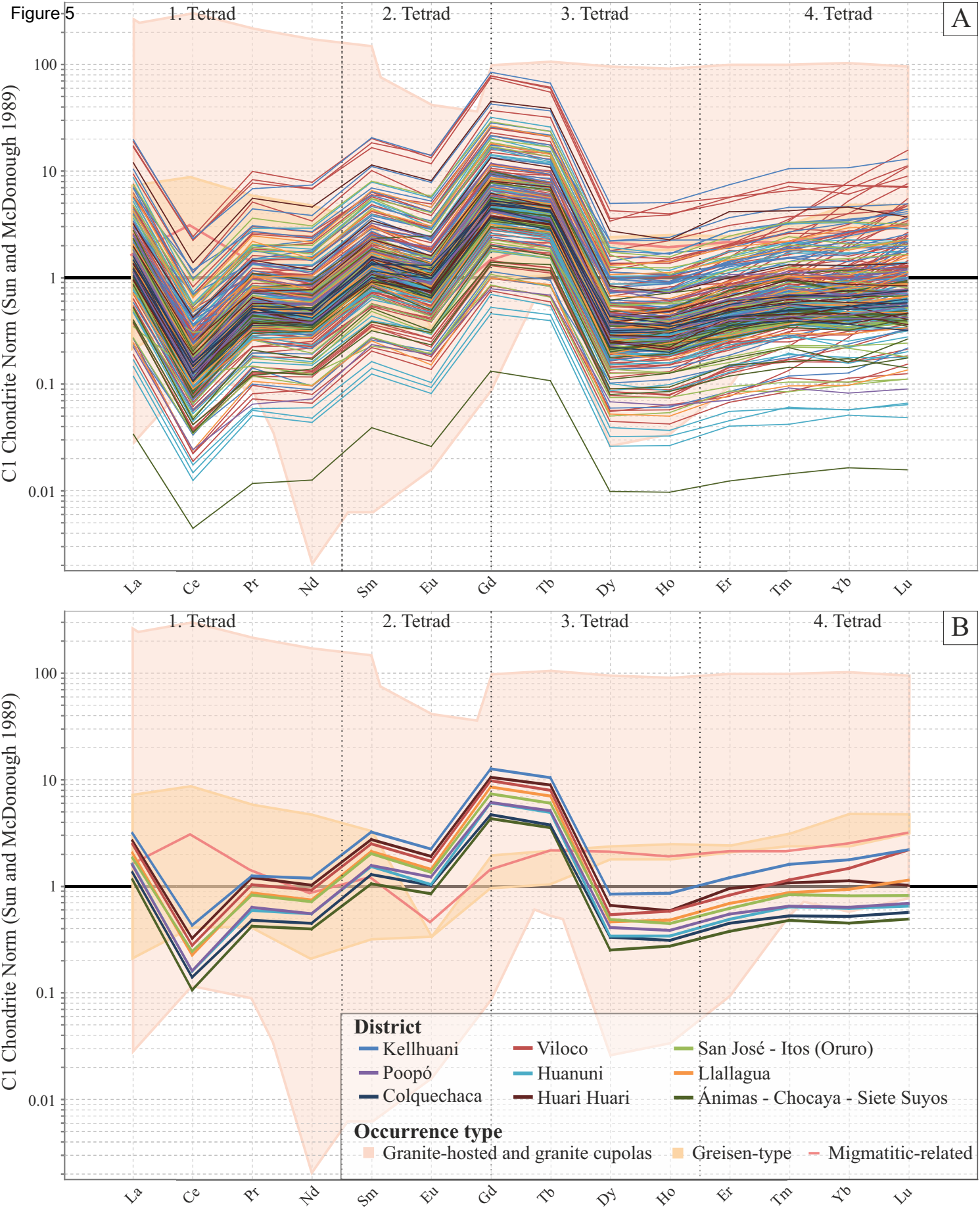
× Mean

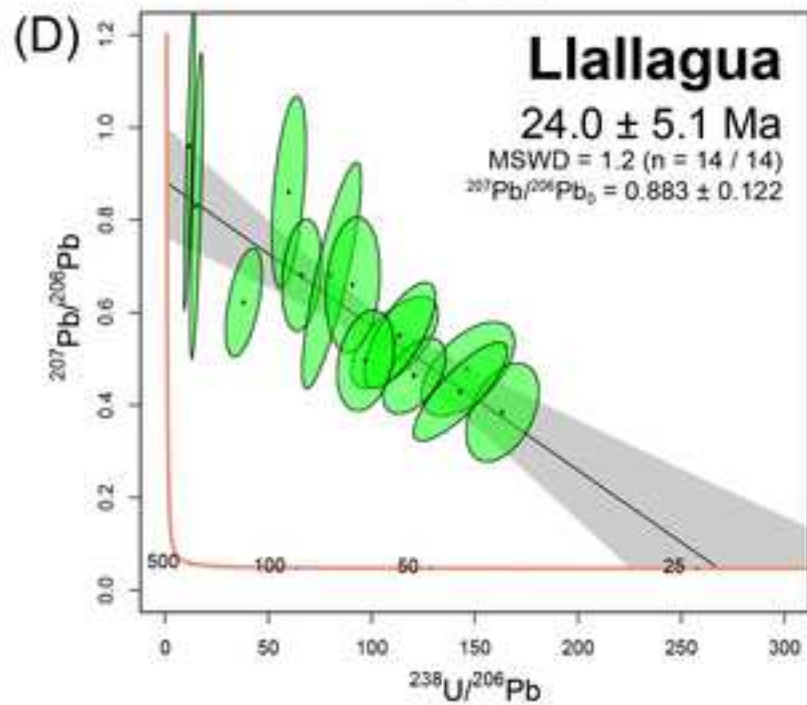
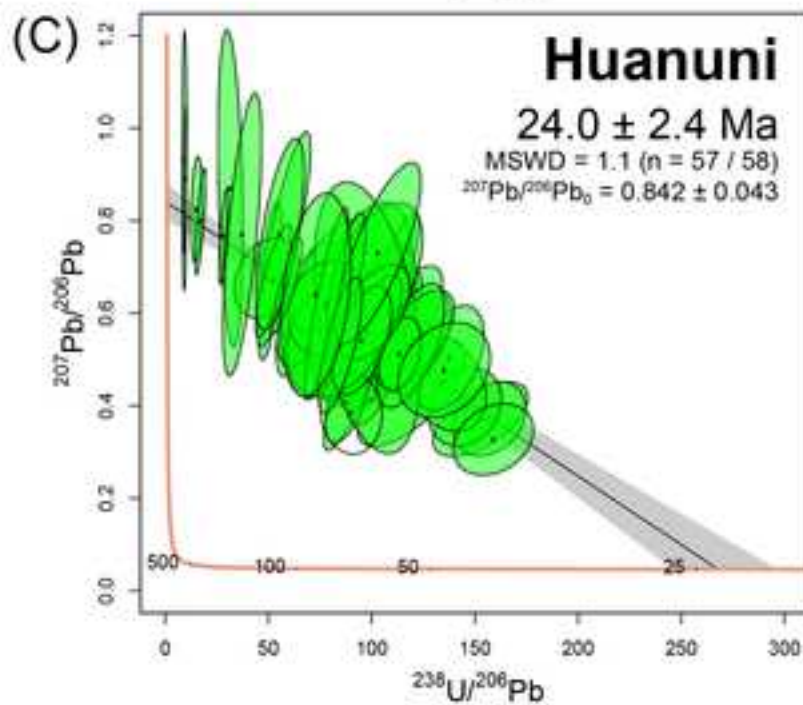
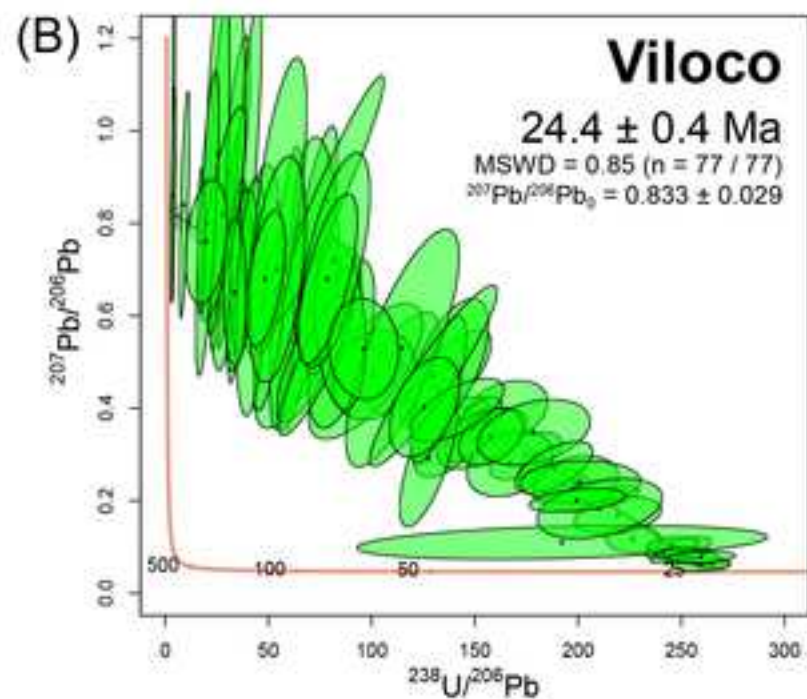
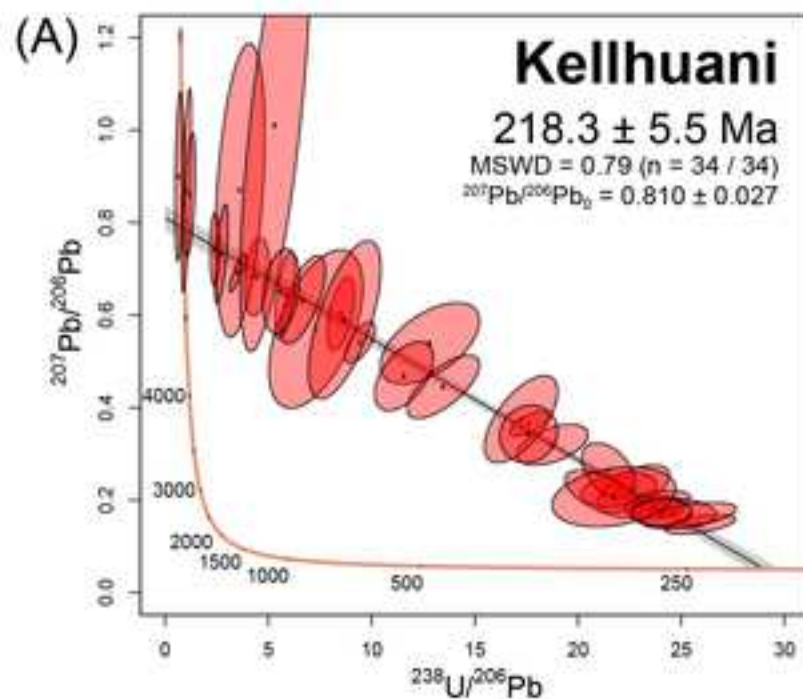
• Outliers

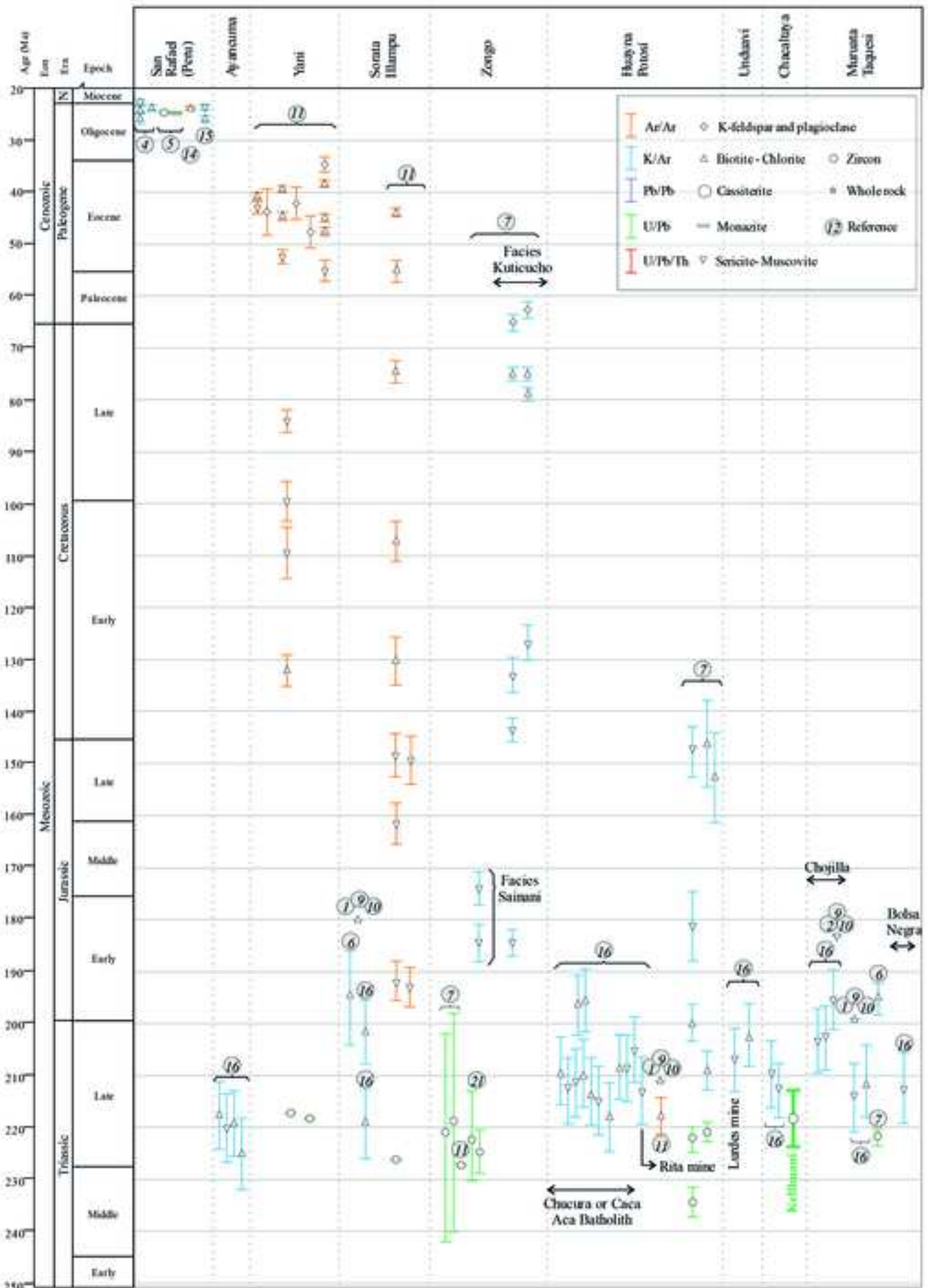
**Figure 4**



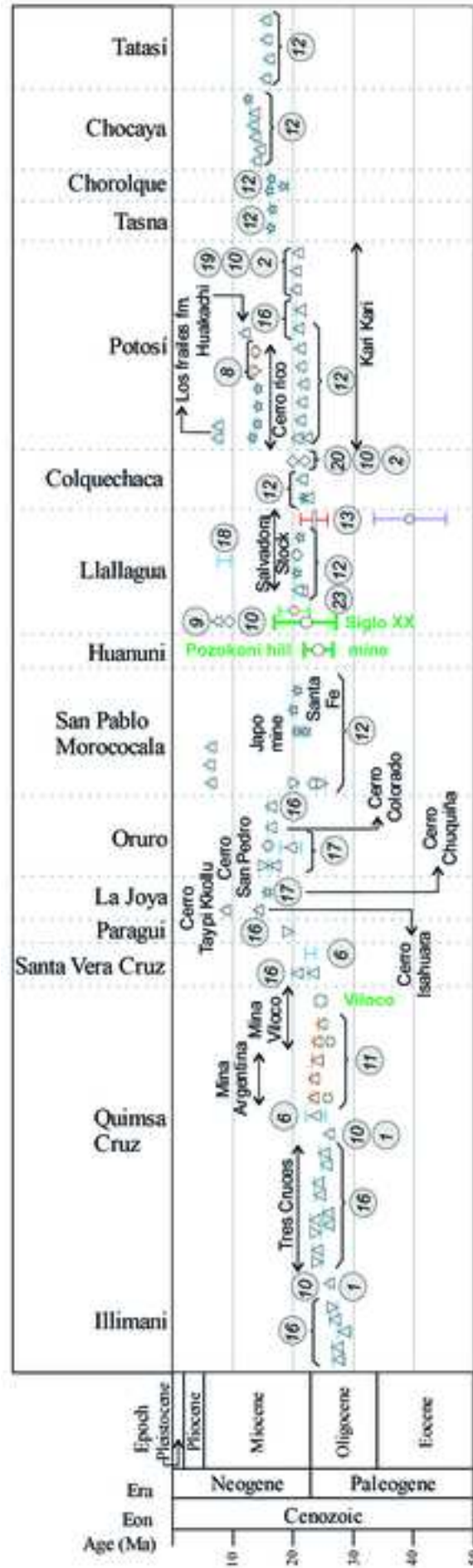















[Click here to access/download](#)

**Supplementary Material**

**Supplementary Table S1 - EPMA cst Bolivia.xlsx**





Click here to access/download  
**Supplementary Material**  
Supplementary Table S2 - LA-ICP-  
MS\_Metadata\_Cassiterite.xlsx



[Click here to access/download](#)

**Supplementary Material**

Supplementary Table S3 - CST-LAICPMS DATA.xlsx





[Click here to access/download](#)

**Supplementary Material**

Supplementary Table S4 - U\_Pb LA-ICP-MS.xlsx





Click here to access/download  
**Supplementary Material**  
Supplementary Figure\_S1.pdf





[Click here to access/download](#)

**Supplementary Material**

Supplementary Figure\_S2.pdf





Click here to access/download  
**Supplementary Material**  
Supplementary Figure\_S3.pdf

